공학박사 학위논문

Effect of Microstructure and Electronic Structure on the Thermoelectric Properties of Polycrystalline SnSe

미세구조 및 전자 구조가 다결정 SnSe의 열전 특성에 미치는 영향

2020년 2월

서울대학교 대학원

재 료 공 학 부

조 준 영

Abstract

Effect of Microstructure and Electronic Structure on the Thermoelectric Properties of Polycrystalline SnSe

Jun-Young Cho
Department of Materials Science and Engineering
The Graduate School
Seoul National University

The depletion of energy resources and the environmental pollution have become a global issue. And the world's demand for new, eco-friendly, and renewable energy resources has been increasing. Thermoelectric (TE) material, which can reversibly convert thermal energy into electrical energy, has been considered as a way to solve the energy crises and environmental problems. The efficiency of TE material is represented by the dimensionless figure of merit ZT =

$S^2\sigma T/k$, where S, σ, k, and T are Seebeck coefficient, electrical conductivity, thermal conductivity and absolute temperature, respectively. In order to achieve high ZT values, TE materials should possess high electrical conductivity, large Seebeck coefficient, and low thermal conductivity simultaneously. However, these TE parameters have complex interrelationships, which makes it difficult to optimize ZT. For example, the increase of carrier concentration can lead to the increase in electrical conductivity (σ), but can lead to the decrease in Seebeck coefficient (S). And it is difficult to suppress only the thermal conductivity without affecting the electrical conductivity. In order to obtain a high TE efficiency, the charge carrier concentration should be optimized, and in general, it is known that high TE efficiency can be obtained when the carrier concentration lies in the range of 10^{19} to 10^{20} cm^{-3}.

In recent years, tin selenide (SnSe) which contains non-toxic and earth-abundant elements has been considered as a promising TE material since a remarkable ZT value of ~2.6 at 923 K (the world record to date) along the b-axis in its single crystal form were reported in 2014.

It, however, is still difficult to use single crystal TE materials in devices because of poor mechanical properties and high production costs. For these reasons, the research on SnSe has focused on

developing high performance polycrystalline SnSe. The low ZT values of polycrystalline SnSe which is lower than that of single crystal SnSe originate mainly from its poor electrical conductivity and high thermal conductivity. Therefore, in order to achieve polycrystalline SnSe having high TE efficiency, the electrical conductivity should be enhanced and thermal conductivity should be suppressed.

In this study, the effects of microstructure and electronic structure on the TE properties of polycrystalline SnSe were investigated, and the TE efficiency was improved by increasing the electrical conductivity and reducing the thermal conductivity by controlling the microstructure, band structure, and interfacial structure.

First, to improve the electrical conductivity of polycrystalline SnSe, the effects of the pressure applied during spark plasma sintering (SPS) on the microstructure and the TE properties of the polycrystalline SnSe were investigated. Polycrystalline SnSe powder were synthesized by mechanical alloying, and then specimens having different degrees of texturing were fabricated by SPS under various pressure conditions (30, 60, 90, 120MPa). As the sintering pressure was increased from 30 to 120 MPa, the hole carrier mobility was increased by the enhancement of degree of texture, which resulted in the improvement of the electrical conductivity. On the other hand,

the increase in sintering pressure led to a significant increase in thermal conductivity due to the increase of lattice thermal conductivity, which can be attributed to the reduction of the phonon scattering at grain boundaries. A ZT of ~0.7 was obtained at 823K from the polycrystalline SnSe sintered with a pressure of 60 MPa, which can result from large increase in electrical conductivity with relatively small increase of the thermal conductivity. This study shows that the TE properties of the polycrystalline SnSe can be improved by controlling the degree of texture by changing the pressure applied during SPS.

Second, the electrical transport and TE properties of SnSe−SnTe solid solution were investigated. $SnSe_{1-x}Te_x$ (x = 0, 0.1, 0.3, 0.5, 0.8, 1) bulk specimens were prepared by mechanical alloying and SPS. The solubility limit of Te in $SnSe_{1-x}Te_x$ was found to lie somewhere between x = 0.3 and 0.5. With increasing Te content, the electrical conductivity was increased due to the increase of hole carrier concentration. The measurements and calculations of band gap using UV−VIS−NIR spectrum and DFT, respectively, showed that the band gap was decreased as the amount of Te was increased, which can lead to the increase of carrier concentration. The total thermal conductivity was decreased with increasing Te content, which can be attributed to the reduction of lattice thermal conductivity. Te has

atomic mass and size larger than Se, and the presence of Te at Se site can act as an effective point defect, increasing phonon scattering and thus reducing lattice thermal conductivity. A ZT of ~ 0.78 was obtained at 823K from $SnSe_{0.7}Te_{0.3}$, which is ~ 11 % improvement compared to that of SnSe.

Third, the effects of CNT addition on the charge transfer and TE properties of $SnSe_{0.7}Te_{0.3}$/CNT composites were investigated. Various amounts of CNT (0, 0.3, 0.6 and 1 wt %) were added to $SnSe_{0.7}$Te0.3, which were sintered using SPS. Most CNTs are dispersed along the grain boundaries of $SnSe_{0.7}Te_{0.3}$ and are connected to each other when the amount of CNT reaches 0.6 wt %, thereby forming new interfaces, which can result in the decrease in hole carrier mobility. With increasing CNT contents, the electrical conductivity was increased, which can be attributed to the higher intrinsic hole concentration of CNTs compared to $SnSe_{0.7}Te_{0.3}$. When 0.3 wt % CNT was added, the lattice thermal conductivity was decreased by phonon scattering at interface, which results in the decrease of total thermal conductivity. However, when 0.6 and 1 wt % CNT was added, the total thermal conductivity was increased due to the high intrinsic lattice thermal conductivity of CNT. A ZT of ~ 0.86 at 823K was obtained from SnSe0.7Te0.3 with 0.3 wt % CNT, which is the highest ZT value obtained in this study.

These results provide an understanding of the effects of microstructures and electronic structures on the TE properties of polycrystalline SnSe, and can be used to control the TE properties of polycrystalline SnSe which can be used in practical TE devices.

Keywords: SnSe, Spark plasma sintering, Thermoelectric properties, Microstructure, Band structure, Texturing, Solid solution, Composite

Student Number: 2014-30205

Table of Contents

List of Figures

List of Tables

CHAPTER 1. General Introduction

The pollution of fossil fuels and other traditional energy sources has always been global issues. As increasing the depletion of fossil energy sources, the demand for new, clean and sustainable energy is even more urgent [1]. Thermoelectric (TE) technology, which can convert waste heat into electricity directly, has been attracting attention as one of the alternative solutions because it is clean and environmentally safe. to solve energy problem [2−4]. The efficiency of a TE material is represented by the dimensionless figure of merit $ZT = S^2\sigma T/k$, where S, σ, k, and T are Seebeck coefficient, electrical conductivity, absolute temperature, and thermal conductivity, respectively [4]. In order to achieve high ZT values, TE materials should possess the high electrical conductivity, the large Seebeck coefficient, and low thermal conductivity simultaneously. [2, 5]. Large ZT values can be obtained by high power factor ($PF = S^2\sigma$) and low thermal conductivity. However, these TE parameters have complex interrelationships, which makes it difficult to optimize ZT [6]. For example, the higher carrier concentration leads to larger electrical conductivity (σ), but is negative to the Seebeck coefficient (S). And it is also difficult to solely suppress thermal conductivity without deteriorating the electrical conductivity. Therefore, the optimization of the carrier

concentration is needed to improve the efficiency of a TE material for practical application. And the effort to find TE materials which have performance high enough to be used in devices, which consist of earth-abundant and non-toxic elements, is continuing today.

Over the past several decades, various TE materials such as Bi_2Te_3- , PbTe- and ZnSb-based compounds, skutterudites, and half-Heusler compounds have been integrated into TE device because of their high efficiency compared to most other thermoelectric materials [7-12]. However, these materials have limited applications owing to their high cost and toxicity. Therefore, many studies on alternative thermoelectric materials with high efficiency, low cost, and environmentally friendly characteristics have been reported. In recent years, tin selenide (SnSe) which contains non-toxic and earth-abundant elements has been considered as a promising TE material since Zhao et al. [13] reported a remarkable ZT value of ~2.6 at 923K (the world record to date) along the b-axis in its single crystal form. It, however, is still difficult to use single crystal TE materials in devices because of poor mechanical properties and high production cost [14]. For these reasons, the researches on SnSe have focused on developing high performance polycrystalline SnSe. The main limitation of undoped polycrystalline SnSe for TE applications originates from its lower

electrical and higher thermal conductivity than that of sing crystal SnSe [6]. Therefore, it is still a challenge to improve TE performance of polycrystalline SnSe. Many approaches to obtain polycrystalline SnSe which has TE performance similar to that of single crystal through texturing [15−18], doping [19−26], and nanoinclusion [27−32] have been reported. Polycrystalline SnSe has anisotropy structure, and its electrical/thermal properties are properties strongly depend on the crystal orientation. Previous reports [15, 19, 33, 34]. Showed that when texturing was applied, the anisotropy became stronger, which results in a better thermoelectric performance measured along the direction perpendicular to the pressure (⊥) than that measured along the direction parallel (//) to the pressure. However, the effect of texture on the TE properties of SnSe (which also has anisotropic TE properties) with all parameters other than the degree of texture kept constant, has not been reported.

In chapter 5. the degree of texture of polycrystalline SnSe was controlled by the pressure applied during spark plasma sintering (SPS), and the effects of sintering pressure on electrical transport and TE properties of the polycrystalline SnSe were investigated. With increasing sintering pressure, the degree of texture along the direction perpendicular to the pressure applied during the SPS were improved, which led to the increase in carrier mobility, which resulted

in the increase of the electrical conductivity. The When the pressure was increased, the total thermal conductivity was significantly increased by the increase of the lattice thermal conductivity which resulted from the decrease of the phonon scattering at the grain boundary. Increase in pressure led to a significant increase in thermal conductivity due to increase of the lattice thermal conductivity, which can be attributed to the decrease of the phonon scattering at the grain boundary. A ZT of ~0.7 was obtained at 823K from the polycrystalline SnSe, which was sintered with a pressure of 60MPa, which can be attributed to large increase in electrical conductivity with very small increase of the thermal conductivity

The electrical conductivity of SnSe can be significantly improved by doping with various doping is a useful method to control carrier concentration. Many dopants including Li [32], Na [32, 35, 36], K [37], Ca [14] Sr [14], Ba [14], Cu [14, 23], Ag [20, 38], Zn [14, 39], Al [23], In [21], Tl [40], Ge [41], Pb [23, 42], Te [43–45] and Sm [25] are used to improve the TE performance of polycrystalline SnSe. The TE performances of polycrystalline SnSe which was improved by doping, however, are still low compared to that of single crystal SnSe. One potential way to optimize the TE performance of polycrystalline SnSe is by making a solid solution which has been used in other TE materials such as $Bi_{2-x}Sb_xTe_3$, $Mg_2Si_{1-x}Sn$, and

$PbTe_{1-x}Se_x$ [46-48]. In solid solution system, electrical conductivity can be enhanced by optimizing carrier concentration through bandgap engineering while thermal conductivity can be suppressed by enhancing phonon scattering by atomic disorder and mass difference.

In chapter 6, the electrical transport and TE property of SnSe-SnTe solid solutions. Mechanical alloying (MA) and SPS were used to fabricate SnSe-SnTe sintered samples, respectively. hole carrier concentration is increased with increasing Te contents, led to the enhancement of electrical conductivity and reduction of Seebeck coefficient. The increase in hole carrier concentration is caused by a decrease in the band gap as Te replaces the Se site, which was confirmed by measuring the band gap energy and DFT calculating the band structure. Te has atomic mass and size larger than Se, and the presence of Te at Se site can act as an effective point defect, increasing phonon scattering and thus reducing lattice thermal conductivity. As a result, the ZT value of 0.78 at 823K was obtained in in $SnSe_{0.7}Te_{0.3}$, which is 11% higher than that of the SnSe.

TE properties of $SnSe_{0.7}Te_{0.3}$ can be more improved by making composites with secondary phases. Carbon nanotube (CNT) has been considered as a good candidate for embedding in TE matrix due to its dimensional structure and high electrical conductivity. The improvement of TE property has been reported in TE materials such

as Bi_2Te_3 [49], oxide-based [50] and organic TE materials [51] in which CNT is added as a secondary phase. We expected that when CNTs are well dispersed at the grain boundaries between $SnSe_{0.7}Te_{0.3}$, the electrical conductivity can be enhanced by formation of the electrical network of CNTs while the thermal conductivity can be suppressed by enhanced phonon scattering at CNT/matrix interfaces.

Finally, in chapter 6, Various amounts of CNT (0, 0.3, 0.6 and 1 wt %) were added to $SnSe_{0.7}Te_{0.3}$, which were sintered using SPS, and the effects of CNT addition on the charge transfer and TE properties of $SnSe_{0.7}Te_{0.3}$/CNT composites were investigated. CNTs are homogeneously distributed along the grain boundaries of $SnSe_{0.7}Te_{0.3}$. As the amount of CNTs increased, they formed networks, which led to the decrease in hole mobility, which resulted in reduction of hole mobility. Despite the decrease in mobility, high intrinsic hole concentration of CNT itself caused an increase in electrical conductivity and a decrease in Seebeck coefficient. when 0.3 wt% CNT was added, thermal conductivity decreased by interface phonon scattering, but when more CNT was added, the thermal conductivity increased again due to the high thermal conductivity of CNT itself. A ZT of ~ 0.86 at 823K was obtained from $SnSe_{0.7}Te_{0.3}$ with 0.3 wt% CNT.

1.1 References

[1] A. Demirbas, Global renewable energy projections, Energy Sources, Part B, 4 (2009) 212.

[2] F.J. DiSalvo, Thermoelectric cooling and power generation, Science, 285 (1999) 703.

[3] X. Zhu, Y. Yu, F. Li, A review on thermoelectric energy harvesting from asphalt pavement: Configuration, performance and future, Construction and Building Materials, 228 (2019) 116818.

[4] G.J. Snyder, E.S. Toberer, Complex thermoelectric materials, materials for sustainable energy: a collection of peer-reviewed research and review articles from Nature Publishing Group, World Scientific (2011) 101.

[5] S.K. Bux, J.-P. Fleurial, R.B. Kaner, Nanostructured materials for thermoelectric applications, Chemical Communications, 46 (2010) 8311.

[6] D.M. Rowe, Thermoelectrics handbook: macro to nano, CRC press (2018).

[7] G. Nolas, D. Morelli, T.M. Tritt, Skutterudites: A phonon-glass-electron crystal approach to advanced thermoelectric energy conversion applications, Annual Review of Materials Science, 29 (1999) 89.

[8] X. Zhang, L.-D. Zhao, Thermoelectric materials: Energy

conversion between heat and electricity, J. Materiomics, 1 (2015) 92.
[9] J. Yang, H. Li, T. Wu, W. Zhang, L. Chen, J. Yang, Evaluation of half-Heusler compounds as thermoelectric materials based on the calculated electrical transport properties, Advanced Functional Materials, 18 (2008) 2880.
[10] J.P. Heremans, V. Jovovic, E.S. Toberer, A. Saramat, K. Kurosaki, A. Charoenphakdee, S. Yamanaka, G.J. Snyder, Enhancement of thermoelectric efficiency in PbTe by distortion of the electronic density of states, Science, 321 (2008) 554.
[11] S. Bathula, M. Jayasimhadri, N. Singh, A. Srivastava, J. Pulikkotil, A. Dhar, R. Budhani, Enhanced thermoelectric figure−of−merit in spark plasma sintered nanostructured n−type SiGe alloys, Applied Physics Letters, 101 (2012) 213902.
[12] P. Rauwel, O.M. Løvvik, E. Rauwel, E.S. Toberer, G.J. Snyder, J. Taftø, Nanostructuring in β-Zn4Sb3 with variable starting Zn compositions, physica status solidi (a), 208 (2011) 1652.
[13] L.−D. Zhao, S.−H. Lo, Y. Zhang, H. Sun, G. Tan, C. Uher, C. Wolverton, V.P. Dravid, M.G. Kanatzidis, Ultralow thermal conductivity and high thermoelectric figure of merit in SnSe crystals, Nature, 508 (2014) 373.
[14] B.R. Ortiz, H. Peng, A. Lopez, P.A. Parilla, S. Lany, E.S. Toberer, Effect of extended strain fields on point defect phonon scattering in

thermoelectric materials, Physical Chemistry Chemical Physics, 17 (2015) 19410.

[15] Y. Fu, J. Xu, G.-Q. Liu, J. Yang, X. Tan, Z. Liu, H. Qin, H. Shao, H. Jiang, B. Liang, Enhanced thermoelectric performance in p-type polycrystalline SnSe benefiting from texture modulation, J. Mater. Chem. C, 4 (2016) 1201.

[16] D. Feng, Z.-H. Ge, D. Wu, Y.-X. Chen, T. Wu, J. Li, J. He, Enhanced thermoelectric properties of SnSe polycrystals via texture control, Physical Chemistry Chemical Physics, 18 (2016) 31821.

[17] S.R. Popuri, M. Pollet, R. Decourt, F.D. Morrison, N.S. Bennett, J.-W.G. Bos, Large thermoelectric power factors and impact of texturing on the thermal conductivity in polycrystalline SnSe, J. Mater. Chem. C, 4 (2016) 1685.

[18] X. Wang, J. Xu, G.-Q. Liu, X. Tan, D. Li, H. Shao, T. Tan, J. Jiang, Texturing degree boosts thermoelectric performance of silver-doped polycrystalline SnSe, NPG Asia Materials, 9 (2017) e426.

[19] S. Sassi, C. Candolfi, J.-B. Vaney, V. Ohorodniichuk, P. Masschelein, A. Dauscher, B. Lenoir, Assessment of the thermoelectric performance of polycrystalline p-type SnSe, Applied Physics Letters, 104 (2014) 212105.

[20] C.-L. Chen, H. Wang, Y.-Y. Chen, T. Day, G.J. Snyder,

Thermoelectric properties of p−type polycrystalline SnSe doped with Ag, Journal of Materials Chemistry A, 2 (2014) 11171.

[21] J.H. Kim, S. Oh, Y.M. Kim, H.S. So, H. Lee, J.−S. Rhyee, S.−D. Park, S.−J. Kim, Indium substitution effect on thermoelectric and optical properties of Sn1− xInxSe compounds, Journal of Alloys and Compounds, 682 (2016) 785.

[22] H.−Q. Leng, M. Zhou, J. Zhao, Y.−M. Han, L.−F. Li, The thermoelectric performance of anisotropic SnSe doped with Na, Rsc Advances, 6 (2016) 9112.

[23] N.K. Singh, S. Bathula, B. Gahtori, K. Tyagi, D. Haranath, A. Dhar, The effect of doping on thermoelectric performance of p−type SnSe: Promising thermoelectric material, Journal of Alloys and Compounds, 668 (2016) 152.

[24] J. Gao, G. Xu, Thermoelectric performance of polycrystalline Sn1−xCuxSe (x= 0–0.03) prepared by high pressure method, Intermetallics, 89 (2017) 40.

[25] J. Gao, H. Zhu, T. Mao, L. Zhang, J. Di, G. Xu, The effect of Sm doping on the transport and thermoelectric properties of SnSe, Materials Research Bulletin, 93 (2017) 366.

[26] Z.−H. Ge, D. Song, X. Chong, F. Zheng, L. Jin, X. Qian, L. Zheng, R.E. Dunin−Borkowski, P. Qin, J. Feng, Boosting the thermoelectric performance of (Na, K)−codoped polycrystalline SnSe by synergistic

tailoring of the band structure and atomic-scale defect phonon scattering, Journal of the American Chemical Society, 139 (2017) 9714.

[27] H. Guo, H. Xin, X. Qin, J. Zhang, D. Li, Y. Li, C. Song, C. Li, Enhanced thermoelectric performance of highly oriented polycrystalline SnSe based composites incorporated with SnTe nanoinclusions, Journal of Alloys and Compounds, 689 (2016) 87.

[28] Y.-M. Han, J. Zhao, M. Zhou, X.-X. Jiang, H.-Q. Leng, L.-F. Li, Thermoelectric performance of SnS and SnS-SnSe solid solution, Journal of Materials Chemistry A, 3 (2015) 4555.

[29] X.-Q. Huang, Y.-X. Chen, M. Yin, D. Feng, J. He, Origin of the enhancement in transport properties on polycrystalline SnSe with compositing two-dimensional material MoSe2, Nanotechnology, 28 (2017) 105708.

[30] H. Ju, J. Kim, Effect of SiC ceramics on thermoelectric properties of SiC/SnSe composites for solid-state thermoelectric applications, Ceramics International, 42 (2016) 9550.

[31] J. Li, D. Li, W. Xu, X. Qin, Y. Li, J. Zhang, Enhanced thermoelectric performance of SnSe based composites with carbon black nanoinclusions, Applied Physics Letters, 109 (2016) 173902.

[32] T.-R. Wei, G. Tan, X. Zhang, C.-F. Wu, J.-F. Li, V.P. Dravid, G.J. Snyder, M.G. Kanatzidis, Distinct impact of alkali-ion doping on

electrical transport properties of thermoelectric p-type polycrystalline SnSe, Journal of the American Chemical Society, 138 (2016) 8875.

[33] X. Shi, Z.-G. Chen, W. Liu, L. Yang, M. Hong, R. Moshwan, L. Huang, J. Zou, Achieving high Figure of Merit in p-type polycrystalline Sn0. 98Se via self-doping and anisotropy-strengthening, Energy Storage Materials, 10 (2018) 130.

[34] S. Li, X. Li, Z. Ren, Q. Zhang, Recent progress towards high performance of tin chalcogenide thermoelectric materials, Journal of Materials Chemistry A, 6 (2018) 2432.

[35] E.K. Chere, Q. Zhang, K. Dahal, F. Cao, J. Mao, Z. Ren, Studies on thermoelectric figure of merit of Na-doped p-type polycrystalline SnSe, Journal of Materials Chemistry A, 4 (2016) 1848.

[36] Y. Sun, Z. Zhong, T. Shirakawa, C. Franchini, D. Li, Y. Li, S. Yunoki, X.-Q. Chen, Rocksalt SnS and SnSe: Native topological crystalline insulators, Physical Review B, 88 (2013) 235122.

[37] Y.X. Chen, Z.H. Ge, M. Yin, D. Feng, X.Q. Huang, W. Zhao, J. He, Understanding of the extremely low thermal conductivity in high-performance polycrystalline SnSe through potassium doping, Advanced Functional Materials, 26 (2016) 6836.

[38] C.-H. Chien, C.-C. Chang, C.-L. Chen, C.-M. Tseng, Y.-R. Wu,

M.-K. Wu, C.-H. Lee, Y.-Y. Chen, Facile chemical synthesis and enhanced thermoelectric properties of Ag doped SnSe nanocrystals, RSC Advances, 7 (2017) 34300.

[39] J. Li, D. Li, X. Qin, J. Zhang, Enhanced thermoelectric performance of p-type SnSe doped with Zn, Scripta Materialia, 126 (2017) 6.

[40] V. Kucek, T. Plechacek, P. Janicek, P. Ruleova, L. Benes, J. Navratil, C. Drasar, Thermoelectric properties of Tl-doped SnSe: a hint of phononic structure, Journal of Electronic Materials, 45 (2016) 2943.

[41] M. Gharsallah, F. Serrano-Sánchez, N. Nemes, F. Mompeán, J. Martínez, M. Fernández-Díaz, F. Elhalouani, J. Alonso, Giant seebeck effect in Ge-doped SnSe, Scientific reports, 6 (2016) 26774.

[42] Y.K. Lee, K. Ahn, J. Cha, C. Zhou, H.S. Kim, G. Choi, S.I. Chae, J.-H. Park, S.-P. Cho, S.H. Park, Enhancing p-type thermoelectric performances of polycrystalline SnSe via tuning phase transition temperature, Journal of the American Chemical Society, 139 (2017) 10887.

[43] T.-R. Wei, C.-F. Wu, X. Zhang, Q. Tan, L. Sun, Y. Pan, J.-F. Li, Thermoelectric transport properties of pristine and Na-doped SnSe 1- x Te x polycrystals, Physical Chemistry Chemical Physics, 17 (2015) 30102.

[44] M. Hong, Z.-G. Chen, L. Yang, T.C. Chasapis, S.D. Kang, Y. Zou, G.J. Auchterlonie, M.G. Kanatzidis, G.J. Snyder, J. Zou, Enhancing the thermoelectric performance of SnSe 1− x Te x nanoplates through band engineering, Journal of Materials Chemistry A, 5 (2017) 10713.

[45] S. Chen, K. Cai, W. Zhao, The effect of Te doping on the electronic structure and thermoelectric properties of SnSe, Physica B: Condensed Matter, 407 (2012) 4154.

[46] V. Zaitsev, M. Fedorov, E. Gurieva, I. Eremin, P. Konstantinov, A.Y. Samunin, M. Vedernikov, Highly effective Mg 2 Si 1− x Sn x thermoelectrics, Physical Review B, 74 (2006) 045207.

[47] Y. Pei, X. Shi, A. LaLonde, H. Wang, L. Chen, G.J. Snyder, Convergence of electronic bands for high performance bulk thermoelectrics, Nature, 473 (2011) 66.

[48] X. Yan, B. Poudel, Y. Ma, W. Liu, G. Joshi, H. Wang, Y. Lan, D. Wang, G. Chen, Z. Ren, Experimental studies on anisotropic thermoelectric properties and structures of n−type Bi2Te2. 7Se0. 3, Nano letters, 10 (2010) 3373.

[49] K.T. Kim, S.Y. Choi, E.H. Shin, K.S. Moon, H.Y. Koo, G.-G. Lee, G.H. Ha, The influence of CNTs on the thermoelectric properties of a CNT/Bi2Te3 composite, Carbon, 52 (2013) 541.

[50] G. Tang, W. Yang, J. Wen, Z. Wu, C. Fan, Z. Wang, Ultralow thermal conductivity and thermoelectric properties of carbon

nanotubes doped Ca3Co4O9+δ, Ceramics International, 41 (2015) 961.

[51] Q. Zhang, W. Wang, J. Li, J. Zhu, L. Wang, M. Zhu, W. Jiang, Preparation and thermoelectric properties of multi-walled carbon nanotube/polyaniline hybrid nanocomposites, Journal of Materials Chemistry A, 1 (2013) 12109.

CHAPTER 2. General Background

2.1 Thermoelectricity and Thermoelectric Effects

Due to the depletion of the fossil fuels and its environmental pollution, the demand for alternative and renewable energy has become a world issues. Figure 2-1 shows the energy use in the US in 2018, conducted by the Lawrence Livermore National Laboratory [1]. As shown in Figure 2-1, The energy efficiency used in US is only about 32.7%, and more than 60% of the energy is lost to heat. Therefore, in order to increase energy efficiency, it is important to recovery the waste heat, and Thermoelectricity technology can make it possible. Thermoelectricity includes the collective effects that involve the conversion of a temperature difference to electric voltage and vice versa [2] and it can be used for both power generation and electronic refrigeration. The use of thermoelectric (TE) device has many advantages, such as such as simple structure, no moving part, high durability, high precision, and compactness, as well as being an excellent way of collecting wasted heat energy, and also the possibility of use in a clean cogeneration process. [3]. TE effects are subdivided into the Seebeck, Peltier, and Thomson effects [4, 5]. In 1821, the Thomas Johann Seebeck first discovered the TE effects [6]. He observed that when temperature difference is applied

between the ends of two dissimilar semiconductors, which are connected electrically in series but thermally in parallel, the electrons are moved to the lower energy region and holes are moved to the other region, which generate the electrical voltage, which is proportional to the temperature differences [3], as shown in figure 2-2. The Seebeck efficiency is characterized by the Seebeck coefficient S, which is defined by the ratio of the electric voltage and temperature differences.

$$S = \frac{\Delta V}{\Delta T} \tag{2.1}$$

where S, ΔV, and ΔT are the Seebeck coefficient, voltage gradient, and temperature gradient, respectively. The sign of the Seebeck coefficient is determined by the type of majority charge carriers (positive for a p-type material and negative for an n-type material) [7].

The Peltier effect, which is the opposite effect to the Seebeck, was discovered by Jean Charles Athanase Peltier in 1834. He observed that when a direct current I (A) flows in the circuit composed of two dissimilar materials it causes the junction to cool or heat as a function of the current direction [8], as shown in figure 2-3. The Peltier effect is defined as the ratio of the rate of heating or cooling to the

electrical current passing through the junction and expressed as Eq. 2.2

$$\pi = \frac{Q}{I} \tag{2.2}$$

where π, Q, and I are the Peltier coefficient, heat released or absorbed per unit time at the junction, and applied current, respectively [9].

The last of TE effects, the Thomson effect was discovered by William Thomson (Lord Kelvin) in 1854, and it is related to the rate of generation of reversible heat which results from the passage of a current along a portion of a single conductor along which there is a temperature difference, as shown in figure 2-4 [4]. He observed that the amount of heat exchanged is proportional to both the electric current and the temperature differences, and that their mutual direction determines if the heat is absorbed or released, which is determined by the Thomson coefficient (Eq. 2.3)

$$dQ = \beta \cdot I \cdot dT \tag{2.3}$$

where dQ, β, I, and dT are the rate of heat generation, Thomson coefficient, applied current, and temperature gradient, respectively. The units of β are the same as those of the Seebeck coefficient V/K.

Although the Thomson effect is not of primary importance in TE devices it should not be neglected in detailed calculations.

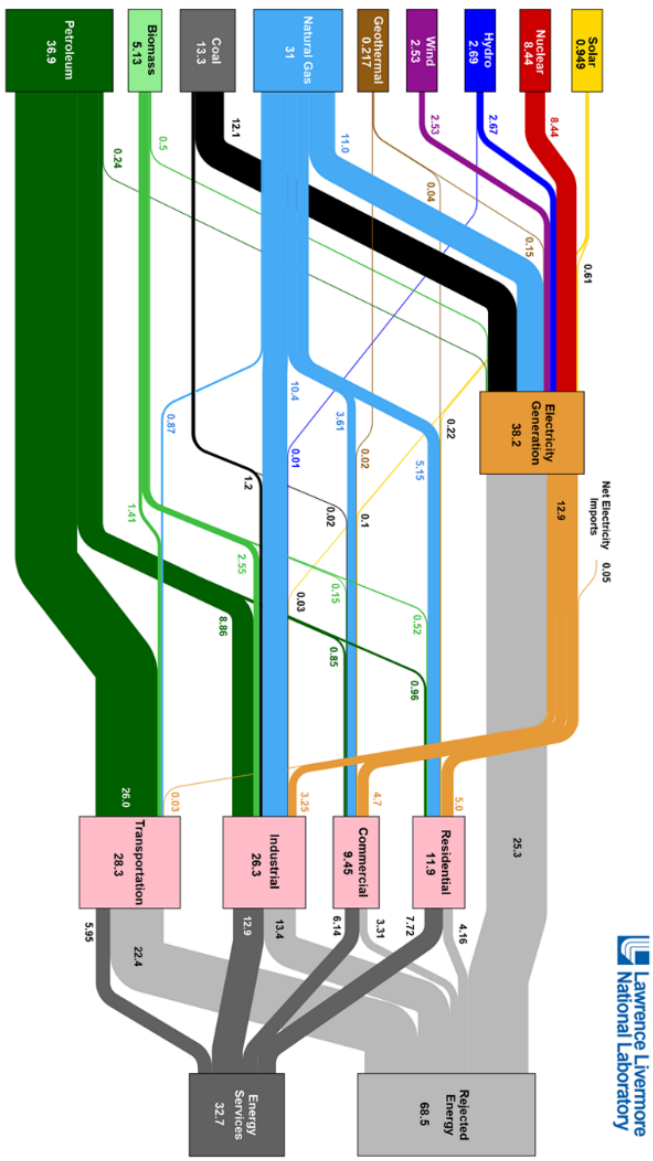

Figure 2-1. The flow chart of energy used in US in 2018 which is conducted by the Lawrence Livermore National Laboratory [1].

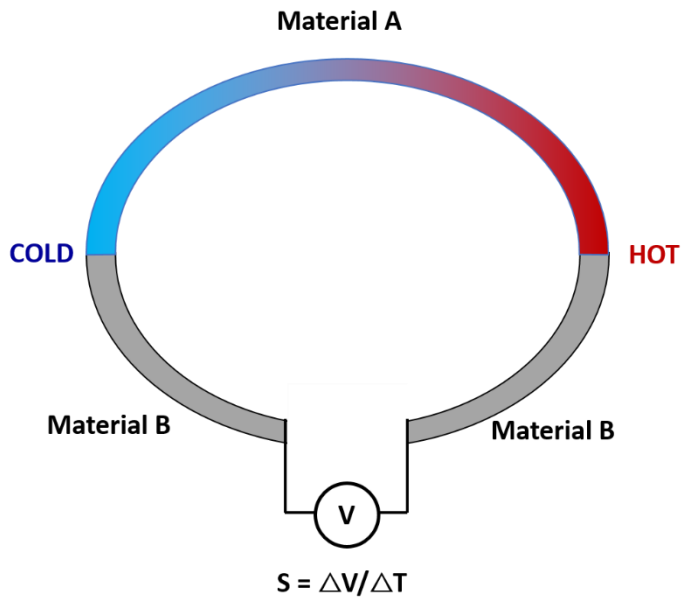

Figure 2-2. A Schematic of Seebeck effect

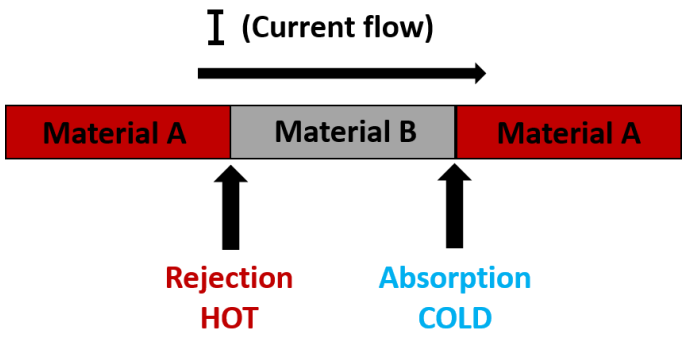

Figure 2-3. A schematic of Peltier effect

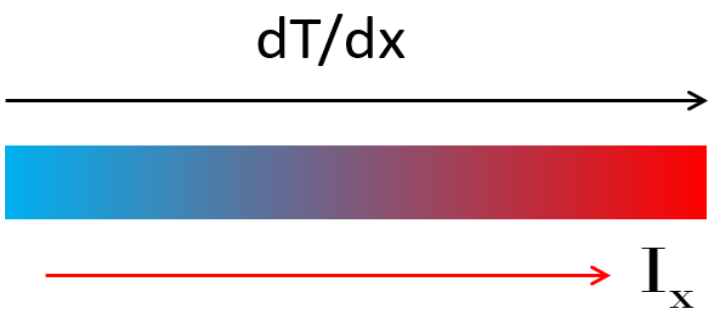

Figure 2-4. A schematic of Thomson effect

2.2 Efficiency and Figure of Merit (ZT) of Thermoelectric

A single Thermoelectric (TE) device consist of a p−type and n−type TE materials connected electrically in series and thermally in parallel [4, 10], it is shown in figure 2−5. The temperatures of the heat source and sink are T_C and T_H, respectively. When heat flows to heat sink through the p−n junction, current (I) passes in the TE device. Assuming no energy loss in the TE device, the efficiency of a TE device is determined by the ratio of electrical energy supplied to the load to heat energy absorbed at a heat source and is expressed by Eq. 2.4. [4]

$$\eta = \frac{P}{Q_H} \tag{2.4}$$

where P and Q_H are the electrical power output and the input heat required at the hot junction to maintain the junction at T_H, respectively. In order to calculate the efficiency of TE device, the electrical energy supplied to load P should be known, and it can be obtained by the difference in the thermal energy absorbed at the hot side Q_H and the thermal energy released at the cold side Q_C. Q_H and Q_C can be represented by Eq. 2.5 and 2.6, respectively.

$$Q_H = \Delta \mathrm{S} \mathrm{T}_H I - \frac{I^2 R}{2} + \kappa \Delta \mathrm{R} \mathrm{T} \tag{2.5}$$

$$Q_C = \Delta \mathrm{S} \mathrm{T}_C I - \frac{I^2 R}{2} + \kappa \Delta \mathrm{R} \mathrm{T} \tag{2.6}$$

where △S is the difference in the Seebeck coefficient between *p* and *n*–type TE materials, R is the internal electrical resistance, *I* is the current supplied to the load, and *k* is the thermal conductivity, respectively. If it is assumed that there is no energy loss inside the system, the P is the difference between the heat input from the hot side and the heat output to cold side, which can be presented by Eq. 2.7.

$$\mathrm{P} = \mathrm{Q}_H - \mathrm{Q}_\mathrm{C} = \left(\Delta \mathrm{S} \mathrm{T}_H - RI\right) I = I^2 R_L \tag{2.7}$$

where R_L is the resistance of the load, and thus the efficiency of the TE device (see Eq. 2.4) can be rewritten as Eq. 2.8.

$$\eta = \frac{P}{Q_H} = \frac{R_L S^2 \Delta T / (R + R_L)^2 + S}{\Delta S T_H I - \frac{I^2 R}{2} + \kappa \Delta T} \tag{2.8}$$

If the value of R_L/R is defined as *m*, and it is same as Eq. 2.9

$$\eta = \frac{\Delta \mathrm{T}}{\mathrm{T}_\mathrm{h}} \cdot \frac{\frac{\mathrm{m}}{1+\mathrm{m}}}{1 + \frac{1+\mathrm{m}}{\mathrm{ZT}_\mathrm{h}} - \frac{\Delta \mathrm{T}}{\mathrm{ZT}_\mathrm{h}(1+\mathrm{m})}} \tag{2.9}$$

The maximum efficiency can be obtained from the local maximum

where $\partial \eta / \partial m$ is '0'. To calculate the maximum efficiency, Maximum value we need to find the local maximum where $\partial \eta / \partial m$ is '0'. If Eq. 2.9 is taken as a partial derivative, the maximum value of m is expressed as M, Eq. 2.10 is obtained.

$$\left(\frac{R}{r}\right) = \sqrt{1+ZT} = M \tag{2.10}$$

Substituting the value of M into the previously calculated efficiency η, the final efficiency is as following Eq. 2.11.

$$\eta_{max} = \frac{\Delta T}{T_h} \cdot \frac{\sqrt{1+ZT}-1}{\sqrt{1+ZT}+\left(\frac{T_c}{T_h}\right)} \tag{2.11}$$

The ZT is called dimensionless figure of merit for evaluating the performance of TE device, and the unit is the inverse of temperature. ZT can be expressed by $ZT = S^2 \sigma T/k$, where S, σ, T and k are the Seebeck coefficient, electrical conductivity, absolute temperature, and thermal, respectively [11, 12]. Therefore, high Seebeck coefficient, high electrical conductivity, and low thermal conductivity are required to achieve high ZT value. However, all those parameters have complex interrelationships [4]. The dependence of parameters on the carrier concentration is plotted in Figure 2-6. For example, the higher carrier concentration leads to larger electrical conductivity (σ), but is negative to the Seebeck coefficient (S). And it is also difficult to solely suppress thermal conductivity without deteriorating

the electrical conductivity. Therefore, the optimization of the carrier concentration is needed to improve the efficiency of a TE material for practical application. It is generally known that the optimized carrier concentration typically is between 10^{19} and 10^{21} cm^{-3}, indicating that heavily doped semiconductors are best for the thermoelectric materials. And also the effort to find TE materials which have performance high enough to be used in devices, which consist of earth-abundant and non-toxic elements, is continuing today.

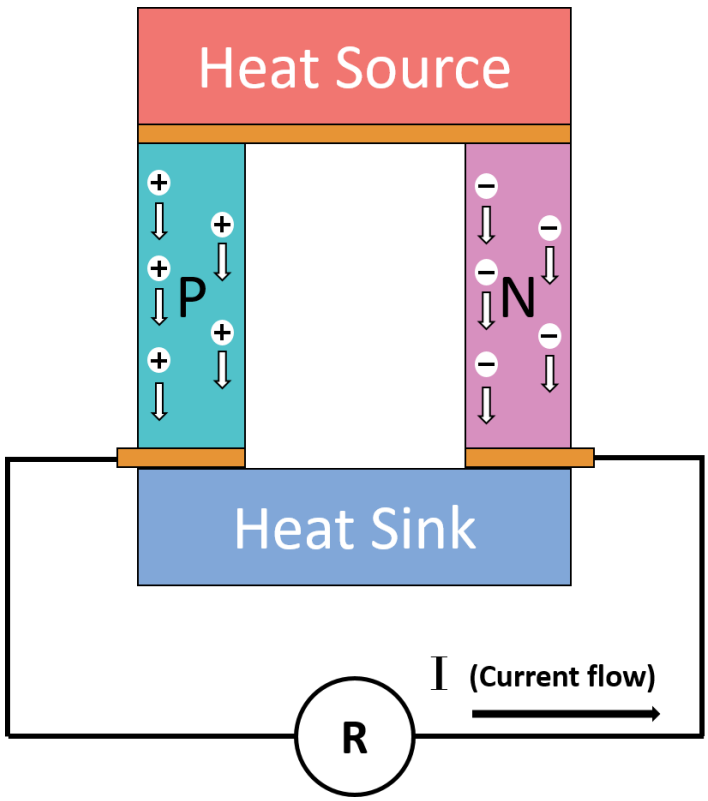

Figure 2-5. A schematic of a single thermoelectric device consisted of *p*- and *n*- type thermoelectric materials

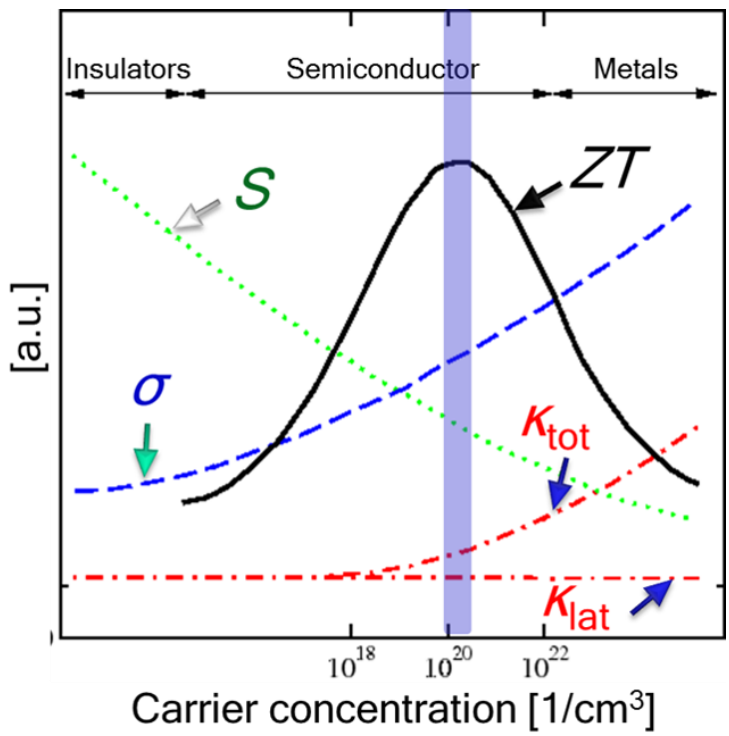

Figure 2-6. The dependence of ZT parameters on carrier concentration

2.3 Commercial and Alternative Thermoelectric Material

Over the past several decades, many thermoelectric (TE) materials, including alloy semiconductors such as Bi_2Te_3, PbTe and SiGe, have been integrated into conventional power generation and refrigeration [13-19]. As mentioned in chapter 2.2, the TE device consist of n- and p-type TE materials. Figure 2-7 shows the temperature-dependent ZT of commercially used *n*- and *p*-type thermoelectric materials [20]. It revealed that TE materials have a different temperature range showing high TE performance, so TE materials can be classified into the low temperature, the mid-temperature, and the high temperature TE material according to the temperature in use.

For near room temperature (~ 450K) applications such as waste heat generation and refrigeration, Bi_2Te_3 based TE materials are the most widely used TE material due to its greatest figure of merit for both n- and p-type TE systems. For mid-temperature (450 ~ 900K), the materials based on group-IV tellurides such as PbTe and GeTe are typically used for waste heat recovery of automotive or plants. For high temperature (> 900K) application, SiGe based TE materials are used for the field of space. Despite the high

performance of TE materials such as Bi_2Te_3 and PbTe, they have limited applications because of their high cost and toxicity. Figure 2-8 shows the price of elements is plotted as a function of abundance [21]. It showed that Co, Bi, Sb, Se, and Te, which constitutes the commercial TE materials, are ex expensive and have low abundance, whereas Pb is toxic and has low abundance.

Figure 2-9 and 2-10 show the ZT of the current bulk thermoelectric materials as a function of year and the ZT values of different classes of materials over a range of temperatures, respectively. [14, 22]. Many efforts have been made to obtain alternative the TE material, which is with high performance, low cost, and eco-friendly. [14]. Among the alternative TE materials, SnSe has been considered as one of the most promising TE material, since reported the highest ZT value (2.6 at 923 K) in single crystalline form, comparable with commercial thermoelectric materials [22].

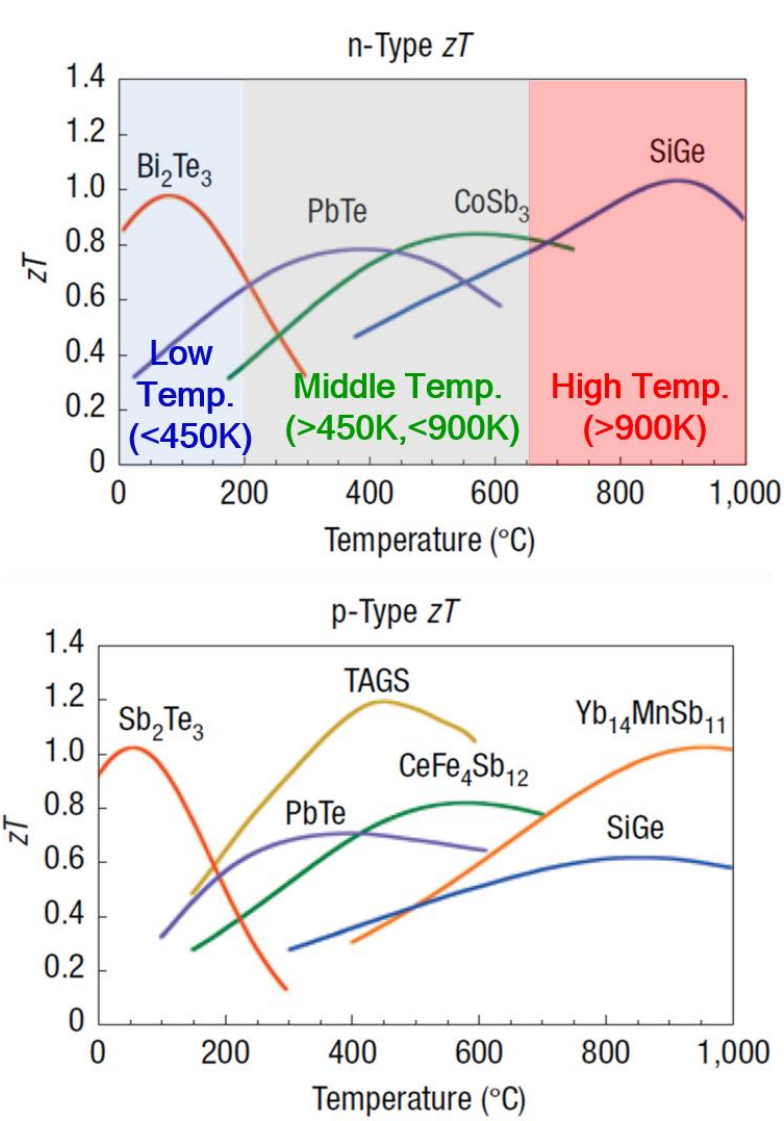

Figure 2-7. Temperature-dependent ZT of n- and p- type thermoelectric materials used commercially.

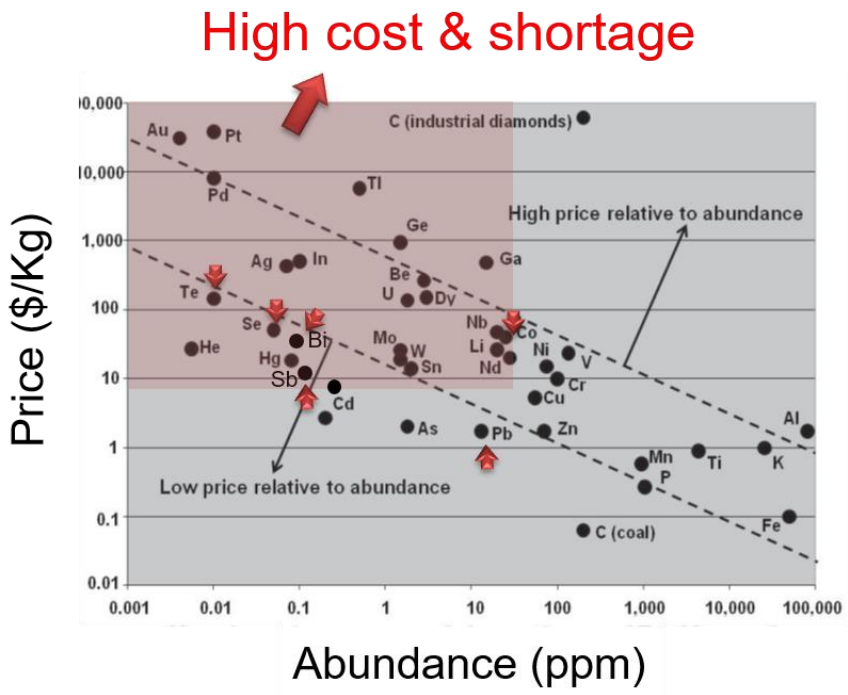

Figure 2-8. Price versus abundance for selected elements. Prices are mostly averages for the year 2009 from U.S. Geological Survey (2010)

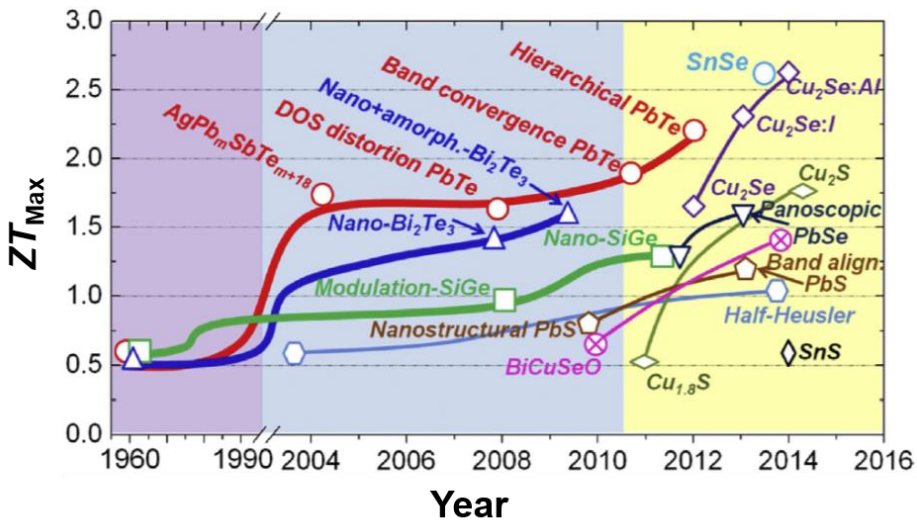

Figure 2-9. ZT of the current bulk thermoelectric materials as a function of year: The left part indicates the three conventional thermoelectric systems with ZT < 1.0 before 1990s, the middle part elucidates that the ZTs were enhanced to about 1.7 by nanostructures, and the right part shows the high performance realized in promising thermoelectric materials developed recently and characterized by low-cost, earth-abundant, and low thermal conductivity [14].

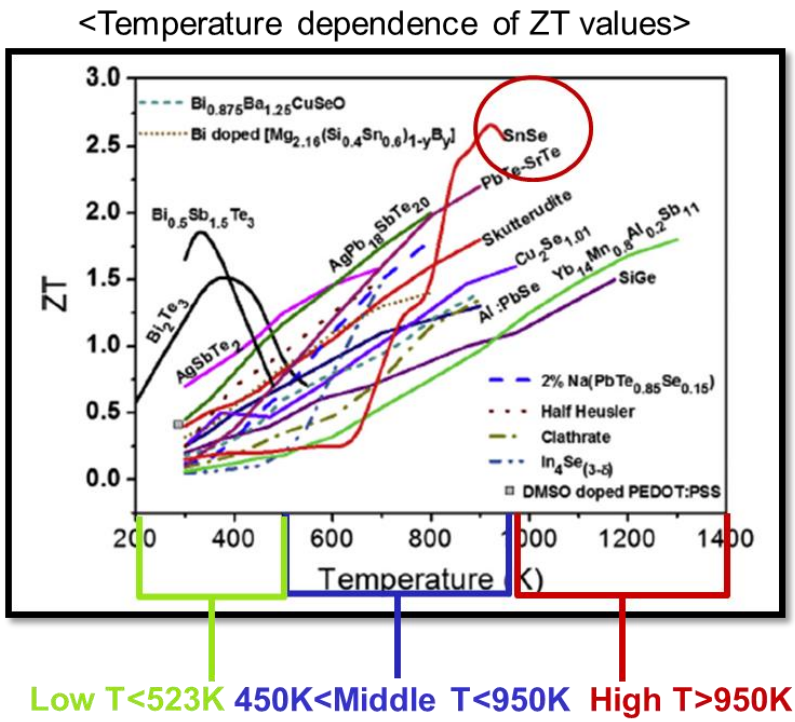

Figure 2-10. Dimensionless figure of merit ZT vs temperature of typical current thermoelectric materials.

2.4 References

[1] Lawrence Livermore National Laboratory-Energy flow chart (2018).

[2] D.T. Morelli, Thermoelectric Materials, in: S. Kasap, P. Capper (Eds.) Springer Handbook of Electronic and Photonic Materials, Springer International Publishing, Cham, (2017).

[3] O.A. Junior, A. Maran, N.J.R. Henao, S.E. Reviews, A review of the development and applications of thermoelectric microgenerators for energy harvesting, 91 (2018) 376.

[4] D.M. Rowe, Thermoelectrics handbook: macro to nano, CRC press (2018).

[5] H.J. Goldsmid, Introduction to thermoelectricity, Springer2010.

[6] C. Goupil, H. Ouerdane, K. Zabrocki, W. Seifert, N.F. Hinsche, E.J.C.T. Müller, M.o.T. Elements, Thermodynamics and thermoelectricity, (2015).

[7] D.J.E.C. Champier, Management, Thermoelectric generators: A review of applications, 140 (2017) 167

[8] J. Martins, F.P. Brito, L. Goncalves, J. Antunes, Thermoelectric exhaust energy recovery with temperature control through heat pipes, (2011).

[9] A. Montecucco, A.R.J.A.e. Knox, Accurate simulation of

thermoelectric power generating systems, 118 (2014) 166.

[10] K.M. Saqr, M.N.J.T.S. Musa, Critical review of thermoelectrics in modern power generation applications, 13 (2009) 165.

[11] B. Sherman, R. Heikes, R.J.J.o.A.P. Ure Jr, Calculation of efficiency of thermoelectric devices, 31 (1960) 1.

[12] M.J.J.o.A.P. Telkes, The Efficiency of Thermoelectric Generators. I, 18 (1947) 1116.

[13] P.J. Taroni, I. Hoces, N. Stingelin, M. Heeney, E.J.I.J.o.C. Bilotti, Thermoelectric materials: A brief historical survey from metal junctions and inorganic semiconductors to organic polymers, 54 (2014) 534.

[14] X. Zhang, L.-D. Zhao, Thermoelectric materials: Energy conversion between heat and electricity, Journal of Materiomics, 1 (2015) 92.

[15] K.F. Hsu, S. Loo, F. Guo, W. Chen, J.S. Dyck, C. Uher, T. Hogan, E. Polychroniadis, M.G. Kanatzidis, Cubic AgPbmSbTe2+ m: bulk thermoelectric materials with high figure of merit, Science, 303 (2004) 818.

[16] B. Poudel, Q. Hao, Y. Ma, Y. Lan, A. Minnich, B. Yu, X. Yan, D. Wang, A. Muto, D. Vashaee, High-thermoelectric performance of nanostructured bismuth antimony telluride bulk alloys, Science, 320 (2008) 634.

[17] W. Xie, X. Tang, Y. Yan, Q. Zhang, T.M. Tritt, Unique nanostructures and enhanced thermoelectric performance of melt-spun BiSbTe alloys, Applied Physics Letters, 94 (2009) 102111.

[18] S. Bathula, M. Jayasimhadri, N. Singh, A. Srivastava, J. Pulikkotil, A. Dhar, R. Budhani, Enhanced thermoelectric figure-of-merit in spark plasma sintered nanostructured n-type SiGe alloys, Applied Physics Letters, 101 (2012) 213902.

[19] B. Yu, M. Zebarjadi, H. Wang, K. Lukas, H. Wang, D. Wang, C. Opeil, M. Dresselhaus, G. Chen, Z. Ren, Enhancement of thermoelectric properties by modulation-doping in silicon germanium alloy nanocomposites, Nano letters, 12 (2012) 2077.

[20] G.J. Snyder, E.S. Toberer, Complex thermoelectric materials, materials for sustainable energy: a collection of peer-reviewed research and review articles from Nature Publishing Group, World Scientific (2011) 101.

[21] J.G.J.G.T. Price, The world is changing, 26 (2016).

[22] C. Gayner, K.K. Kar, Recent advances in thermoelectric materials, Progress in Materials Science, 83 (2016) 330.

CHAPTER 3. Reviews of Thermoelectric Material SnSe

3.1. General Properties of SnSe

SnSe is an inorganic compound semiconductor [1], that has a Molar mass of 197.67 g/mol, a theoretical density of 6.179 g/cm^3 at room temperature [2], and a melting point of 1134 K [3]. SnSe has two stable phases: α−SnSe (T<~800 K) and β−SnSe (T>~800 K). These two phases possess a similar crystal structure (orthogonal), but different lattice parameters and space groups, as summarized in Table 3−1. Figure 3−2 (a)−(d) and figure 3−3 (a)−(d) shows the atomic structure of α−SnSe in a unit cell, and Figure 3(b)−(d) show the projected crystal structure of α−SnSe viewed along the a−, b−, and c−axes, respectively. At 750 K, SnSe undergoes a structural transition from space group *Pnma* to space group *Cmcm*. The low−temperature orthorhombic *Pnma* phase (a = 11.490 Å, b = 4.440 Å, c = 4.135 Å) has an indirect band gap E_g = 0.86 ~ 1 eV at 300 K, and the high−temperature *Cmcm* phase has a direct band gap E_g = 0.46 eV [4−6]. It typically behaves as a p−type material with a hole concentration in the range 10^{17}1018 cm3 and a room temperature electrical resistivity between 10^{17} ~ 10^{18} cm^{-3} and a room temperature electrical resistivity between 10 ~ 10^5 Ω cm. [7] SnSe had been ignored from a TE point of view because of the large

electrical resistivity and has been more useful for applications in solar cells, optoelectronics and other electronic devices. [8] Recently, however, SnSe, which is composed of nontoxic and abundant elements, has come to be considered a promising candidate TE material for practical applications. The potential of SnSe has attracted a great deal of attention since Zhao et al. [9] reported the high ZT value of ~2.6 at 923 K in single crystal SnSe, which is larger than the values of other state-of-the-art TE materials.

Table 3-1. Crystal structure data of SnSe system [10, 11]

Phase	Pearson symbol	Space group	S. D.	Lattice Parameters (Å)	Prototype
α-SnSe	oP8	Pnma	B16	a=11.37, b=4.19, c=4.44	GeS
β-SnSe	oC8	Cmcm	B	a=4.31, b=11.71, c=4.32	CrB

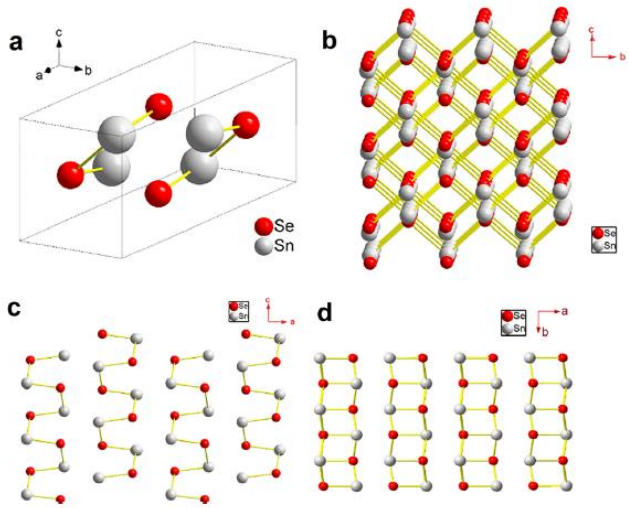

Figure 3-1. (a) Unit cell of α-SnSe and crystal structure along (b) a-axis, (c) b-axis, and (d) c-axis.

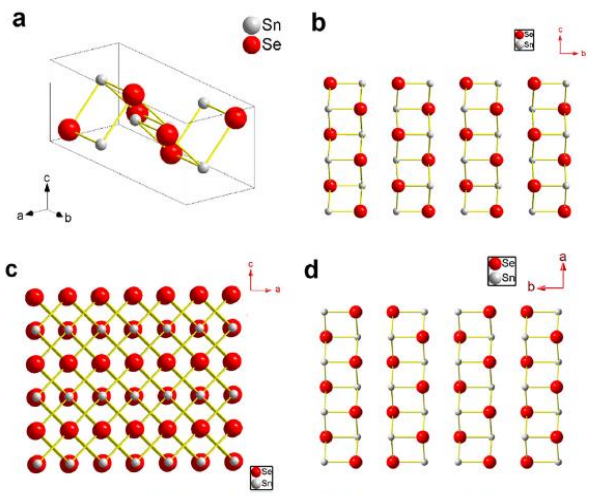

Figure 3-2. (a) Unit cell of β-SnSe and crystal structure along (b) a-axis, (c) b-axis, and (d) c-axis.

3.2 Advantage of SnSe for Thermoelectric Applications

SnSe has been received significant attentions as one of the promising middle-temperature (600-900 K) thermoelectric (TE) materials since in 2010, Zhao *et al.* [9] reported a high ZT value of 2.6 at 923 K in single crystal SnSe prepared by using the Bridgman technique; this ZT is larger than the values of other state-of-the-art TE materials.

SnSe compounds have an intrinsically high Seebeck coefficient. Figure 3-3 shows the comparison of the Seebeck coefficients for SnSe and other TE materials [12]. Seebeck coefficient of SnSe is significantly higher than that of other TE materials. SnSe also has a ultralow lattice thermal conductivity [9]. Figure 3-4 shows the comparison of the thermal conductivity for SnSe and other TE materials [12-15]. It was confirmed that the Seebeck coefficient of SnSe is significantly lower than that of other. The high ZT value of SnSe is due to its moderate power factor and ultralow thermal conductivity (lowest among any bulk materials being 0.23 W/m·K along the *a*-axis at 973 K).

Figure 3-5 shows the number of the publications related to SnSe. Since the high TE performance of single crystal SnSe has been reported, research on SnSe TE materials continues to increase.

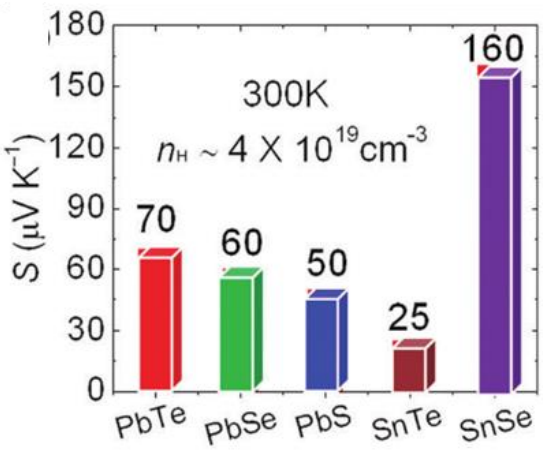

Figure 3-3. The comparison of Seebeck coefficient for SnSe and other thermoelectric materials

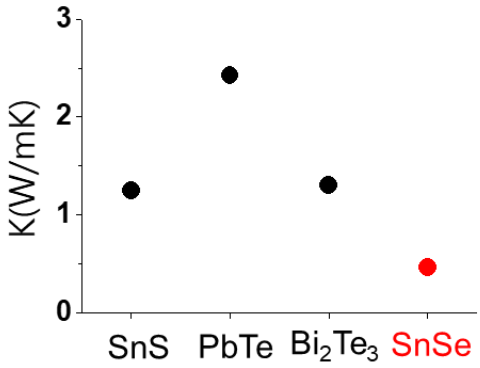

Figure 3-4. The comparison of Seebeck coefficient for SnSe and other thermoelectric materials

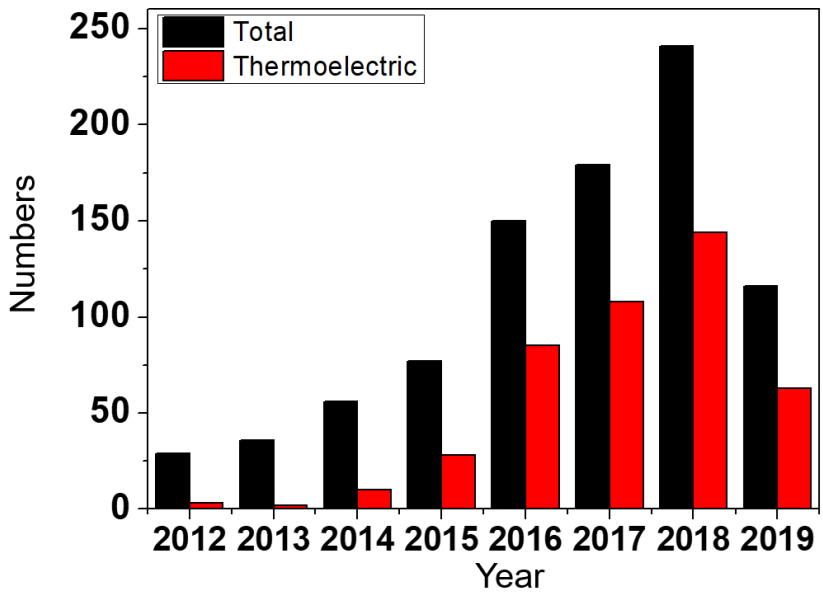

Figure 3-5. The number of articles published related to SnSe. (Search source; Web of science, keyword; SnSe is used for total. SnSe & thermoelectric were used for thermoelectric).

3.3 Disadvantage of SnSe for Thermoelectric

Applications

Recently, a new material has drawn the attention of the thermoelectric (TE) scientific community, with the description of a record-high ZT value of 2.6 at 923K in single crystalline SnSe semiconductor [9]. In fact, this compound had been known for a long time but its TE parameters were evaluated as poor [16, 17]. Indeed, the unusually high values reported for single-crystalline SnSe correspond to the threshold temperature of a structural phase transition at 820K from the low-temperature structure, defined in the Pnma space group, and consisting of corrugated layers of a NaCl like arrangement of $SnSe_3$ (and $SeSn_3$) units, to a Cmcm structure which is prone to decompose by Se evaporation [18, 19]. Figure 3-6 shows the TE properties of single crystalline SnSe and polycrystalline SnSe, respectively. In polycrystalline specimens, the reported properties for single crystal materials have not been reproduced [18], where ZT values reach 0.5 at 820K. Also, different chemical substitutions in this compound in both the Sn and Se sublattices have led to some improvement of certain parameters [20, 21]. The fact that SnSe is a semiconductor with a low intrinsic defect concentration drove some authors to increase the concentration of extra free carriers, However, this material presents some disadvantages that could impede its application i) SnSe is difficult to

prepare in single crystalline form, and hard to handle, as it is prone to cleave [9, 22], ii) the preparation described for polycrystalline samples requires long annealing times followed by spark−plasma sintering processes, leading to inhomogeneous phases where the segregation of Sn is frequently observed [9, 16] and which is also difficult to scale−up, iii) the defects introduced by the synthesis methods and minor impurities have a strong impact on the number of carriers and hence on the Seebeck coefficient and electronic conductivity, leading to a dispersion of the reported data in the literature [20].

Figure 3-6. Comparison of Thermoelectric Properties of Monocrystalline SnSe and Polycrystalline SnSe.

3.4 References

[1] A.A. Khan, I. Khan, I. Ahmad, Z. Ali, Thermoelectric studies of IV–VI semiconductors for renewable energy resources, Materials Science in Semiconductor Processing, 48 (2016) 85.

[2] T. Chattopadhyay, J. Pannetier, H. Von Schnering, Neutron diffraction study of the structural phase transition in SnS and SnSe, Journal of Physics and Chemistry of Solids, 47 (1986) 879.

[3] S. Vyas, G. Pandya, C. Desai, Microhardness studies on cleavage planes of SnS and SnSe single crystals, Indian journal of pure & applied physics, 33 (1995) 191.

[4] B. Subramanian, C. Sanjeeviraja, M. Jayachandran, Brush plating of tin (II) selenide thin films, Journal of Crystal Growth, 234 (2002) 421.

[5] M. Parenteau, C. Carlone, Influence of temperature and pressure on the electronic transitions in SnS and SnSe semiconductors, Physical Review B, 41 (1990) 5227.

[6] G. Shi, E. Kioupakis, Quasiparticle band structures and thermoelectric transport properties of p-type SnSe, Journal of Applied Physics, 117 (2015) 065103.

[7] A. Agarwal, M. Vashi, D. Lakshminarayana, N.J.J.o.M.S.M.i.E. Batra, Electrical resistivity anisotropy in layered p-SnSe single crystals, 11 (2000) 67.

[8] L.-D. Zhao, C. Chang, G. Tan, M.G.J.E. Kanatzidis, E. Science, SnSe: a remarkable new thermoelectric material, 9 (2016) 3044.

[9] L.-D. Zhao, S.-H. Lo, Y. Zhang, H. Sun, G. Tan, C. Uher, C. Wolverton, V.P. Dravid, M.G. Kanatzidis, Ultralow thermal conductivity and high thermoelectric figure of merit in SnSe crystals, Nature, 508 (2014) 373.

[10] R. Sharma, Y. Chang, The Se- Sn (selenium-tin) system, Journal of Phase Equilibria, 7 (1986) 68.

[11] H. Okamoto, Se-Sn (selenium-tin), Journal of phase equilibria, 19 (1998) 293.

[12] L.-D. Zhao, C. Chang, G. Tan, M.G. Kanatzidis, SnSe: a remarkable new thermoelectric material, Energy & Environmental Science, 9 (2016) 3044.

[13] Q. Tan, L.-D. Zhao, J.-F. Li, C.-F. Wu, T.-R. Wei, Z.-B. Xing, M.G. Kanatzidis, Thermoelectrics with earth abundant elements: low thermal conductivity and high thermopower in doped SnS, Journal of Materials Chemistry A, 2 (2014) 17302.

[14] B. Paul, P. Banerji, Embedded Ag-rich nanodots in PbTe: Enhancement of thermoelectric properties through energy filtering of the carriers, Journal of Applied Physics, 108 (2010) 064322.

[15] D.M. Rowe, Thermoelectrics handbook: macro to nano, CRC press (2018).

[16] J. Wasscher, W. Albers, C. Haas, Simple evaluation of the

maximum thermoelectric figure of merit, with application to mixed crystals SnS1−xSex, Solid−State Electronics, 6 (1963) 261.

[17] J.G. Yu, A. Yue, O. Stafsudd Jr, Growth and electronic properties of the SnSe semiconductor, Journal of Crystal Growth, 54 (1981) 248.

[18] X. Zhang, L.−D. Zhao, Thermoelectric materials: Energy conversion between heat and electricity, J. Materiomics, 1 (2015) 92.

[19] S. Sassi, C. Candolfi, J.−B. Vaney, V. Ohorodniichuk, P. Masschelein, A. Dauscher, B. Lenoir, Assessment of the thermoelectric performance of polycrystalline p−type SnSe, Applied Physics Letters, 104 (2014) 212105.

[20] C.−L. Chen, H. Wang, Y.−Y. Chen, T. Day, G.J. Snyder, Thermoelectric properties of p−type polycrystalline SnSe doped with Ag, Journal of Materials Chemistry A, 2 (2014) 11171.

[21] S. Chen, K. Cai, W. Zhao, The effect of Te doping on the electronic structure and thermoelectric properties of SnSe, Physica B: Condensed Matter, 407 (2012) 4154.

[22] H. Wiedemeier, H. Georg, G. von Schnering, Refinement of the structures of GeS, GeSe, SnS and SnSe, Zeitschrift für Kristallographie−Crystalline Materials, 148 (1978) 295.

CHAPTER 4. Experimental

4.1 Mechanical alloying (MA)

Mechanical alloying (MA) is a solid-state powder processing technique involving repeated cold welding, fracturing, and rewelding of powder particles in a high-energy ball mill [1]. It was developed in the mid-1960 by Benjamin at the International Nickel Company (INCO) to introduce hard particles, such as oxides and carbides, into a metallic matrix on a scale that is much finer than can be achieved by conventional powder metallurgy practices. [2]. It was quickly found that this solid-state powder processing route enabled intimately mixed, fine-scale composite powders to be produced from a wide range of elemental and master alloy starting powders. Now, the MA process is the one of the methods for the synthesis of polycrystalline compounds. In a typical MA process, the elemental powders are first put into a steel crucible with steel balls of different diameters then subjected to mechanical alloying (MA). The weight ratio of ball to powder is chosen carefully for each mill and powder charge combination, which is typically around 10:1 for commercial systems [3]. In order to avoid oxidation and contamination during MA processing, pre- and post-MA powder handling were conducted in the principal protective atmospheres such as argon or hydrogen gas.

After MA, the mixed powders were sintered using various sintering methods such as conventional sintering, hot pressing (HP) and spark plasma sintering (SPS).

4.2 Spark Plasma Sintering

Spark plasma sintering (SPS), which is also called the pressure-assisted pulse energizing process or the pulsed electric current sintering (PECS) process, is a rapid sintering technique that uses pressure-driven powder consolidation in which a pulsed DC current passes through a powder compressed in a graphite mold [4]. In 1933, the application of SPS was initiated by Taylor who incorporated the idea of resistance sintering during the hot pressing of cemented carbides [5], and Inoue proposed the concept of compacting metallic materials to a relatively high density by an electric discharge process in 1965 [6].

Figure 4-1 and 4-2 show a photograph of SPS system and a basic SPS System configuration, respectively. SPS system consist of punch electrodes incorporating a water cooler, a water-cooled vacuum chamber, a special DC pulse sintering power generator, temperature measuring and control units, and mechanical loading system. And it

can be seen that the powder put in the graphite die are uniaxial pressurized.

The figure 4-3 shows a SPS sintering mechanism. In the initial stage of sintering, a pulsed DC current generates a spark plasma at high localized temperatures in the gap between the powders, which causes heat. This heat forms the neck between the powder, and the powders are heated by Joule heating generated by an electric current [7].

SPS has several advantages such as fast heating rate, fast cooling rate, and very short holding time over conventional systems using hot press (HP) sintering, hot isostatic pressing (HIP), or atmospheric furnaces. These combined advantages make it possible to sinter powders to near full densification with little grain growth [8]. The microstructure and phases in the final sintered products are significantly influenced by SPS processing parameters. In general, SPS process depends upon sintering temperature, applied pressure, heating rate, holding time, and total sintering time and those parameters are essential for the optimization of consolidation conditions for each material type [9].

Figure 4-1. A photograph of SPS system.

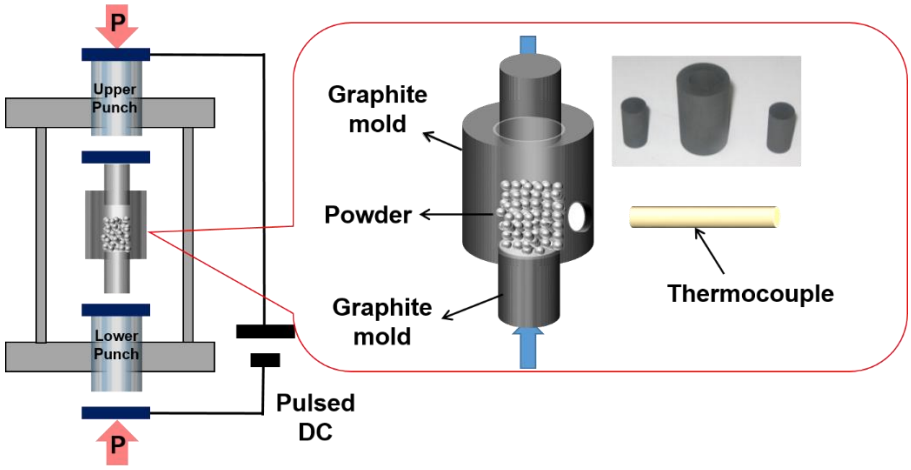

Figure 4-2. A basic SPS System configuration

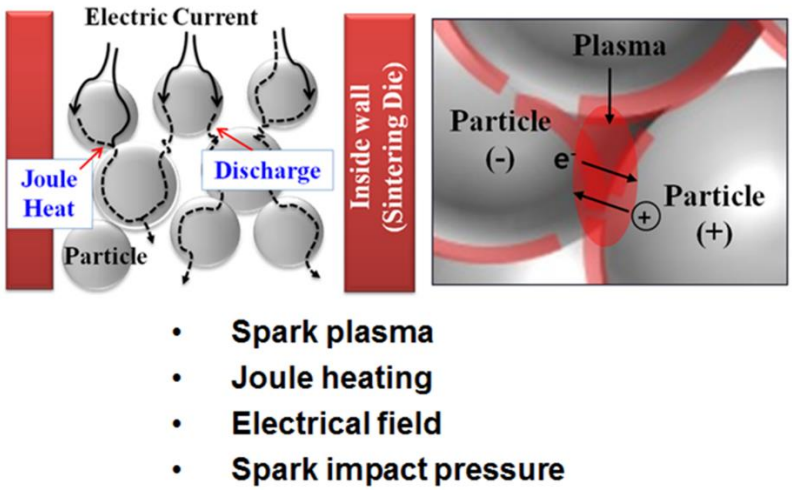

Figure 4-3. A mechanism of SPS.

4.3 X-ray Diffraction Analysis

X-ray diffraction (XRD) is a powerful nondestructive technique for characterizing crystalline materials such as structures, phases, preferred crystal orientations (texture), average grain size, crystallinity, strain, and crystal defects [10]. XRD is the elastic scattering of X-ray by atoms in a periodic lattice. The scattered X-rays interfere with each other and this interference can be observed in by using Bragg's law to determine characteristics of the crystalline materials [11]. The Bragg's law can be expressed by the following equation;

$$n\ \lambda = 2\ d \sin\theta \tag{4.1}$$

where n is an integer called the order of reflection, and λ is the wavelength of the X-ray, d is the characteristic spacing between the crystal planes, and θ is the angle between the incident beam and the normal to the reflecting lattice plane.

X-ray beam constructively interacts with the parallel plane of atoms when Bragg's law is satisfied as shown in Figure 4-4. XRD peaks are produced by constructive interference of a monochromatic beam of X-rays scattered at specific angles from each set of lattice planes in a crystalline material. The peak intensities are determined by the atomic positions within the lattice planes. Consequently, XRD

pattern gives a periodic atomic arrangement in the material [10]. In this study, The XRD phase analyses of powder and sintered samples were carried out using X-ray diffraction (XRD, D-8 Advanced, Bruker) with Cu K_{α} radiation.

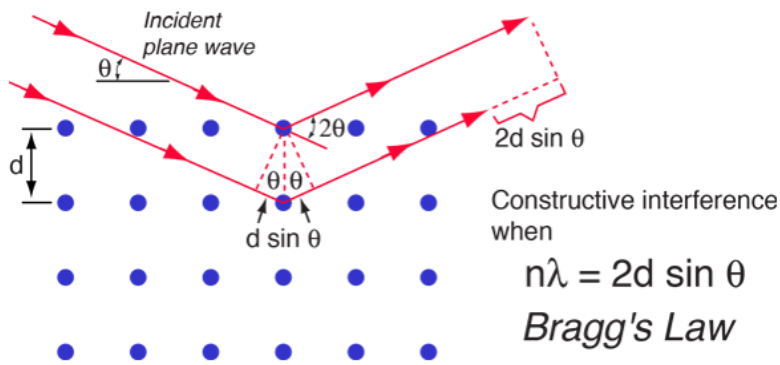

Figure 4-4. Bragg analysis for X-ray diffraction by crystal planes (http://hyperphysics.phy-astr.gsu.edu/hbase/quantum/bragg.html).

4.4 Electrical Conductivity and Seebeck Coefficient Measurement

4.4.1 Electrical Conductivity Measurement

A 4-point probe is a simple method to measure electrical conductivity of semiconductor samples. The 4-point probe method has been developed to minimize the contact resistance between the metal electrode and sample. The contact resistance depends on the resistance of samples. Electrical conductivity is obtained by passing a current through two outer probes and measuring the voltage through the inner probes. A constant electric current is streamed along the sample through Chromel or Alumel leg of the K-type thermocouple (TC) and resistive voltage (V_r) along the longitudinal direction of the bar-shaped sample is measured using the two of Pt probe. The voltage probe was positioned away from the current leads to allow a uniform flow of current through the voltage probe. The voltage ($\triangle V$) is generated by the TCs based on the Seebeck effect, which can be added to the voltage V_r during the measurement of electrical conductivity. Therefore, in order to minimize a generated $\triangle V$ by the Seebeck effect and to measure a more accurate V_r value, the repeated test with reversed high current flow rate [12]. The

electrical conductivity is calculated by the following equation;

$$\sigma = \frac{L}{A}R \tag{4.2}$$

where L is the distance between the two voltage proves, A is the cross sectional area of the sample, and R is the resistance of the sample. Figs. 4-5 show the commercial measurement equipment (Seepel Corp, Gunpo, Korea) used for the measurement of electrical conductivity and Seebeck coefficient.

4.4.2 Seebeck Coefficient Measurement

Seebeck coefficient (S) is defined as the ratio of an open-circuit potential difference to the temperature difference [13]. During the Seebeck coefficient measurement, it is difficult to measure the accurate voltage and real temperatures at voltage probes. So, the Seebeck should be measured between two points of a sample having temperature T1 and T2 at the respective points, under the condition that no current flows through the sample during measurement to prevent Peltier voltage. Then one end of the sample is kept at a fixed temperature while the other end is slowly heated. Using the gradient of voltage versus temperature, the S can be found for any given temperature [14]. The total Seebeck coefficient of sample and Pt is

obtained and can be expressed by following equation;

$$S_{total} = S_{sample} - S_{pt} \quad (4.3)$$

where S_{sample} and S_{Pt} are the Seebeck coefficient of sample and Pt, respectively. The sign of the Seebeck coefficient indicates the dominant charge carrier type. *p*−type materials have the positive Seebeck coefficient, whereas *n*−type materials have negative Seebeck coefficient. In this study, the commercial measurement equipment (Seepel Corp, Korea) shown in Figure 4−5 was used to measure Seebeck coefficients.

Figure 4-5. A photograph of the commercial measurement equipment (Seepel Corp, Korea)

4.5 Hall Effect Measurement

In 1879 E. H. Hall observed that when an electrical current passes through a conductor placed in a magnetic field, a potential proportional to the current and to the magnetic field is developed across the material in a direction perpendicular to both the current and to the magnetic field [15]. This effect is known as the Hall effect and is used to understand charge transport of TE materials. So, the Hall effect measurement is performed, and carrier concentration and Hall mobility of TE materials can be obtained by Hall effect measurement system in this study.

Figure 4-6 shows the mechanism for Hall effect. After current pass through the material, the magnetic field is applied to the conductor, and then the Hall voltage is produced in conductor. The Hall coefficient is calculated by following Eq. 4.4;

$$R_H = \frac{V_H w}{IB} \tag{4.4}$$

where R_H is the Hall coefficient, V_H is the Hall voltage, w is width of sample, I is the current applied, and B is the magnetic field applied, respectively. And he electrical conductivity and carrier concentration are obtained by using the Hall coefficient as represented by the following Eq. 4.5 and Eq. 4.6;

$$\sigma = \frac{V_H wd}{Il} \tag{4.5}$$

$$R_H = \frac{1}{ne} \tag{4.6}$$

where σ is the electrical conductivity, d is the thickness of a sample, l is the length of a sample, n is the carrier concentration, and e is the charge carrier. Hall mobility, u_H, is also calculated by Eq. 4.6.

$$\mu = \frac{\sigma}{ne} \tag{4.7}$$

Figure 4−7 shows the photograph of the Hall measurement system (HMS 3000, Ecopia, Korea) used to obtain the carrier concentration and Hall mobility of the sample.

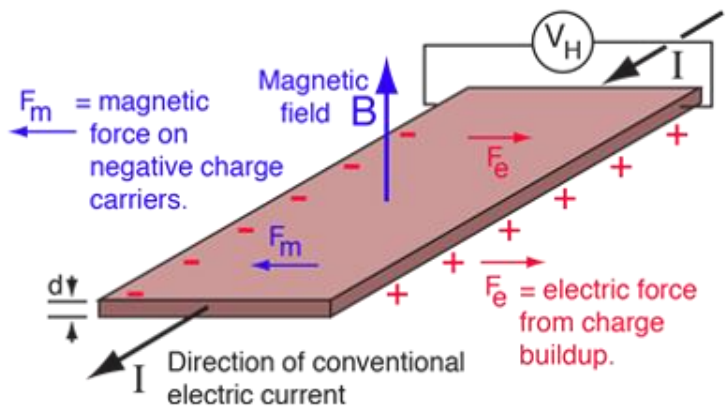

Figure 4-6. A schematic of mechanism of Hall effect.

(http://hyperphysics.phy-astr.gsu.edu/hbase/magnetic/Hall.html)

Figure 4-7. A photograph of Hall measurement system (HMS 3000, Ecopia, Korea).

4.6 Thermal Conductivity Measurement

In order to obtain a thermoelectric (TE) material with high ZT, it is necessary to have a low thermal conductivity. Thermal conductivity (k) can be defined as the rate at which heat is transferred by conduction through a unit cross-section area of a material, when a temperature gradient exits perpendicular to the area [16]. The Thermal conductivity is expressed by Eq. 4.7.

$$K_{tot} = \rho \cdot D \cdot C_P \quad (4.7)$$

where k_{tot}, ρ, D, and C_P are the total thermal conductivity, density, thermal diffusivity, and the specific heat of a sample. In this study, the ρ, D, and C_P values were measured using the Archimedes method, laser flash method (LFA) and, differential scanning calorimetry (DSC), respectively. The measurement principle and techniques are explained in the following sub-sections.

4.6.1 Thermal Diffusivity Measurement (Laser Flash Technique)

Thermal diffusivity is an important material thermophysical property. The most widely used method for measuring thermal

diffusivity is the laser flash technique [17]. The laser flash technique was introduced in 1961 by Parker et al. [18] Its concept is based on deriving thermal diffusivity from the thermal response of the rear side of an adiabatically insulated infinite plate whose front side was exposed to a short pulse of radiant energy, and the figure 4−8 shows the a schematic of laser flash method to measure thermal diffusivity. In this technique, a uniform heat pulse of short duration compared to the transient time through the sample is incident on the front face of a disc specimen, and the temperature rise on the rear face is recorded [19].

The Parker et al. showed that the point corresponding to 50% of the temperature rise to its maximum value, $t_{0.5}$ relating thermal diffusivity of the material to the square of the plate thickness, and the time needed for the rear temperature to reach 50% of its maximum. [18], and the thermal diffusivity is expressed as following Equation

$$D = \frac{0.1388L^2}{t_{0.5}} \tag{4.8}$$

where L is the thickness of a sample. Even though the laser flash technique is the most favored one for measuring thermal diffusivity.

Figure 4−8 shows the photograph of a laser flash analysis system

(LFA457, Netzsch). The samples are coated with graphite to improve the absorptivity. The dish shaped sample (12.7 mm in diameter and about 1~2mm thick) is placed in a vacuum furnace and isothermally heated at a uniform temperature. A short laser pulse irradiates one side of the sample and the temperature rise on the opposite sample face is measured by an IR detector.

4.6.2 Specific Heat Capacity

Heat capacity is a material-specific physical quantity, determined by the amount of heat supplied to specimen, divided by the resulting temperature increase. The specific heat capacity is related to a unit mass of the specimen. The unit of measure of specific heat capacity is kJ/kg·K.

Figure 4-10 shows a photograph of differential scanning calorimetry (DSC 204F1 Phoenix, Netzsch). Differential scanning calorimetry (DSC) is a thermoanalytic technique that looks at how a material's heat capacity (Cp) is changed by temperature [20]. Generally, the Cp is measured by differential scanning calorimetry (DSC). Although the Cp can be measured using the LFA, it is not as accurate and reliable as DSC.

In an ideal DSC measurement, no heat flow would occur unless a sample with heat capacity was heated, and the empty pan baseline would be a straight line at 0 mW. When a sample is heated in ideal DSC, the displacement will be occurred from the zero line, which can be expressed as Eq. 4.9 [21];

$$\frac{dQ}{dt} = C_P \times \beta \times W \quad (4.9)$$

where dQ/dt is heat flow, β is heating rate and W is the sample mass. In real DSC measurement, however, there is a heat flow offset when there is no sample present. Therefore, in order to obtain accuracy Cp of the sample, it has been necessary to subtract an empty pan baseline run under identical conditions, before determining Cp from Eq. 4.9 [21] .

According to ASTM standard E1269, which requires three scans: a baseline scan, a scan using a sapphire standard, and the sample scan, the Cp were measured by DSC, and each samples were measured three times under same conditions.

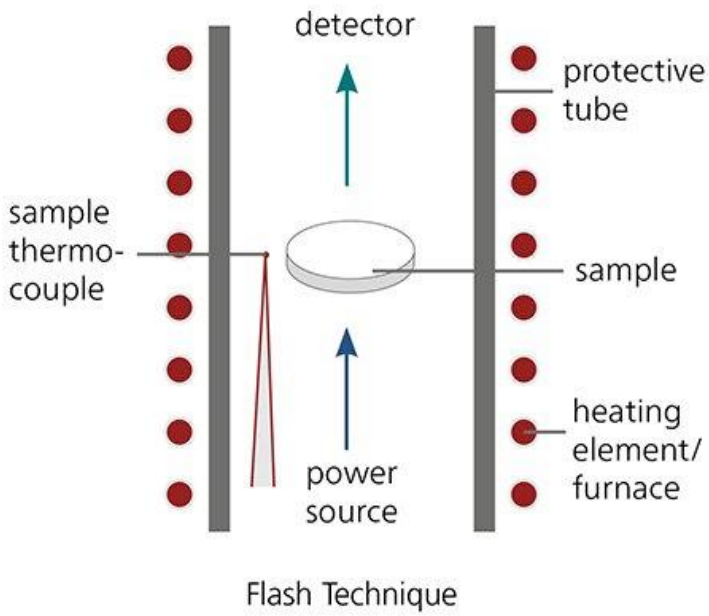

Figure 4-8. Laser flash method principles.

Figure 4-9. A photograph of laser flash analysis system (LFA 457, Netzsch).

Figure 4-10. A photograph of differential scanning calorimetry (DSC 204F1 Phoenix, Netzsch)

4.7 References

[1] A. Zhou, Methods of MAX−phase synthesis and densification–II, Advances in science and technology of Mn+1AXn phases, Elsevier (2012) 21.

[2] C. Suryanarayana, E. Ivanov, Mechanochemical synthesis of nanocrystalline metal powders, Advances in powder metallurgy, Elsevier (2013) 42.

[3] P. Gilman, J.J.A.r.o.m.s. Benjamin, Mechanical alloying, 13 (1983) 279.

[4] J.−L. Huang, P. Nayak, Strengthening alumina ceramic matrix nanocomposites using spark plasma sintering, Advances in ceramic matrix composites, Elsevier (2014) 218.

[5] G.F. Taylor, Apparatus for making hard metal compositions, Google Patents, (1933).

[6] I. Kiyoshi, Electric discharge heat treatment of metals in electrolytes, Google Patents, (1965).

[7] M. Suárez, A. Fernández, J. Menéndez, R. Torrecillas, H. Kessel, J. Hennicke, R. Kirchner, T.J.S.A. Kessel, Challenges and opportunities for spark plasma sintering: a key technology for a new generation of materials, 13 (2013) 319.

[8] T. Hungria, J. Galy, A.J.A.E.M. Castro, Spark plasma sintering as a useful technique to the nanostructuration of piezo-ferroelectric

materials, 11 (2009) 615.

[9] N. Ghosh, S. Harimkar, Consolidation and synthesis of MAX phases by Spark Plasma Sintering (SPS): a review, Advances in Science and Technology of Mn+ 1AXn Phases, Elsevier (2012) 80.

[10] R. Kohli, Methods for monitoring and measuring cleanliness of surfaces, Developments in Surface Contamination and Cleaning, Elsevier (2012) 107.

[11] S. Rajeshkumar, L. Bharath, R. Geetha, Broad spectrum antibacterial silver nanoparticle green synthesis: Characterization, and mechanism of action, Green Synthesis, Characterization and Applications of Nanoparticles, Elsevier (2019) 429.

[12] J. Pacio, M. Daubner, F. Fellmoser, W. Hering, W. Jäger, R. Stieglitz, T. Wetzel, Construction of experimental liquid–metal facilities, Thermal Hydraulics Aspects of Liquid Metal Cooled Nuclear Reactors, Elsevier (2019) 107.

[13] G.S. Nolas, J. Sharp, J. Goldsmid, Thermoelectrics: basic principles and new materials developments, Springer Science & Business Media (2013).

[14] A. Mishra, S. Bhattacharjee, S.J.M. Anwar, Simple apparatus to measure Seebeck coefficient up to 900 K, 68 (2015) 295.

[15] E.H.J.A.J.o.M. Hall, On a new action of the magnet on electric currents, 2 (1879) 287.

[16] A. Palacios, L. Cong, M. Navarro, Y. Ding, C.J.R. Barreneche, S.E. Reviews, Thermal conductivity measurement techniques for characterizing thermal energy storage materials–A review, 108 (2019) 32.

[17] S.F. Corbin, D.M.J.C.o.M. Turriff, Thermal diffusivity by the laser flash technique, (2002) 1.

[18] W. Parker, R. Jenkins, C. Butler, G.J.J.o.a.p. Abbott, Flash method of determining thermal diffusivity, heat capacity, and thermal conductivity, 32 (1961) 1679.

[19] I. Abdulagatov, Z. Abdulagatova, S.N. Kallaev, A. Bakmaev, P.G.J.I.J.o.T. Ranjith, Thermal–diffusivity and heat–capacity measurements of sandstone at high temperatures using laser flash and DSC methods, 36 (2015) 658.

[20] V. Nikolić, S. Ilić–Stojanović, S. Petrović, A. Tačić, L. Nikolić, Administration routes for nano drugs and characterization of nano drug loading, Characterization and Biology of Nanomaterials for Drug Delivery, Elsevier (2019) 587.

[21] R.B.J.T.I. Cassel, New Castle, DE, How Tzero™ Technology Improves DSC Performance Part III: The Measurement of Specific Heat Capacity, (2001).

Chapter 5. The effects of Sintering Pressure on the Electrical Transport and Thermoelectric Properties of the Polycrystalline SnSe

5.1 Introduction

Due to growing interest in new energy systems to solve the global energy crisis, the world's demand for new, clean and renewable energy resources has been increasing [1, 2]. Thermoelectric (TE) materials, which can convert waste heat into electrical energy, has been attracting attention as an alternative eco-friendly energy material [3, 4]. The performance of a TE material is represented by the figure of merit (ZT), $ZT = (S^2\sigma/k)T$, where S, σ, k, and T are Seebeck coefficient, electrical conductivity, thermal conductivity, and absolute temperature, respectively. [5]. Over the past several decades, many TE materials, including alloy semiconductors such as Bi_2Te_3, PbTe, and SiGe, have been integrated into conventional power generation and refrigeration systems [6-11].

Recently, SnSe, which is composed of nontoxic and abundant elements, has been considered as a promising candidate for a TE material for practical application. The potential of SnSe has attracted a great deal of attention since high ZT value of ~2.6 at 923 K was

reported in single crystal SnSe by Zhao et al [12]. Zhao et al. [13] also reported the enhanced TE properties of Na-doped single crystal SnSe In the case of single crystal SnSe, however, the mechanical properties are poor, and the production cost is high [14]. SnSe should be synthesized in a polycrystalline form for practical application. And so, efforts were made to make polycrystalline SnSe which has TE performance similar to that of single crystal SnSe. It was reported that thermal conductivity of polycrystalline SnSe is similar to that of single crystal SnSe, but its electrical conductivity is remarkably low compared to that of single crystal [14].

Various studies have been carried out to improve the electrical conductivity of polycrystalline SnSe by doping [15-24]. Chen et al. and Zhang et al. reported the TE performance of Ag doped polycrystalline SnSe [16, 17]. According to Chen et al. [16], Ag is not an effective doping element, while Zhang et al. [17] reported that TE performance of SnSe can be improved by Ag doping and a ZT of ~1.3 was obtained in the Ag-doped SnSe. Wei et al. [18] investigated TE performance of polycrystalline SnSe doped with three alkali metals (Li, Na, and K) and reported a ZT of ~0.8 in Na doped SnSe. Singh et al. [19] reported a ZT of up to ~ 0.7 in Cu doped SnSe which

was attributed to the presence of Cu2Se second phase associated with intrinsic nanostructure formation of SnSe. Li et al [20] reported a ZT of up to ~0.96 in Zn doped SnSe, which was ~40% higher than that of pure SnSe. Ge et al. [21] reported that Na and K co-doping can lead to the increase of Seebeck coefficient and a decrease of lattice thermal conductivity in polycrystalline SnSe, which resulted in a ZT of ~1.2 in 1% (Na, K) co-doped SnSe. Chandra et al. [22] reported a ZT of ~0.21 at 719 K for 6% Bi-doped SnSe nanosheets, which is higher than that of n-type SnSe nanosheets. They [23] also reported a ZT of ~2.1 at 873 K in 3 % Ge-doped SnSe nanoplates synthesized by a simple hydrothermal route followed by spark plasma sintering (SPS)

The TE performances of polycrystalline SnSe which was improved by doping, however, are still low compared to that of single crystal SnSe. Further improvement of TE performance of polycrystalline SnSe is needed for practical application. SnSe has anisotropic structure, and its electrical/thermal properties strongly depend on the crystal orientation [12]. Therefore, if the grains of polycrystalline SnSe can be oriented along the direction with high electrical conductivity through the control of texture, the electrical

properties can be improved. There are a few reports on the TE properties of textured polycrystalline SnSe [25–28]. Popuri et al. [25] reported anisotropic TE properties of polycrystalline SnSe when they were measured along the direction perpendicular and parallel to the pressure applied during hot pressing. Fu et al. [26] reported a ZT of ~0.92 at 873K in highly textured polycrystalline SnSe samples prepared by zone melting. But, zone melting is a relatively long and expensive process and is a difficult process to control the degree of texture. Feng et al. [28] reported that different degrees of texture of the polycrystalline SnSe can be obtained by SPS at different sintering temperatures; a ZT of ~0.81 was obtained at 773K in the polycrystalline SnSe which was sintered at 623 K. However, measurement of the TE properties at a temperature higher than the sintering temperature can lead to changes of the microstructure (e.g. grain size, density, etc.) and loss of some element(s), which can affect the TE property [29, 30]. Li et al. [30] reported that the degree of texture of polycrystalline SnSe is not affected by sintering temperature. Therefore, it is difficult to explain the change of TE property using the change of the degree of texture only, when factors other than the degree of texture can affect the TE properties.

One way to control the degree of texture of polycrystalline SnSe is to change the sintering pressure. In the case of Bi_2Te_3, $CoSb_3$, and BiCuSeO, which have anisotropic TE properties, the TE performance can be improved by controlling the degree of texture through sintering pressure. [31−34]. The effect of texture on the TE properties of SnSe (which also has anisotropic TE properties) with all parameters other than the degree of texture kept constant, has not been reported. In this study, the degree of texture of polycrystalline SnSe was controlled by the pressure applied during SPS, and the effects of sintering pressure on electrical transport and TE properties of the polycrystalline SnSe were investigated.

5.2 Experimental Procedure

5.2.1 Synthesis of Polycrystalline SnSe Powder

Figure 5-1 shows the experimental procedure. High purity Sn (4N, Sigma Aldrich) and Se (99.99%, Sigma Aldrich) powders were used as the starting materials. Sn and Se were weighed based on the stoichiometry of SnSe and placed in a steel crucible at a ratio of 5:1 with steel balls. Using the prepared mixture, polycrystalline SnSe powder was then synthesized by mechanical alloying for 4 h in Ar atmosphere.

5.2.2 Fabrication of Polycrystalline Bulk SnSe

Approximately 4 grams of the synthesized SnSe powder was placed in a 12.5 mm-diameter graphite crucible die and sintered in vacuum (~2 x 10^{-3} Torr) at 850 K for 5 min under various uniaxial pressure of 0, 30, 60, 90 and 120MPa using SPS.

5.2.3 Characterization

Sintered SnSe samples were carried out using X-ray diffractio n (XRD, D-8 Advanced, Bruker). The microstructures of the sa mples were observed using a field emission scanning electron mi

croscope (FE-SEM, SU-70, JEOL). The size distribution of SnSe particles were observed using a particle size analyzer (PSA, LS 13 320, Beckman Coulter). The disk-shaped sintered bodies were cut into bar shapes of 1.5 x 1.5 x 7 mm^3. The electric conductivity and Seebeck coefficient were measured from 300K to 823K using a commercial measurement equipment (Seepel Corp). Carrier concentrations of the SnSe samples at room temperature were obtained using a Hall measurement system (HMS 3000, Ecopia). The total thermal conductivity (k_{tot}) can be expressed as the sum of electronic thermal conductivity (k_e) and lattice thermal conductivity (k_{latt}). The k_{tot} was calculated by multiplying the specific heat (C_p), thermal diffusivity (D), and density (ρ). The C_p values which were measured from room temperature to 823k using differential scanning calorimetry (DSC, DSC-404C, Netzsch) were used for the calculation of k_{tot}. The samples were put in an alumina crucible in Ar atmosphere, and the DSC curve was recorded with a heating rate of 10 K/min. The D and ρ values were measured using the laser flash method (LFA457, Netzsch) and the Archimedes method, respectively. The k_e was obtained using the Wiedemann-Franz law, $k_e = L\sigma T$, where L, σ and T are Lorenz number, electrical conductivity and absolute temperature, respectively. The Lorenz number which was calculated from the Se

ebeck coefficients by fitting to the reduced chemical potential in prior reports, was used to obtain k_e. [35, 36]. The k_{latt} was obtai ned by subtracting the k_e from the k_{tot}. The TE properties of all the samples were measured perpendicular to the direction of the pressure applied during the SPS.

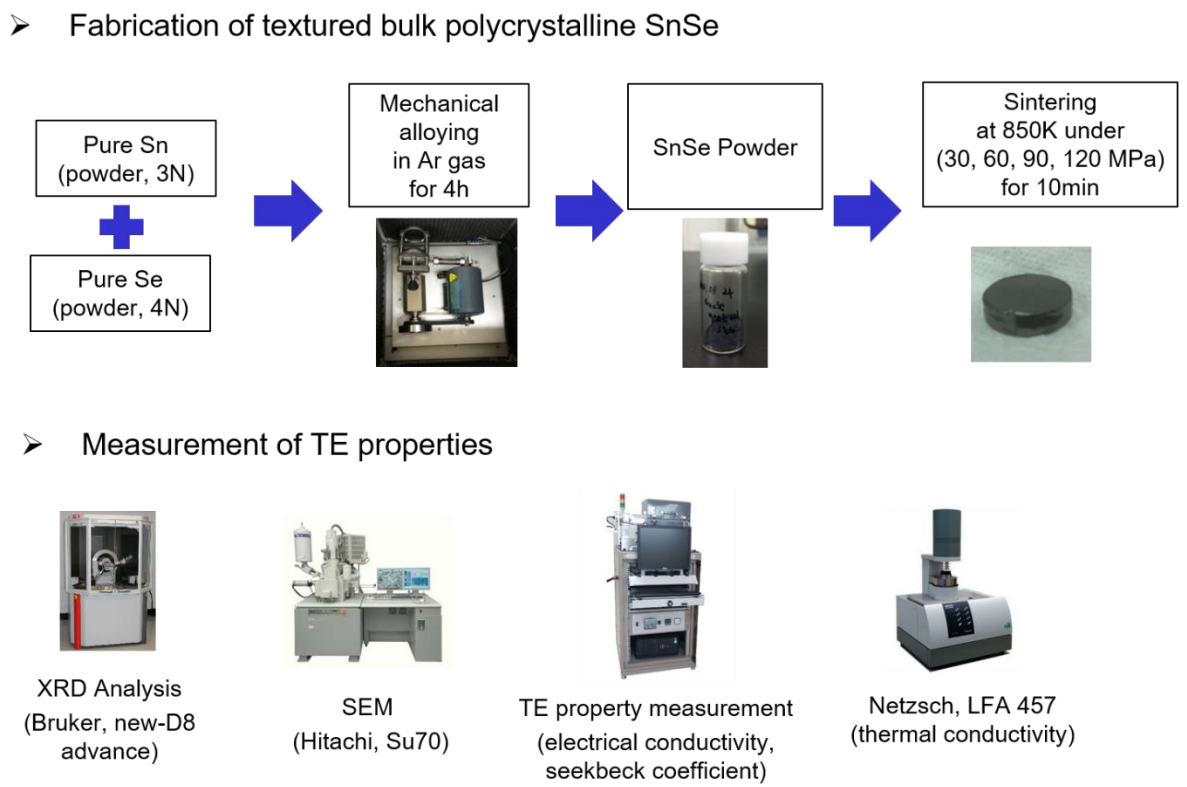

Figure 5-1. Experimental procedure.

5.3. Results and Discussion

5.3.1 Phase Analysis of Textured Bulk SnSe

Figure 5-2 shows the XRD pattern and the SEM image of the SnSe powder prepared using mechanical alloying. The peaks with (hkl)'s are from orthorhombic SnSe (PDF #48-1224), and peaks from secondary phase(s) are not observed in the pattern. The average size of SnSe particles observed by PSA was approximately 8.2 um and the result is shown in Figure 5-3.

Figure 5-4 shows XRD patterns of the polycrystalline SnSe sintered with different sintering pressures. XRD patterns were obtained from planes perpendicular to the direction of the applied pressure. All the diffraction peaks in Figure 2 come from the orthorhombic SnSe (PDF #48-1224), and no peaks from any secondary phase(s) are observed. As the sintering pressure is increased, the relative intensity ratio I(111)/I(400) is decreased, which means that the degree of (100) out-of-plane orientation is increased.

The degree of texture of the samples can be described by the Lotgering factor (F) [37]. The F value is defined using the following equation;

$$F = \frac{(P - P_0)}{(1 - P_0)} \quad (5.1)$$

Where $P = \sum I(l\ 0\ 0)/\sum I\ (h\ k\ l)$ for the textured sample, and P_0 is P for randomly oriented sample. In this study, P_0 was calculated from the data of the orthorhombic SnSe (PDF #48-1224). The results are shown in table 5-1. The calculated F values of the SnSe, which were sintered with different pressures of 30, 60, 90 and 120MPa, were 0.11, 0.16, 0.25 and 0.43, respectively.

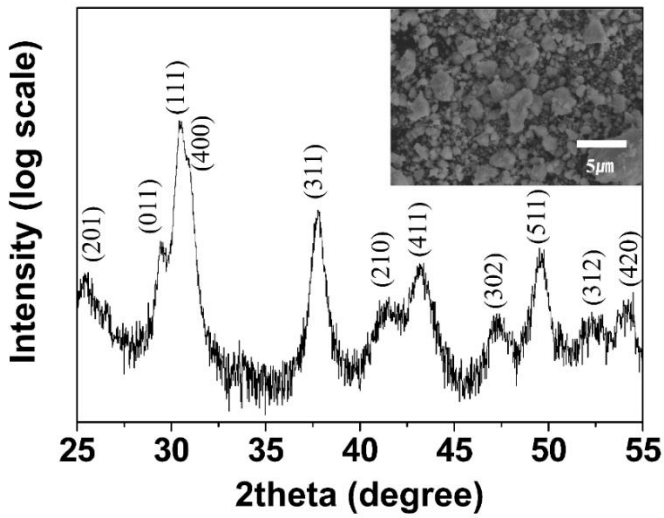

Figure 5-2. X-ray diffraction (XRD) pattern and the SEM image of the SnSe powder prepared using mechanical alloying.

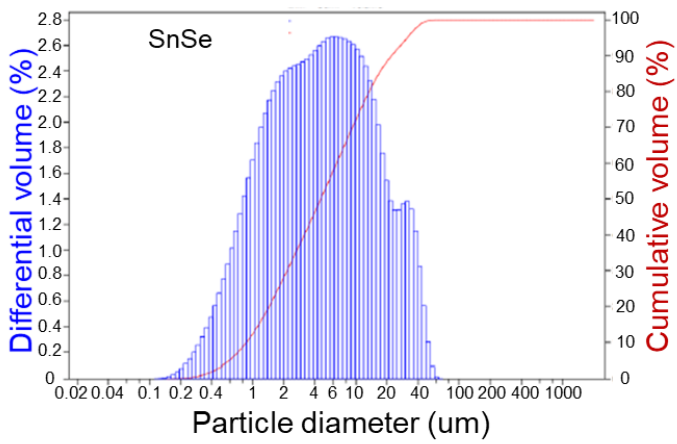

Figure 5-3. Particle size distributions of SnSe powder using analyzer (PSA).

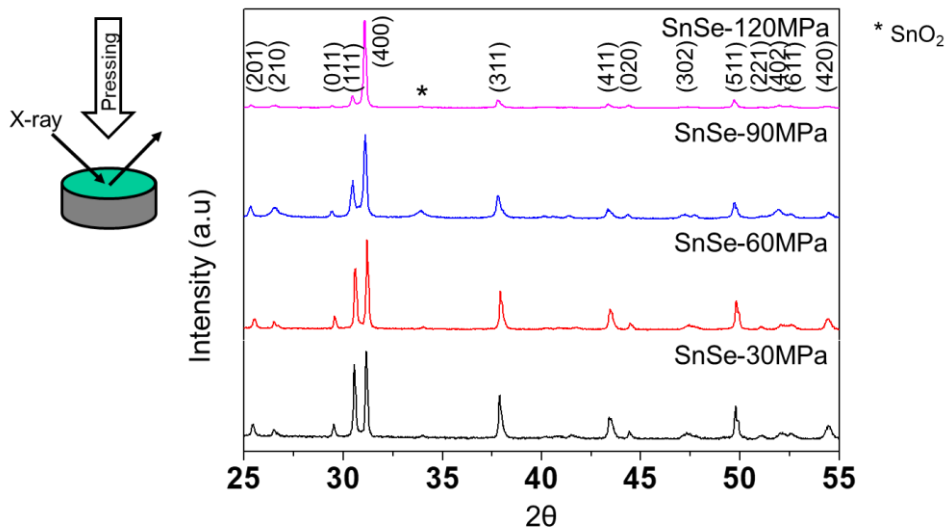

Figure 5-4. X-ray diffraction (XRD) pattern and the SEM image of the SnSe powder prepared using mechanical alloying.

Table 5-1. Lotgering factor (F) and charge transport properties of the polycrystalline SnSe sintered with different sintering pressures (30, 60, 90 and 120MPa). The carrier concentration (n), carrier mobility (μ), and electrical conductivity were measured at room temperature.

Sintering pressure (MPa)	Lotgering factor (F)	Carrier concentration [n, cm^{-3}]	Carrier mobility [μ,$cm^2/V \cdot s$]	Conductivity [σ, S/cm]
30	0.11	3.04×10^{18}	7.5	3.89
60	0.16	3.16×10^{18}	10.46	5.59
90	0.25	2.99×10^{18}	12.27	6.19
120	0.43	2.89×10^{18}	21.21	10.35

5.3.2 Microstructure of Textured Bulk SnSe

Figure 5-5 (a) ~ (d) show the FE-SEM micrographs taken from the fracture surface of the polycrystalline SnSe samples sintered with different pressures. All the sintered samples have dense microstructure and plate-like grains. As the sintering pressure is increased, plate-like grains are aligned along the direction perpendicular to the pressure applied during sintering. A much higher degree of texture is observed in the SnSe sintered with 120MPa than that sintered with 30MPa. From the results of XRD and FE-SEM, the surface of the plate-like grain can be (100) plane. Feng et al. [28] reported that the surface of the plate-like SnSe particle is (100) plane and the plane of preferred orientation changed from (111) to (100) when SPS pressure was increased, which is consistent with the results of this study. An electron probe micro-analysis (EPMA) was used to quantitatively determine the composition of all the sintered samples. The atomic ratio of Sn and Se for all the sintered samples was close to 50 ($\pm$0.1) : 50 ($\pm$0.1), which means that there was no change of composition during sintering. The grains sizes of all the samples observed by FE-SEM were similar. Therefore, the change of TE properties can be explained by the single effect of texture generated by the pressure applied during SPS, without the effect of the change of composition and grain size.

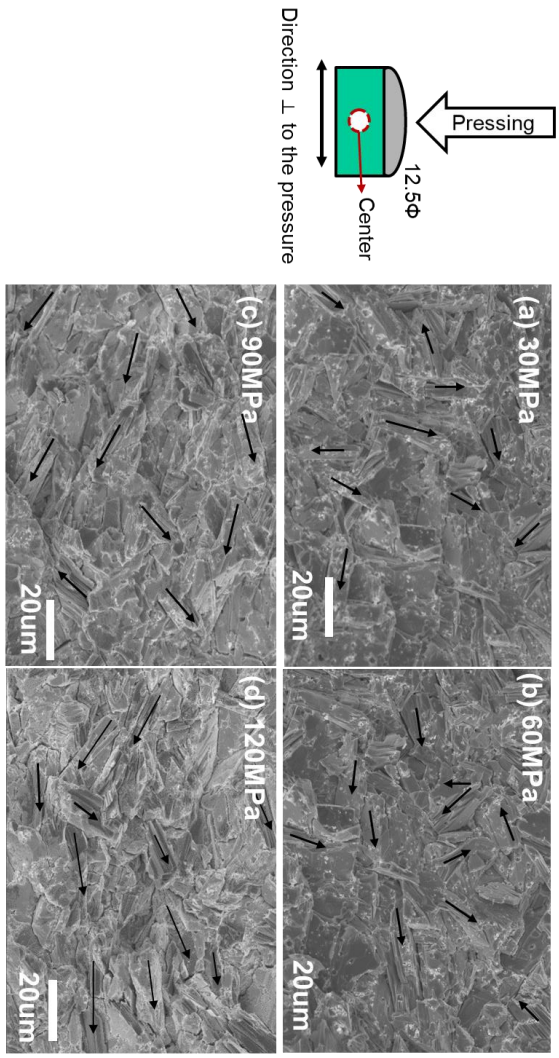

Figure 5-5. FE-SEM micrographs taken from the fracture surface of the polycrystalline SnSe sintered with different sintering pressures (a) 30, (b) 60, (c) 90 and (d) 120MPa.

5.3.3 Thermoelectric (TE) property of Textured Bulk SnSe

Figure 5-6 (a) shows the temperature-dependent electrical conductivity (σ) of the polycrystalline SnSe sintered with different sintering pressures. The way electrical conductivity changes with temperature does not change when different pressure was applied during SPS. The electrical conductivities were increased with temperature up to ~450K, then decreased from ~450K to ~650K, and then increased again. The change of electric conductivity with the temperature observed in this study is in agreement with those of the previous reports [28, 38, 39]. Sassi et al. [38] reported that the reduction of the electrical conductivity can occur when Sn is melted at a temperature around 505K. Fu et al. [39] reported that the increase in electrical conductivity at temperatures above ~650K can be attributed to the thermal activation of minority carriers and the phase transition of the SnSe from Pnma to Cmcm.

The electrical conductivity is increased with sintering pressure. In general, electrical conductivity is known to be influenced by carrier concentration (n) and carrier mobility (μ). To investigate the effects of pressure on the charge transport properties, the carrier concentration and mobility of SnSe sintered at different pressures

were measured at room temperature, and the results are shown in Table 5-1. As the pressure is increased, the carrier concentrations of the SnSe, which are in the range of 2.8 ~ 3.0 x 10^{18} cm^{-3}, do not show any significant change. Yan et al. [40] and Ghosh et al. [41] reported that the bandgap of SnSe is reduced by high pressures (4 ~ 10GPa) and the intrinsic carrier concentration is increased by the reduced bandgap. In this study, however, there was no significant change in the carrier concentration when the pressure applied during SPS was changed (30~120MPa). It is difficult to explain the increase of the electric conductivities observed in this study using the change of the band gap which was used to explain the change of electrical conductivities in previous studies [23,24]. The improvement of the electric conductivity with increasing pressure can come from the increase of the carrier mobility. The enhancement of degree of texture was confirmed through XRD and FE-SEM (fig 5-4 and 5), which can lead to the increased hole carrier mobility, which is consistent with the results of Fu et al. [39].

Figure 5-6 (b) shows the temperature-dependent Seebeck coefficients (S) of the polycrystalline SnSe sintered with different sintering pressures. S values can be determined by Pisarenko relationship which is given below [42].

$$S = \frac{8\pi^2 k_B^2 T}{3q\hbar^2} m_d^* \left(\frac{\pi}{3n}\right)^{2/3} \quad (5.2)$$

where q, k_B, h, m_d^*, and n are the charge of carrier, the Boltzmann constant, the Planck constant, and the density of state (DOS) effective mass, respectively.

The measured Seebeck coefficients are positive, which means that the samples are p-type semiconductors. For all the samples, up to 550K, the S values are increased, and then are slightly decreased, followed by a sharp decrease from 750K. The decrease in the Seebeck coefficient in the temperature range of 550~673K can be the result of the bipolar conduction by the excitation of the minor carrier [28], and the sharp decrease of the Seebeck coefficient can be caused by the increase of the hole concentration by the phase transition of SnSe from Pnma to Cmcm [26, 43]. The S values of all the samples at room temperature are not significantly changed by sintering pressure. According to the measured carrier concentrations (Table 5-1), the carrier concentration at room temperature did not change with the increase of sintering pressure, indicating that the Seebeck coefficient is not affected by the degree of texture.

Figure 5-7 shows the temperature-dependent power factor ($PF=S^2\sigma$) of the polycrystalline SnSe sintered at 850K with different sintering pressures (30, 60, 90 and 120MPa). The SnSe

sintered at 120MPa has a PF of ~3.9 x10^{-4} W/m· K^2 at 823K, due to the improved electrical conductivity, which means that the use of sintering pressure can enhance the electrical transport of polycrystalline SnSe.

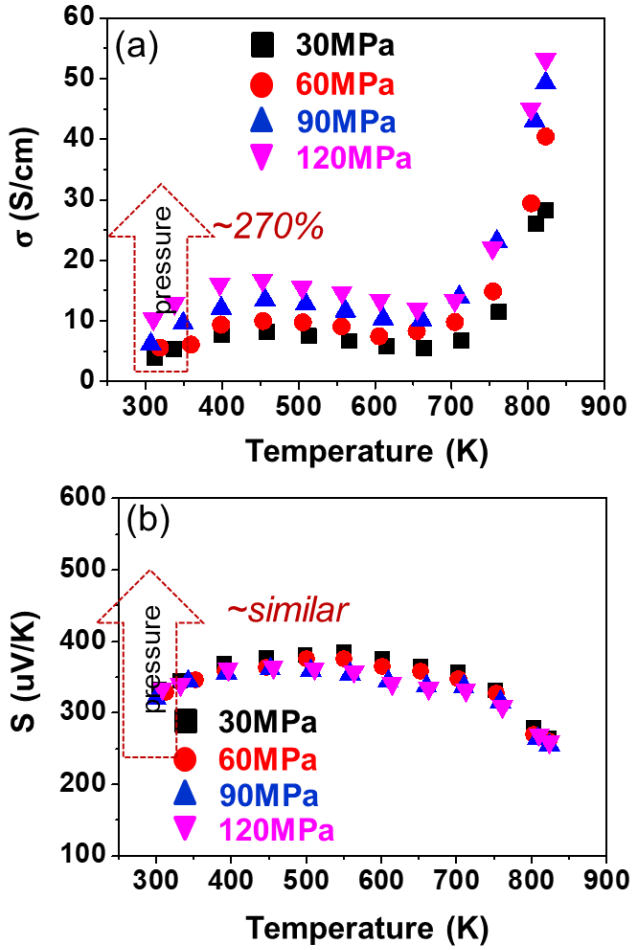

Figure 5-6. The temperature-dependent (a) electrical conductivity (σ) and (b) Seebeck coefficient (S) of the poly-crystalline SnSe sintered with different sintering pressures.

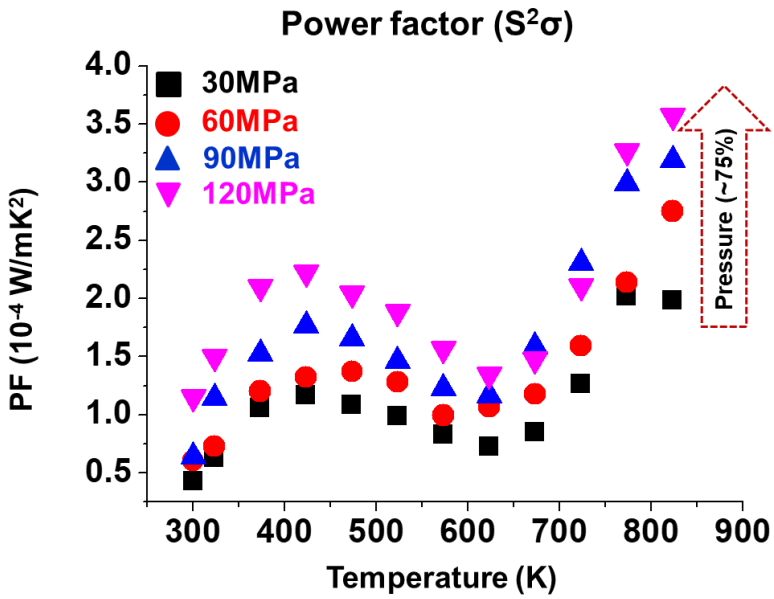

Figure 5-7. The temperature-dependent power factor ($PF=S^2\sigma$) of the polycrystalline SnSe sintered with different sintering pressures.

5.3.4 Thermal Conductivity and ZT of Textured Bulk SnSe

Figure 5-8 (a) shows the temperature-dependent total thermal conductivities (k_{tot}) of the SnSe sintered at 850K with different sintering pressures. k_{tot} is decreased with the increase of temperature from room temperature to 773K, and then is increased at temperatures higher than ~773K due to the phase transition of the SnSe from Pnma to Cmcm [18, 25]. As the sintering pressure is increased, the k_{tot} increased, which can be explained in terms of the changes in electrical/lattice thermal conductivity. k_{tot} is a sum of k_e and k_{latt}. k_e was calculated using the Wiedemann-Franz relation, $k_e = L\sigma T$, where L, σ and T are Lorenz number, electrical conductivity and absolute temperature, respectively. k_{latt} can be obtained by subtracting k_e from k_{tot}.

Figure 5-8 (b) shows the temperature-dependent electronic thermal conductivity (k_e) and the lattice thermal conductivity (k_{latt}) of the SnSe sintered with different pressures. In all the samples, the change in k_{latt} with increasing temperature is similar to the change in k_{tot}. k_{latt} is decreased with the increase in temperature up to ~ 773K and then is increased at temperatures over 773K. Leng et al. [44] and Gao et al. [45] reported that the decreasing of k_{latt} up to ~ 773K

is due to the increase in phonon scattering with increasing temperature, and the increase of k_{latt} over 773K is related to the phase transition from Pnma to Cmcm. When sintering pressure is increased from 30 to 120MPa, the change of k_e is not noticeable, but the change of k_{latt} is significant, indicating that the change of k_{tot} is mainly determined by the change of k_{latt}. The grain boundary scattering was reported to have a significant influence on lattice thermal conductivity [46, 47], which can be responsible for the change of k_{latt} observed in this study. As the sintering pressure is increased, the enhancement of degree of texture along the direction perpendicular to the applied pressure is observed through XRD and FE-SEM (figure 2 and 3), which can lead to the decrease in the phonon scattering at the grain boundary, which results in the increase of lattice thermal conductivity.

Figure 5-9 shows the temperature-dependent figure of merits (ZT) of the polycrystalline SnSe obtained from the electrical conductivity, Seebeck coefficient, and thermal conductivity. The highest ZT value obtained in this study was from the SnSe sample sintered at 60MPa, which was about 0.7 at 823K. To investigate the reproducibility of ZT values of SnSe sintered at 60MPa, ZT values of three SnSe samples sintered at 60 MPa were compared, and the

results are shown in figure 5-10. The ZT values of all three samples show no significant difference.

The results of this study shows that as the pressure applied during sintering is increased, the electrical conductivity of polycrystalline SnSe can be effectively increased by out-of-plane texturing, which gives a positive effect on the ZT value. The thermal conductivity, however, was also increased by the reduced phonon scattering at the grain boundary, which gives a negative effect on the ZT value. Therefore, large improvement of ZT was obtained in the polycrystalline SnSe sintered with 60MPa at temperatures > ~700K which has high power factor and small change of thermal conductivity compared to the samples sintered with 30MPa. This study shows that different amount of out-of-texturing can be obtained by the application of different pressures, which can be used to control the TE performance.

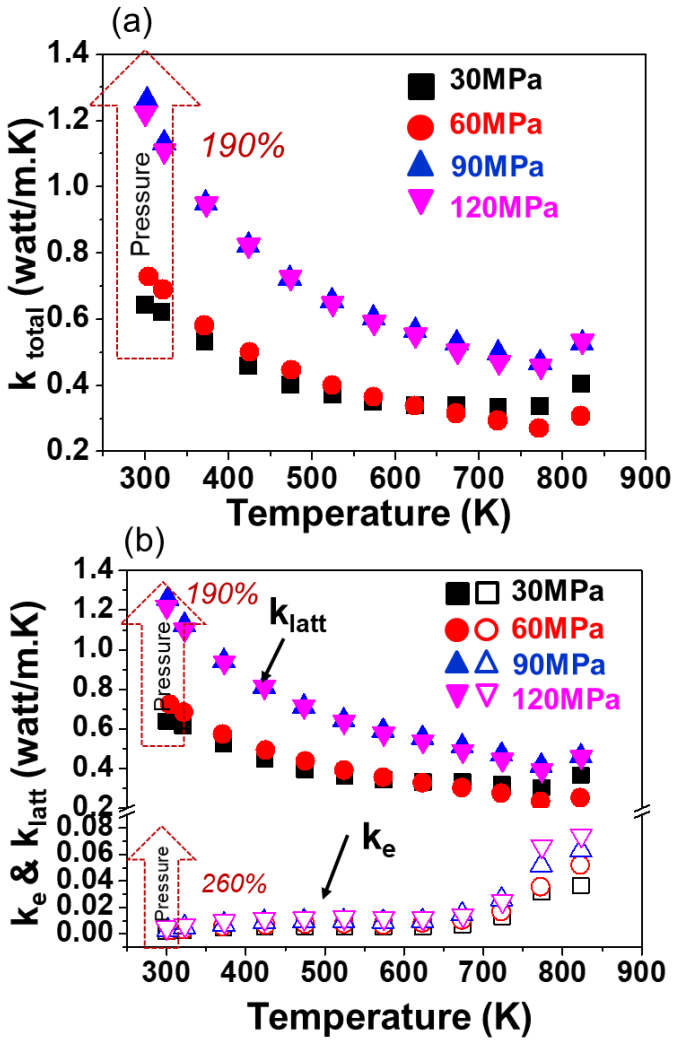

Figure 5-8. The temperature-dependent (a) total thermal conductivity (k_{tot}), (b) electronic thermal conductivity (k_e) and the lattice thermal conductivity (k_L) of the polycrystalline SnSe sintered with different sintering pressures. (filled shapes – the lattice thermal conductivity; hollow shapes – the electronic thermal conductivity).

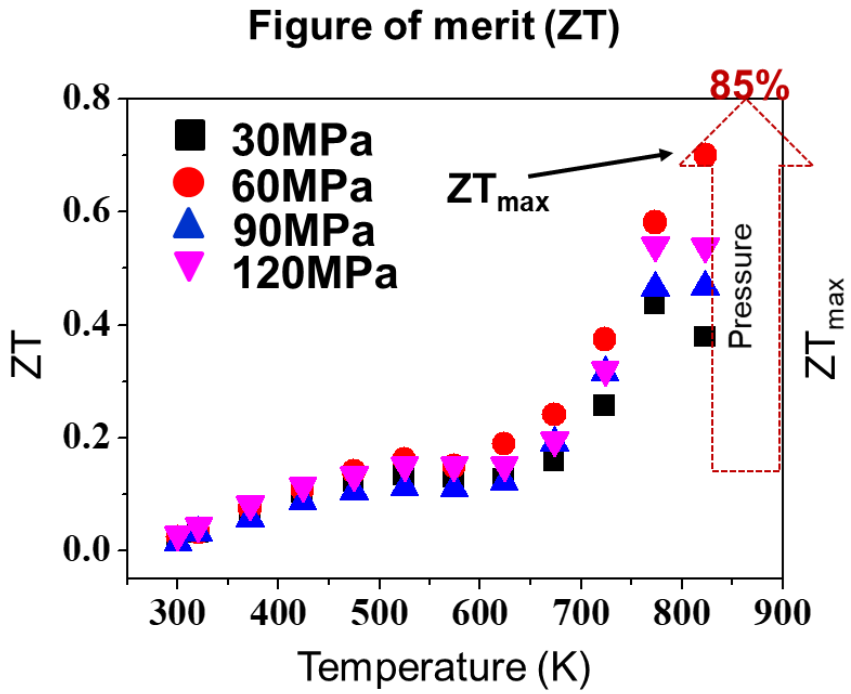

Figure 5-9. The temperature-dependent figure of merits (ZT) of the polycrystalline SnSe sintered with different sintering pressures.

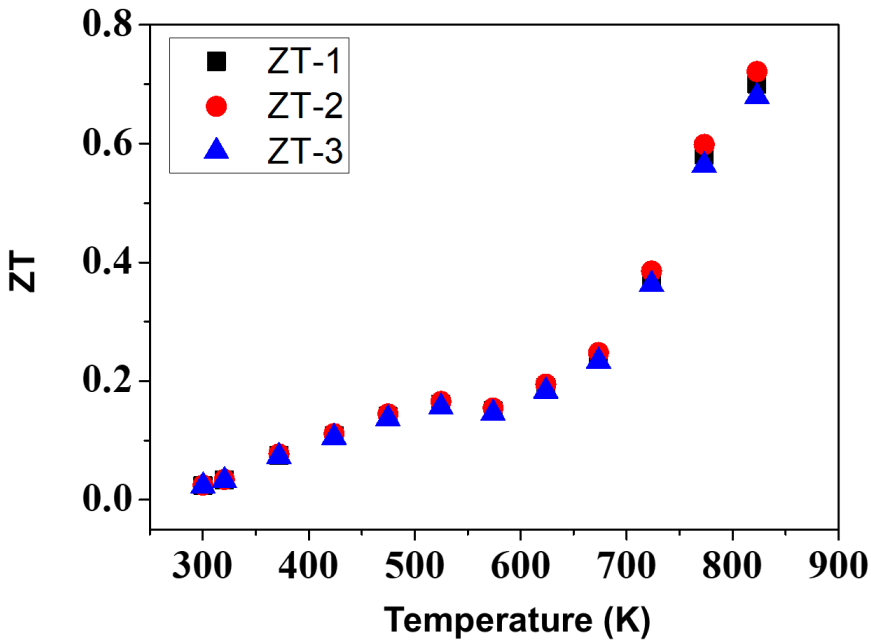

Figure 5-10. The ZT values of three SnSe samples spark-plasma-sintered at 60MPa.

5.4. Summary

This study investigated the effects of the pressure applied during spark plasma sintering (SPS) on the electrical charge transport and the thermoelectric (TE) properties of the polycrystalline SnSe. Degree of texture was enhanced with increasing sintering pressure from 30 to 120MPa during SPS of polycrystalline SnSe, which lead to the increase of carrier mobility, thereby increasing the electrical conductivity. When the pressure was increased, the total thermal conductivity was significantly increased by the increase of the lattice thermal conductivity which resulted from the decrease of the phonon scattering at the grain boundary. A ZT of ~0.7 was obtained at 823K from the polycrystalline SnSe, which was sintered with a pressure of 60MPa, which can be attributed to large increase in electrical conductivity with very small increase of the thermal conductivity. This study shows that the TE properties of the polycrystalline SnSe can be controlled by the degree of texture which can be obtained by the pressure applied during SPS.

5.5. References

[1] B.J. De Vries, D.P. Van Vuuren, M.M. Hoogwijk, Renewable energy sources: Their global potential for the first-half of the 21st century at a global level: An integrated approach, Energy policy, 35 (2007) 2590.

[2] A. Demirbas, Global renewable energy projections, Energy Sources, Part B, 4 (2009) 212.

[3] D.M. Rowe, Thermoelectrics handbook: macro to nano, CRC press (2005).

[4] L.E. Bell, Cooling, heating, generating power, and recovering waste heat with thermoelectric systems, Science, 321 (2008) 1457.

[5] G.S. Nolas, J. Sharp, J. Goldsmid, Thermoelectrics: basic principles and new materials developments, Springer Science & Business Media (2013).

[6] X. Zhang, L.-D. Zhao, Thermoelectric materials: Energy conversion between heat and electricity, Journal of Materiomics, 1 (2015) 92.

[7] K.F. Hsu, S. Loo, F. Guo, W. Chen, J.S. Dyck, C. Uher, T. Hogan, E. Polychroniadis, M.G. Kanatzidis, Cubic $AgPb_mSbTe_{2+m}$: bulk thermoelectric materials with high figure of merit, Science, 303 (2004) 818.

[8] B. Poudel, Q. Hao, Y. Ma, Y. Lan, A. Minnich, B. Yu, X. Yan, D.

Wang, A. Muto, D. Vashaee, High-thermoelectric performance of nanostructured bismuth antimony telluride bulk alloys, Science, 320 (2008) 634.

[9] W. Xie, X. Tang, Y. Yan, Q. Zhang, T.M. Tritt, Unique nanostructures and enhanced thermoelectric performance of melt-spun BiSbTe alloys, Applied Physics Letters, 94 (2009) 102111.

[10] S. Bathula, M. Jayasimhadri, N. Singh, A. Srivastava, J. Pulikkotil, A. Dhar, R. Budhani, Enhanced thermoelectric figure-of-merit in spark plasma sintered nanostructured n-type SiGe alloys, Applied Physics Letters, 101 (2012) 213902.

[11] B. Yu, M. Zebarjadi, H. Wang, K. Lukas, H. Wang, D. Wang, C. Opeil, M. Dresselhaus, G. Chen, Z. Ren, Enhancement of thermoelectric properties by modulation-doping in silicon germanium alloy nanocomposites, Nano letters, 12 (2012) 2077.

[12] L.D. Zhao, S.H. Lo, Y. Zhang, H. Sun, G. Tan, C. Uher, C. Wolverton, V.P. Dravid, M.G. Kanatzidis, Ultralow thermal conductivity and high thermoelectric figure of merit in SnSe crystals, Nature, 508 (2014) 373.

[13] L.D. Zhao, G. Tan, S. Hao, J. He, Y. Pei, H. Chi, H. Wang, S. Gong, H. Xu, V.P. Dravid, C. Uher, G.J. Snyder, C. Wolverton, M.G. Kanatzidis, Ultrahigh power factor and thermoelectric performance in hole-doped single-crystal SnSe, Science, 351 (2016) 141.

[14] L.D. Zhao, C. Chang, G.J. Tan, M.G. Kanatzidis, SnSe: a remarkable new thermoelectric material, Energy & Environmental Science, 9 (2016) 3044.

[15] B.R. Ortiz, H. Peng, A. Lopez, P.A. Parilla, S. Lany, E.S.J.P.C.C.P. Toberer, Effect of extended strain fields on point defect phonon scattering in thermoelectric materials, 17 (2015) 19410.

[16] C.-L. Chen, H. Wang, Y.-Y. Chen, T. Day, G.J. Snyder, Thermoelectric properties of p-type polycrystalline SnSe doped with Ag, Journal of Materials Chemistry A, 2 (2014) 11171.

[17] L. Zhang, J. Wang, Q. Sun, P. Qin, Z. Cheng, Z. Ge, Z. Li, S.J.A.E.M. Dou, Three-Stage Inter-Orthorhombic Evolution and High Thermoelectric Performance in Ag-Doped Nanolaminar SnSe Polycrystals, 7 (2017) 1700573.

[18] T.-R. Wei, G. Tan, X. Zhang, C.-F. Wu, J.-F. Li, V.P. Dravid, G.J. Snyder, M.G.J.J.o.t.A.C.S. Kanatzidis, Distinct impact of alkali-ion doping on electrical transport properties of thermoelectric p-type polycrystalline SnSe, 138 (2016) 8875.

[19] N.K. Singh, S. Bathula, B. Gahtori, K. Tyagi, D. Haranath, A.J.J.o.A. Dhar, Compounds, The effect of doping on thermoelectric performance of p-type SnSe: Promising thermoelectric material, 668 (2016) 152.

[20] J. Li, D. Li, X. Qin, J. Zhang, Enhanced thermoelectric

performance of p-type SnSe doped with Zn, Scripta Mater, 126 (2017) 6.

[21] Z.-H. Ge, D. Song, X. Chong, F. Zheng, L. Jin, X. Qian, L. Zheng, R.E. Dunin-Borkowski, P. Qin, J.J.J.o.t.A.C.S. Feng, Boosting the thermoelectric performance of (Na, K)-codoped polycrystalline SnSe by synergistic tailoring of the band structure and atomic-scale defect phonon scattering, 139 (2017) 9714.

[22] S. Chandra, A. Banik, K. Biswas, n-Type Ultrathin few-layer nanosheets of Bi-doped SnSe: Synthesis and thermoelectric properties, ACS Energy Letters, 3 (2018) 1153.

[23] S. Chandra, K. Biswas, Realization of High Thermoelectric Figure of Merit in Solution Synthesized 2D SnSe Nanoplates via Ge Alloying, Journal of the American Chemical Society, 141 (2019) 6141.

[24] A. Banik, S. Roychowdhury, K. Biswas, The journey of tin chalcogenides towards high-performance thermoelectrics and topological materials, Chem. Commun., 54 (2018) 6573.

[25] S.R. Popuri, M. Pollet, R. Decourt, F.D. Morrison, N.S. Bennett, J.W.G. Bos, Large thermoelectric power factors and impact of texturing on the thermal conductivity in polycrystalline SnSe, J. Mater. Chem. C, 4 (2016) 1685.

[26] Y. Fu, J. Xu, G.Q. Liu, J. Yang, X. Tan, Z. Liu, H. Qin, H. Shao, H.

Jiang, B. Liang, J. Jiang, Enhanced thermoelectric performance in p-type polycrystalline SnSe benefiting from texture modulation, Journal of Materials Chemistry C, 4 (2016) 1201.

[27] X. Wang, J.T. Xu, G.Q. Liu, X.J. Tan, D.B. Li, H.Z. Shao, T.Y. Tan, J. Jiang, Texturing degree boosts thermoelectric performance of silver-doped polycrystalline SnSe, NPG Asia Mater., 9 (2017) 6.

[28] D. Feng, Z.-H. Ge, D. Wu, Y.-X. Chen, T. Wu, J. Li, J. He, Enhanced thermoelectric properties of SnSe polycrystals via texture control, Physical Chemistry Chemical Physics, 18 (2016) 31821.

[29] M.S. Song, S.M. Choi, W.S. Seo, J. Moon, K.W. Jang, Thermoelectric and mechanical properties of Zn_4Sb_3 polycrystals sintered by spark plasma sintering, Journal of the Korean Physical Society, 60 (2012) 1735.

[30] D. Li, J.C. Li, X.Y. Qin, J. Zhang, C.J. Song, L. Wang, H.X. Xin, Thermoelectric Performance for SnSe Hot-Pressed at Different Temperature, Journal of Electronic Materials, 46 (2017) 79.

[31] P. Zou, G.Y. Xu, S. Wang, P.L. Chen, F.Z. Huang, Effect of high pressure sintering and annealing on microstructure and thermoelectric properties of nanocrystalline $Bi_2Te_{2.7}Se_{0.3}$ doped with Gd, Prog. Nat. Sci., 24 (2014) 210.

[32] L. Han, S.H. Spangsdorf, N.V. Nong, L.T. Hung, Y.B. Zhang, H.N. Pham, Y.Z. Chen, A. Roch, L. Stepien, N. Pryds, Effects of spark

plasma sintering conditions on the anisotropic thermoelectric properties of bismuth antimony telluride, RSC Adv., 6 (2016) 59565.
[33] J.H. Sui, J. Li, J.Q. He, Y.L. Pei, D. Berardan, H.J. Wu, N. Dragoe, W. Cai, L.D. Zhao, Texturation boosts the thermoelectric performance of BiCuSeO oxyselenides, Energy & Environmental Science, 6 (2013) 2916.
[34] C. Mei, Y. Li, G.D. Li, M.F. Li, P.C. Zhai, The Effect of High-Pressure Sintering Process on the Microstructure and Thermoelectric Properties of $CoSb_3$, Journal of Electronic Materials, 38 (2009) 1194.
[35] J. He, J.T. Xu, X.J. Tan, G.Q. Liu, H.Z. Shao, Z. Liu, H.C. Jiang, J. Jiang, Synthesis of SnTe/$AgSbSe_2$ nanocomposite as a promising lead- free thermoelectric material, J. Materiomics, 2 (2016) 165.
[36] J.H. Kim, Y.J. Song, J.S. Rhyee, B.S. Kim, S.D. Park, H.J. Lee, J.W. Shin, Small-polaron transport and thermoelectric properties of the misfit-layer composite $(BiSe)_{(1.09)}TaSe_2/TaSe_2$, Physical Review B, 87 (2013) 6.
[37] F. Lotgering, Topotactical reactions with ferrimagnetic oxides having hexagonal crystal structures—I, Journal of Inorganic and Nuclear Chemistry, 9 (1959) 113.
[38] S. Sassi, C. Candolfi, J.-B. Vaney, V. Ohorodniichuk, P. Masschelein, A. Dauscher, B. Lenoir, Assessment of the

thermoelectric performance of polycrystalline p-type SnSe, Applied Physics Letters, 104 (2014) 212105.

[39] Y.J. Fu, J.T. Xu, G.Q. Liu, J.K. Yang, X.J. Tan, Z. Liu, H.M. Qin, H.Z. Shao, H.C. Jiang, B. Liang, J. Jiang, Enhanced thermoelectric performance in p-type polycrystalline SnSe benefiting from texture modulation, J. Mater. Chem. C, 4 (2016) 1201.

[40] J. Yan, F. Ke, C. Liu, L. Wang, Q. Wang, J. Zhang, G. Li, Y. Han, Y. Ma, C. Gao, Pressure-driven semiconducting-semimetallic transition in SnSe, Phys. Chem. Chem. Phys., 18 (2016) 5012.

[41] A. Ghosh, M. Gusmão, P. Chaudhuri, S.M. de Souza, C. Mota, D. Trichês, H. Frota, Electrical properties of SnSe under high-pressure, Computational Condensed Matter, 9 (2016) 77.

[42] P. Maycock, Thermal conductivity of silicon, germanium, III-V compounds and III-V alloys, Solid-state electronics, 10 (1967) 161.

[43] Y. Li, F. Li, J. Dong, Z. Ge, F. Kang, J. He, H. Du, B. Li, J.-F. Li, Enhanced mid-temperature thermoelectric performance of textured SnSe polycrystals made of solvothermally synthesized powders, Journal of Materials Chemistry C, 4 (2016) 2047.

[44] H. Leng, M. Zhou, J. Zhao, Y. Han, L. Li, Optimization of thermoelectric performance of anisotropic $Ag_xSn_{1-x}Se$ compounds, Journal of Electronic Materials, 45 (2016) 527.

[45] J. Gao, G. Xu, Thermoelectric performance of polycrystalline

$Sn_{1-x}Cu_xSe$ (x= 0–0.03) prepared by high pressure method, Intermetallics, 89 (2017) 40–45.

[46] X. Liang, Impact of grain boundary characteristics on lattice thermal conductivity: A kinetic theory study on ZnO, Phys. Rev. B, 95 (2017) 7.

[47] S. Wang, S. Hui, K.L. Peng, T.P. Bailey, X.Y. Zhou, X.F. Tang, C. Uher, Grain boundary scattering effects on mobilities in p–type polycrystalline SnSe, Journal of Materials Chemistry C, 5 (2017) 10191–10200.

Notice; This chapter has been accepted for publication in *Bulletin of Materials Science* on Sept. 2019. The title is "Effect of sintering pressure on electrical transport and thermoelectric properties of polycrystalline SnSe" and the authors are Jun–Young Cho, Muhammad Siyar, Seung–Hwan Bae, Junsik Mun, Miyoung Kim, Woo Chan Jin, Seong–Hyeon Hong and Chan Park.

CHAPTER 6. Electrical Transport and Thermoelectric Properties of SnSe–SnTe Solid Solution

6.1 Introduction

Thermoelectric (TE) materials, which can reversibly convert thermal energy into electrical energy, has been considered as a way to solve energy crisis and environmental problems [1, 2]. The performance of a TE material is evaluated by the dimensionless figure of merit (ZT), $ZT = (S^2\sigma/k)T$, where S, σ, k and T are Seebeck coefficient, electrical conductivity, thermal conductivity and absolute temperature, respectively [3]. Large ZT values can be obtained by high power factor PF ($=S^2\sigma$) and low thermal conductivity. To increase both σ and S simultaneously is difficult because they tend to change in the opposite direction as charge carrier concentration changes. And it is also very difficult to increase σ and to decrease k at the same time because the electronic component of k tends to change in the same direction as the change of σ. And so the effort to find TE materials which have performance high enough to be used in devices, which consist of earth–abundant and non–toxic elements, is continuing today.

Over the past several decades, various TE materials such as

Bi_2Te_3- , PbTe- and ZnSb-based compounds, skutterudites, and half-Heusler compounds have been integrated into TE device [4-7]. In recent years, tin selenide (SnSe) which contains non-toxic and earth-abundant elements has been considered as a promising TE material since Zhao et al. [8] reported remarkable ZT value of ~2.6 at 923K (the world record to date) along the b-axis in its single crystal SnSe. It, however, is still difficult to use single crystal TE materials in devices because of poor mechanical properties and high production cost. For these reasons, the researches on SnSe have focused on developing high performance polycrystalline SnSe [8-11]. Many approaches to obtain polycrystalline SnSe which has TE performance similar to that of single crystal through texturing [9], doping [10] and nanoinclusion [11] have been reported. The ZT values of polycrystalline SnSe which is lower than that of single crystal SnSe come mainly from its relatively low electrical conductivity (σ) and high thermal conductivity (k) [12]. Recently, Chung et al. [13] reported that the high thermal conductivity in polycrystalline SnSe is attributed to surface tin oxides and a ZT value of ~2.5 at 773K in polycrystalline SnSe doped with 5% PbSe by removing surface oxide, which is the highest ZT value reported so far.

One potential way to optimize the TE performance of

polycrystalline SnSe is making solid solution which has been used in other TE systems such as $Bi_{2-x}Sb_xTe_3$, $Mg_2Si_{1-x}Sn$ and $PbTe_{1-x}Se_x$ [14−17]. In solid solution, electrical transport properties can be improved by optimizing carrier concentration through band gap engineering while lattice thermal conductivity can be suppressed by enhanced phonon scattering through atomic disorder and mass difference [18]. To determine the element for forming the solid solutions, Hume−Rothery rules are usually used [19, 20], which indicate that the solute and the solvent atoms should have: (1) similar size, (2) similar crystal structure, (3) similar valence state and (4) similar electronegativity

There are a few reports on TE properties of SnSe−based solid solutions [21−26]. Han et al. [21] investigated the TE properties of $SnS_{1-x}Se_x$ solid solutions and reported that a ZT of ~ 0.82 in $SnS_{0.2}Se_{0.8}$, which was more than four times higher than that of SnS, was achieved by the increase of carrier mobility and the reduction of lattice thermal conductivity. Wei et al. [23] reported that single−phase $Sn_{1-x}Pb_xSe$ solid solutions were formed up to $x = 0.12$, and the highest ZT was ~ 0.85 which was obtained in the sample with $x = 0$, which means that there was no significant enhancement in ZT value by Pb substitution. Saini et al. [24] reported that, the electrical properties of $SnTe_xSe_{1-x}$ ($0 < x < 1$) solid solutions which exhibit p−

type conduction behaviours can be improved with the increase of Te contents. Hong et al. [25] also reported that $SnSe_{1-x}Te_x$ ($0 < x < 0.2$) nanoplates prepared by solvothermal method has p-type conduction and a ZT of ~ 1.1 was achieved in $SnSe_{0.9}Te_{0.1}$ which was higher than that of SnSe (ZT ~ 0.97). On the other hand, Chen et al. [26] reported that $SnSe_{1-x}Te_x$ (x= 0, 0.0625) has n-type conduction behaviour, and the incorporation of Te does not improve the electrical transport properties of SnSe. Thus, the precise role of Te on the TE properties of $SnSe_{1-x}Te_x$ solid solution is still not fully understood, and a detailed study of the TE transport properties of $SnSe_{1-x}Te_x$ solid solution is needed.

The purpose of this study was to gain a better understanding of the effect of Te substitution on the TE properties of the SnSe-SnTe solid solution. In this study, $SnSe_{1-x}Te_x$ ($0 \leq x \leq 1$) were prepared by mechanical alloying and spark plasma sintering, and their TE transport properties were investigated. Here we report the solubility limit of Te in $SnSe_{1-x}Te_x$ is somewhere between x = 0.3 and 0.5 and a ZT of ~ 0.78 (x = 0.3) is obtained at 825K (the ZT of SnSe is 0.7). The improvement of ZT is attributed to the increase of electrical conductivity which can be obtained from the tuning of carrier concentration and to the decrease of lattice thermal conductivity obtained by enhanced phonon scattering through point defect.

6.2 Experimental Procedure

6.2.1 Synthesis of Polycrystalline SnSe–SnTe Solid Solution

Figure 6–1 shows the experimental procedure. Sn (99.99%, Sigma Aldrich), Se (99.99%, Sigma Aldrich) and Te (99.99%, Kunjundo Chemicals) powders were used to synthesize the polycrystalline SnSe–SnTe solid solutions. High purity single elements of Sn, Se and Te were weighed according to the stoichiometry of $SnSe_{1-X}Te_x$ (x= 0, 0.1, 0.3, 0.5, 0.8 and 1), loaded into a steel crucible (100 mL) at a ratio of 5:1 with steel balls of different diameters (3mm and 1mm) in an Ar filled glove box and then subjected to mechanical alloying (MA). ~35% of the crucible was filled with the powder mixture and balls. The polycrystalline $SnSe_{1-X}Te_x$ powders were synthesized by MA at 250 rpm for 4 h, which was confirmed by XRD and the result were shown in figure 6–2.

Figure 6-1. Experimental procedure.

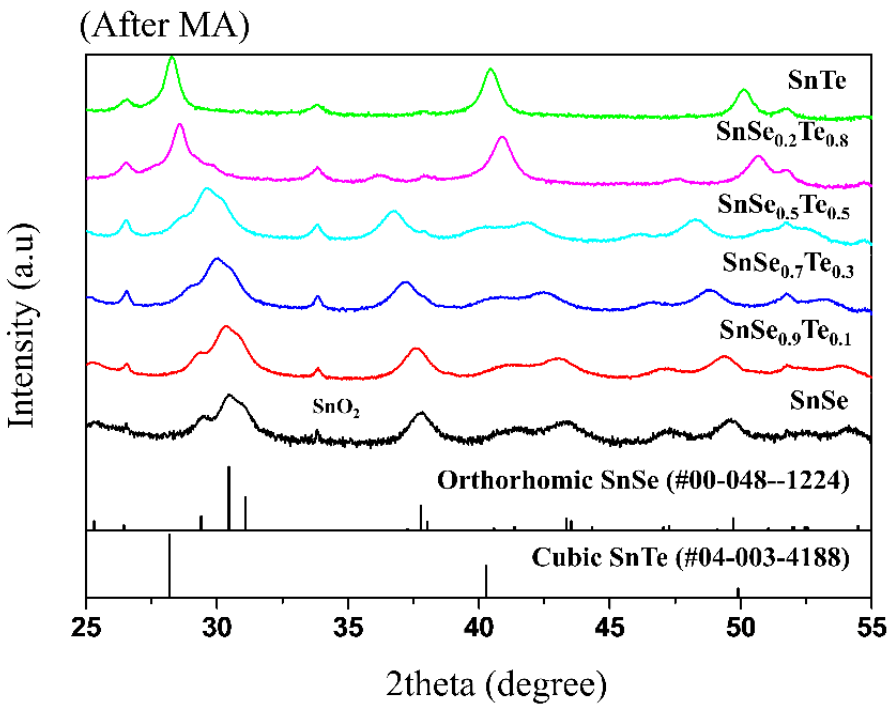

Figure 6-2. Theta-2theta XRD patterns of the polycrystalline $SnSe_{1-x}Te_x$ (x= 0, 0.1, 0.3, 0.5, 0.8 and 1) powder prepared using mechanical alloying.

6.2.2 Fabrication of Polycrystalline Bulk SnSe-SnTe Solid Solution

In order to fabricate a bulk sample, the MA-derived powders were ground in an alumina mortar and sieved through a 140-mesh stainless steel mesh, loaded into a 12.5 mm-diameter graphite mold and was spark plasma sintered in vacuum (~ 2 x 10^{-3} Torr) at 850K for 10min under uni-axial pressure of 30 MPa.

6.2.3 Characterization

The qualitative phase analyses of the disk-shaped sintered samples were carried out using X-ray diffraction (XRD, D-8 Advanced, Bruker) with Cu K_{α} radiation. The microstructures of fracture surface of the sintered samples were observed using a field emission scanning electron microscope (FE-SEM, SU-70, JEOL), and the elemental distribution analyses were conducted on the polished surface of bulk samples using an energy-dispersive X-ray spectroscopy (EDS). The elemental ratios of the bulk samples were determined by Electron Probe Micro-Analysis (EPMA). The dish-shaped sintered samples were cut into bars with dimensions of 1.5 x 1.5 x 7 mm^3. The bar-shaped samples were used for simultaneous measurement of Seebeck coefficient and electrical conductivity using

a commercial measurement equipment (Seepel Corp) under an Ar atmosphere from room temperature to 850 K. Carrier concentrations of the SnSe samples were obtained using a Hall measurement system (HMS 3000, Ecopia) at room temperature. The optical characteristics of the $SnSe_{1-X}Te_x$ were determined using a UV−Vis−NIR spectrometer (UV−3600 plus, Shimadzu). The reflectance spectra were obtained over the wavelength range of 200 to 2600 nm with a step size of 1 nm.

The analyses of density of state (DOS) and the calculations of electronic band structure were carried out for the $SnSe_{1-X}Te_x$ using the atomic positions and the lattice parameters from the Rietveld analysis of each bulk sample, and the result are shown in table 6−1. The unit cell of SnSe consists of eight atoms, and there are four sites of Se which can be substituted by Te per unit cell. Therefore, we used homogenous solid solutions of x = 0, 0.125 and 0.250 to calculate electronic band structures of $SnSe_{1-x}Te_x$.

We performed the first−principles calculation using the Vienna ab initio simulation package (VASP) based on the density functional theory (DFT) [27]. The exchange and correlation energies were treated within the generalized gradient approximation (GGA) according to the Perdew−Burke−Ernzerhof (PBE) parameterization. Projector augmented−wave (PAW) potentials are used for electron−

ion interactions. A plane wave kinetic energy cutoff of 450 eV and 4 x 12 x 12 k−point sets were used. The self−consistent calculation for structural optimization cycles were repeated until the energy difference and force became smaller than 1 x 10^{-6} eV and 1 x 10^{-2} e V $Å^{-1}$, respectively. The standard PBE+U calculations were used to obtain the band gap energy.

The total thermal conductivity (k_{tot}) can be expressed as the sum of electronic thermal conductivity (k_e) and lattice thermal conductivity (k_{latt}). The k_{tot} was calculated by multiplying the specific heat (C_p), thermal diffusivity (D) and density (ρ). The C_p, D and ρ values were measured using the differential scanning calorimetry (DSC, Netzsch), the laser flash method (LFA457, Netzsch), and the Archimedes method, respectively. The k_e was obtained using the Wiedemann-Franz law, $k_e = L \sigma T$, where L, σ and T are Lorenz number, electrical conductivity and absolute temperature, respectively. The Lorenz number L which was obtained from fitting the Seebeck coefficient to the reduced chemical potential was used to obtain k_e [28, 29]. The k_{latt} was obtained by subtracting the k_e from the k_{tot}. The TE properties of all samples were measured perpendicular to the direction of the pressure applied during the SPS.

Table 6-1. Tin (Sn), selenium (Se) and tellurium (Te) atomic ratios and chemical compositions of polycrystalline $SnSe_{1-x}Te_x$ (x= 0, 0.1 and 0.3) obtained by electron probe micro-analyses (EPMA).

Nominal compositions	Sn (at%)	Se (at%)	Te (at%)	Analyzed compositions
SnSe	49.9	50.1	-	$Sn_{0.998}Se_{1.002}$
$SnSe_{0.9}Te_{0.1}$	50.1	45.2	4.7	$Sn_{1.002}Se_{0.904}Te_{0.094}$
$SnSe_{0.7}Te_{0.3}$	50.2	35.3	14.5	$Sn_{1.004}Se_{0.706}Te_{0.290}$

6.3 Results and Discussion

6.3.1 Phase Analysis of SnSe–SnTe Solid Solutions

Figure 6–3 shows the XRD patterns of the sintered $SnSe_{1-x}Te_x$ (x= 0, 0.1, 0.3, 0.5, 0.8 and 1) prepared using MA and spark plasma sintering. For all the sample, there is a peak at around 2theta = 34 which corresponds to SnO_2 is observed, which is consistent with the results of previous reports [30, 31]. Zhang et al. [31] reported that oxygen can be physically adsorbed on SnSe before SPS, and it can be chemically adsorbed on SnSe after SPS and transformed into oxides. However, the Sn–rich phase is not observed by EDS, and chemical compositions of all samples are close to the nominal ones (shown in Figure 6–4 and Table 6–1). And so, we assumed that the amount of SnO_2 inside the sintered samples is very small and almost the same in all the sintered samples, and the effect of SnO_2 on the TE properties was not accounted for in this study.

When x=0, all the peaks of the sample are matched with those of orthorhombic SnSe (PDF #00–048–1224). On the other hands, when x=1, all the peaks of the sample are matched with those of cubic SnTe (PDF #04–003–4188). As Te contents are increased, the peak positions of the samples tend to shift towards low 2θ

values, which indicates that the incorporation of Te induces lattice expansion (see the table 6-2) due the fact that Te has a larger atomic radius (0.21 nm) than Se (0.19 nm), which is consistent with the results previous reported [25]. When x = 0.5, diffraction peaks from SnSe and SnTe are observed simultaneously, which indicates the presence of both SnSe and SnTe. This implies that the solubility limit of Te element in $SnSe_{1-x}Te_x$ can be somewhere between x = 0.3 and 0.5. In this study, all the $SnSe_{1-x}Te_x$ samples were sintered at 850K. Volykhov et al. [32] reported that the solubility limit of Te in SnSe which depends on the temperature is ~0.35 at ~850K, which is consistent with the result of this study. The microstructures and TE properties of three samples (SnSe, $SnSe_{0.9}Te_{0.1}$ and $SnSe_{0.7}Te_{0.3}$) with Te content smaller than the solubility limit, were observed and measured, respectively, in this study.

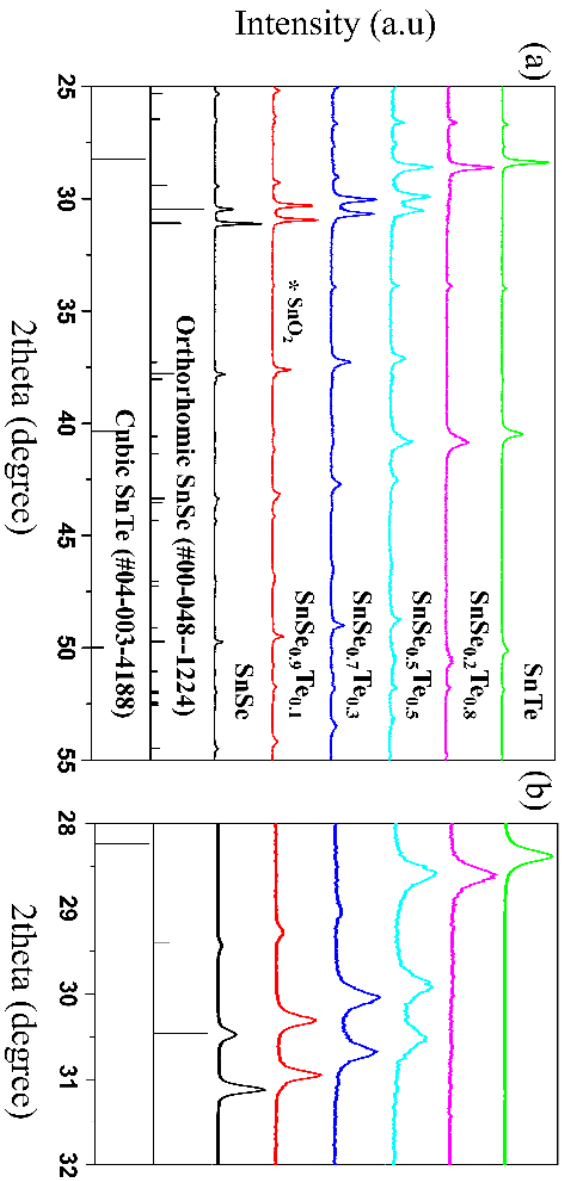

Figure 6-3. (a) Theta-2theta XRD patterns of the polycrystalline $SnSe_{1-x}Te_x$ (x= 0, 0.1, 0.3, 0.5, 0.8 and 1) and (b) featured 2θ profiles on expanded scale.

Table 6-2. The cell parameters of the polycrystalline $SnSe_{1-x}Te_x$ (x= 0, 0.1, 0.3, 0.5, 0.8 and 1) obtained by Rietveld refinement method using TOPAS software.

Sample	Composition	a(Å)	b(Å)	c(Å)	$\alpha = \beta = \gamma$
1	SnSe	11.495	4.152	4.442	90
2	$Sn(Se_{0.9}Te_{0.1})$	11.542	4.183	4.458	90
3	$Sn(Se_{0.7}Te_{0.3})$	11.659	4.227	4.483	90
4	$Sn(Se_{0.5}Te_{0.5})$	11.703	4.251	4.489	90
		6.243	6.243	6.243	90
5	$Sn(Se_{0.2}Te_{0.8})$	6.261	6.261	6.261	90
6	SnTe	6.315	6.315	6.315	90

6.3.2 Microstructure and Chemical Composition of SnSe–SnTe Solid Solutions

Figure 6–4 (a), (b) and (c) show the FE–SEM micrographs taken from the fracture surface of the polycrystalline $SnSe_{1-x}Te_x$ (x= 0, 0.1 and 0.3) samples, respectively. All the sintered $SnSe_{1-x}Te_x$ samples exhibit dense microstructure and plate–like grains. As the amount of Te is increased, no significant microstructural changes are observed. The relative densities of all samples measured by the Archimedes method were ~ 95%, and it can be expected that the effect of density on the TE properties of the $SnSe_{1-x}Te_x$ samples can be negligible. In order to determine the distribution of elements, EDS mapping was performed on the polished surface of the polycrystalline $SnSe_{1-x}Te_x$ (x= 0, 0.1 and 0.3), and the results are shown in Figure 6–5. EDS elemental mapping results show that the distributions of the element Sn, Se and Te are uniform. The atomic ratios and chemical compositions of all samples were determined by electron probe microanalysis (EPMA), and the result are shown in Table 6–1. The Sn/Se/Te atomic ratios of SnSe, $SnSe_{0.9}Te_{0.1}$ and $SnSe_{0.7}Te_{0.3}$ are 49.9/50.1/0, 50.1/45.2/4.7 and 50.2/35.3/14.5, respectively, which indicates that the analyzed chemical compositions of all samples are close to the nominal ones.

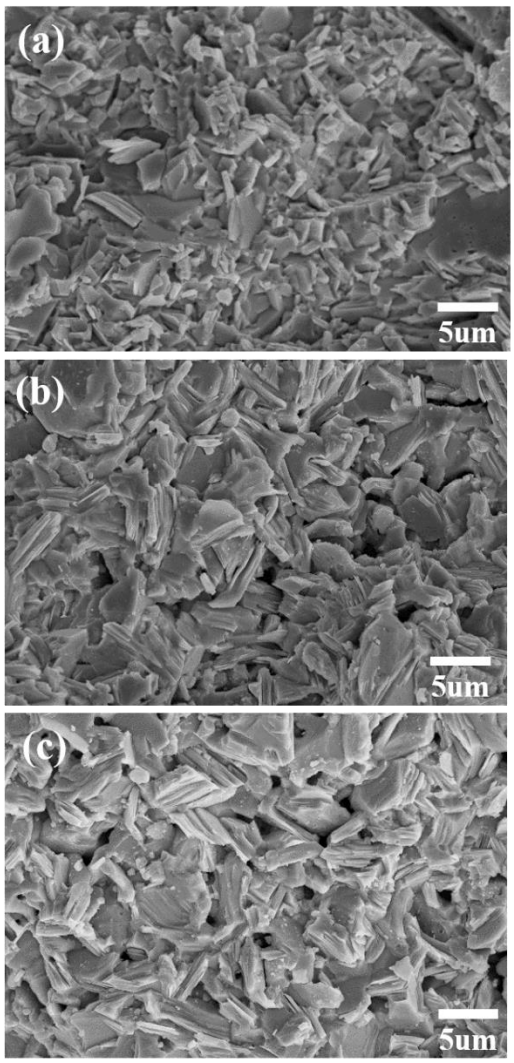

Figure 6-4. FE-SEM micrographs taken from the fracture surface of the polycrystalline (a) SnSe, (b) $SnSe_{0.9}Te_{0.1}$ and (c) $SnSe_{0.7}Te_{0.3}$. The surfaces of the samples were not polished.

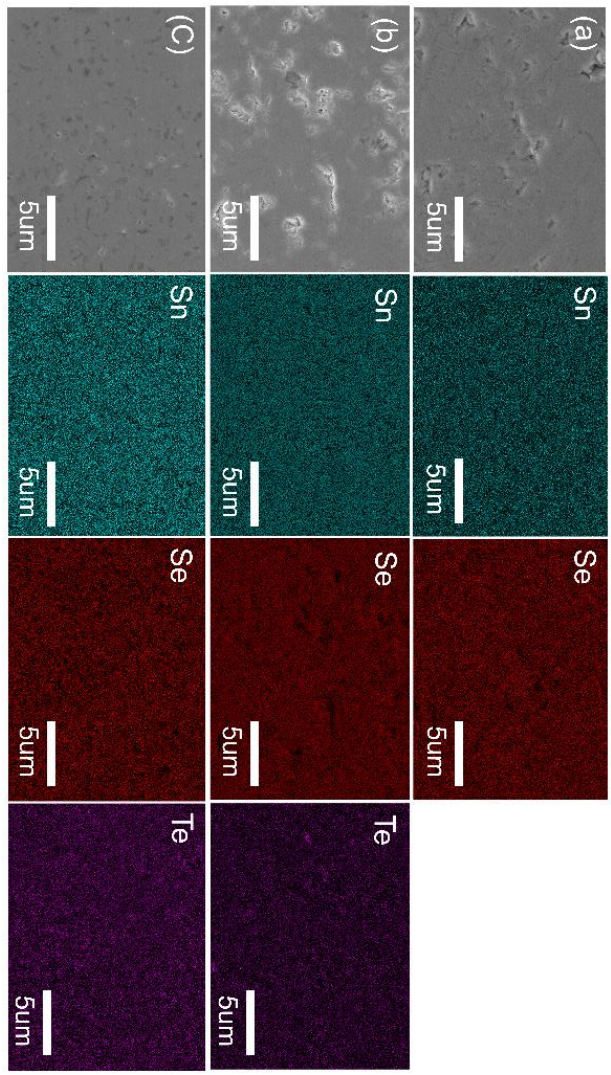

Figure 6-5. Electron probe microanalyzer (EPMA) images of (a) SnSe, (b) $SnSe_{0.9}Te_{0.1}$ and (c) $SnSe_{0.7}Te_{0.3}$. Images with (Sn), (Se) and (Te) show the distribution of the elements Sn, Se and Te, respectively.

6.3.3 Electrical conductivity and Seebeck coefficient of SnSe−SnTe solid solutions

Figure 6−6 (a) shows the temperature−dependency of electrical conductivity (σ) of the polycrystalline $SnSe_{1-x}Te_x$ (x= 0, 0.1 and 0.3). All the curves have the same trend of change: σ is increased with temperature first, decreased from 473K to 700K, and then rapidly increased over 790K again thereafter, which is consistent with the results of previous reports [9, 33−35]. Sassi et al. [33] and Zhang et al. [34] reported a reduction of σ around 505 K due to the melting of a very small amount of unreacted Sn. And Feng et al. [35] and Fu et al. [9] reported that an increase of σ at about 623K can be attributed to the thermal activation of minority carriers and a rapid increase of σ at 750 ~ 800K is due the phase transition of SnSe from Pnma to Cmcm. Zhao et al. [30] reported an anomalous jump in the heat capacity come from the phase transition. The heat capacity of SnSe measured by differential scanning calorimetry (DSC) (see the figure 6−7) showed that the phase transition may occur at around 790K. As the amount of Te is increased, the σ values are increased, and $SnSe_{0.7}Te_{0.3}$ has higher electrical conductivity than the other two at all the measurement temperatures. To understand the variations in electrical conductivity with increasing Te contents, the carrier

concentration (n) and carrier mobility (μ) of all samples were measured at room temperature, and the results are shown in Table 6-3. The n values of all the samples are positive, which indicates that hole is the major carrier and $SnSe_{1-x}Te_x$ is a p-type semiconductor. As the Te contents are increased, n is increased from 3.2×10^{18} to 1.3×10^{19}, while μ is decreased from 10.5 to 5.1 cm^{-2} V^{-1} s^{-1}, which means that the improvement in the electrical conductivity can be attributed to the increase of carrier concentration.

Figure 6-6 (b) shows the temperature-dependency of Seebeck coefficients (S) of the polycrystalline $SnSe_{1-x}Te_x$ (x= 0, 0.1 and 0.3). The change of S values with the increase of temperature in all samples shows the same behavior: S was increased from room temperature to 550K, and then decreased as temperature is further increased. The slight decrease in S value in the temperature range of 550~673K is known to result from the bipolar conduction by the excitation of the minor carrier [35]. The sharp decrease in S values from 790K is known as the result of the increase of carrier concentration by the phase transition of SnSe from Pnma to Cmcm [36]. Unlike the electrical conductivity, the S values of the samples are decreased with the increase of amount of Te. Generally, S values are determined by Pisarenko relationship [37], which indicates that S value is inversely proportional to the carrier concentration. As

shown in Table 6-3, the carrier concentration was increased with the increase of Te content, which can lead to the decrease of Seebeck coefficient. Therefore, the change in the electrical conductivity and the Seebeck coefficient can be influenced by the increase in carrier concentration. Figure 6-8 shows the power factor ($PF=S^2\sigma$) of the polycrystalline $SnSe_{1-x}Te_x$ obtained at different temperatures. The $SnSe_{0.7}Te_{0.3}$ sample shows a relatively high PF compared to the SnSe at all measurement temperatures, and the PF of $SnSe_{0.7}Te_{0.3}$ was ~1.02 x10^{-4} W m^{-1} K^{-1} at 300K and ~3.42 x10^{-4} W m^{-1} K^{-1} at 823K (this was the highest PF obtained in this study), which can mainly come from the improved electrical conductivity.

Table 6-3. Charge transport properties of polycrystalline $SnSe_{1-x}Te_x$ (x= 0, 0.1 and 0.3). The carrier concentration (n), carrier mobility (μ) and electrical conductivity (σ) were measured at room temperature.

Samples	Hall carrier concentration [n, cm^{-3}]	Carrier mobility [μ, $cm^{-2}\ V^{-1}\ s^{-1}$]	Conductivity [σ, $S\ cm^{-1}$]
SnSe	3.16×10^{18}	10.46	5.59
$SnSe_{0.9}Te_{0.1}$	8.38×10^{18}	6.56	9.30
$SnSe_{0.7}Te_{0.3}$	1.31×10^{19}	5.09	11.29

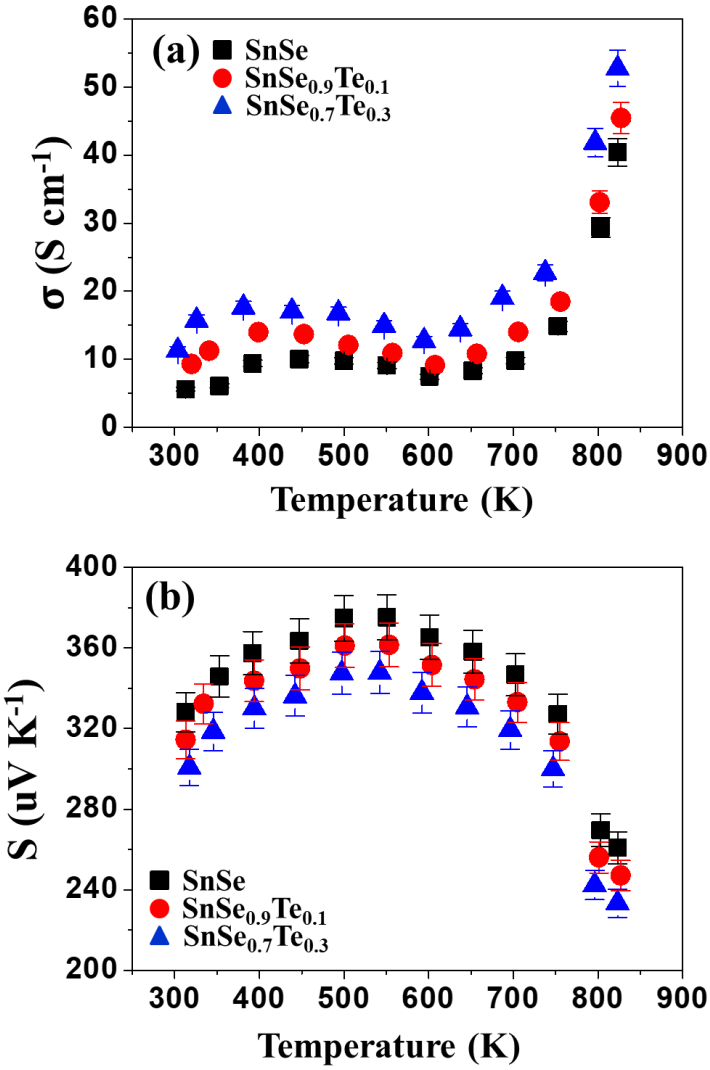

Figure 6-6. The temperature-dependency of (a) electrical conductivity (σ) and (b) Seebeck coefficient (S) of the polycrystalline $SnSe_{1-x}Te_x$ (x= 0, 0.1 and 0.3).

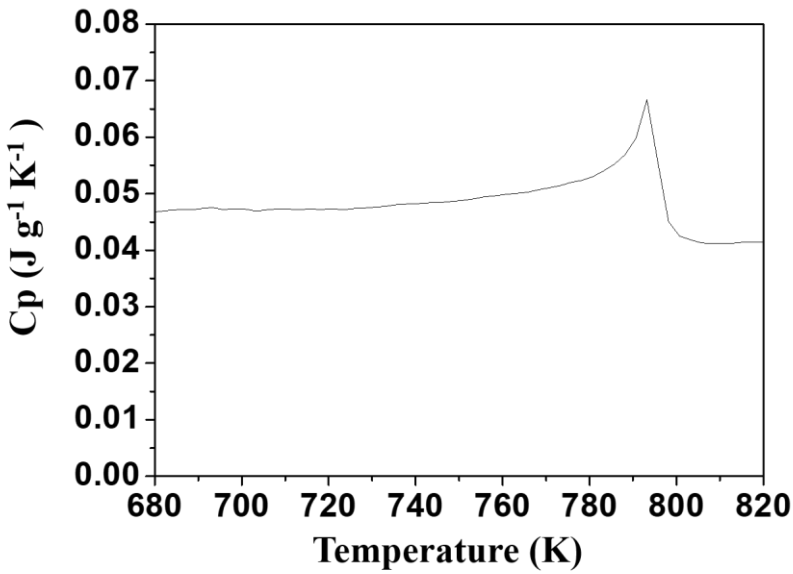

Figure 6-7. Heat capacity of SnSe measured by differential scanning calorimetry (DSC).

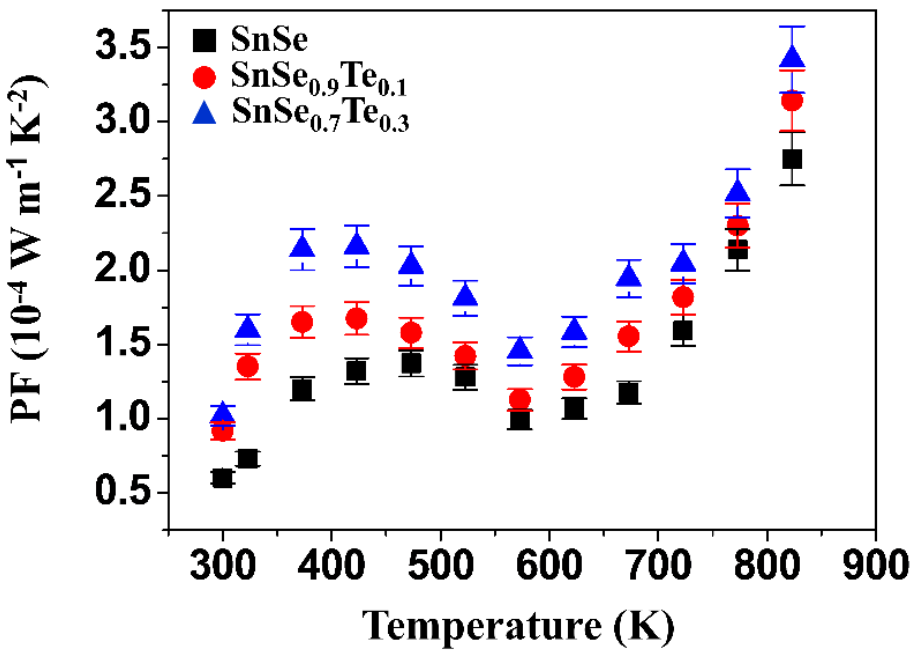

Figure 6-8. The power factor (PF) of the polycrystalline $SnSe_{1-x}Te_x$ (x= 0, 0.1 and 0.3) obtained at different temperatures.

6.3.4 Measurement of Bandgap and Calculation of Band structure of SnSe–SnTe solid solutions

The carrier concentration is closely related to the band gap energy, and its relation is given below [38].

$$n_i = CT^{\frac{3}{2}} \exp\left(\frac{-E_g}{2K_B T}\right) \quad (6.1)$$

Where n_i, C, T, k_B, and E_g are the carrier concentration, a constant, the absolute temperature, the Boltzmann constant, and the band gap energy, respectively. The carrier concentration of a material is inversely proportional to the band gap energy, which means that a reduction of the band gap can lead to the increase in carrier concentration. To investigate the band gaps of $SnSe_{1-x}Te_x$ (x= 0, 0.1 and 0.3) solid solutions, the band gap of each sample was determined from its absorption coefficient (α) obtained by UV–Vis–NIR spectroscopy. The relation between band gap energy (E_g) and the absorption coefficient (α) for indirect band transition can be established by the Tauc's relation given below [39].

$$(\alpha h\nu)^{1/2} = A(h\nu - E_g) \quad (6.2)$$

where A, h and ν are a constant, the Planck's constant and the frequency of radiation, respectively. Figure 6–9 shows $(\alpha h\nu)^2$ vs. ($h\nu$) plots of the polycrystalline $SnSe_{1-x}Te_x$ (x= 0, 0.1 and 0.3). The

optical band gap of each sample was obtained from the extrapolation of the linear region of the plot to the $h\nu$ axis, and the results are shown in the inset of Figure 6-9. The obtained band gap of SnSe was 0.88 eV, and it is in good agreement with the result of optical absorption measurement (0.90 eV) reported by Shi et al [40]. The band gaps of $SnSe_{0.9}Te_{0.1}$ and $SnSe_{0.7}Te_{0.3}$ were 0.76 and 0.64 eV, respectively, which indicates that the band gaps of $SnSe_{1-x}Te_x$ are decreased with increasing Te contents, which is consistent with the results reported by Wei et al [21]. To further understand the decrease in band gap, density of states (DOS) and band structures of $SnSe_{1-x}Te_x$ were obtained using DFT calculation. The bandgaps measured using UV-VIS-NIR spectrum and those calculated by DFT were compared.

Figure 6-10 (a), (b) and (c) show the electronic band structures of the polycrystalline $SnSe_{1-x}Te_x$ (x= 0, 0.125, and 0.25), respectively. The band structures were obtained by the first principle calculations using the VASP based on the DFT. The first and the second conduction band maximum (CBM1 and CBM2) are shown in the Γ-F and Z-Γ directions, respectively, and the first and second valence band minimum (VBM1 and VBM2) are shown in the Z-Γ and Γ-F directions, respectively, which means that the $SnSe_{1-x}Te_x$ have indirect band gap. The calculated band gap of SnSe was 0.68 eV, and

it is different from the measured band gap of SnSe, which was 0.88 eV (Figure 6-9). Chen et al. [26] and Su et al. [41] reported that the difference between measured and calculated bandgap can be caused by a well-known drawback from standard DFT calculation. The measurement and the calculation of the band gap energy show that the band gaps of the $SnSe_{1-x}Te_x$ are increased with the increase of Te content.

Figure 6-11 (a) - (c) shows the projected density of states of $SnSe_{1-x}Te_x$. For SnSe, the valence band maximum (VBM) is mainly contributed by Se-p orbital, while conduction band minimum (CBM) is occupied by Sn-p orbital. With increasing Te contents, VBM is mainly contributed by Sn-s and Te-p orbital hybridization in the VB, while the major part of the CBM is occupied by Sn-p orbital. The Sn-p orbital was shifted toward the Fermi level (E_F), leading to the CBM down to the Fermi level (E_F). This resulted in a band gap reduction, which is consistent with the result reported by Chen et al [26]. They reported that the interaction between Sn and Te orbitals can move the CBM towards the Fermi level (E_F) and consequently reduce the band gap. Therefore, the increase of electrical conductivity and the decrease of the Seebeck coefficient in this study are mainly caused by the increase of carrier concentration due to the band gap reduction.

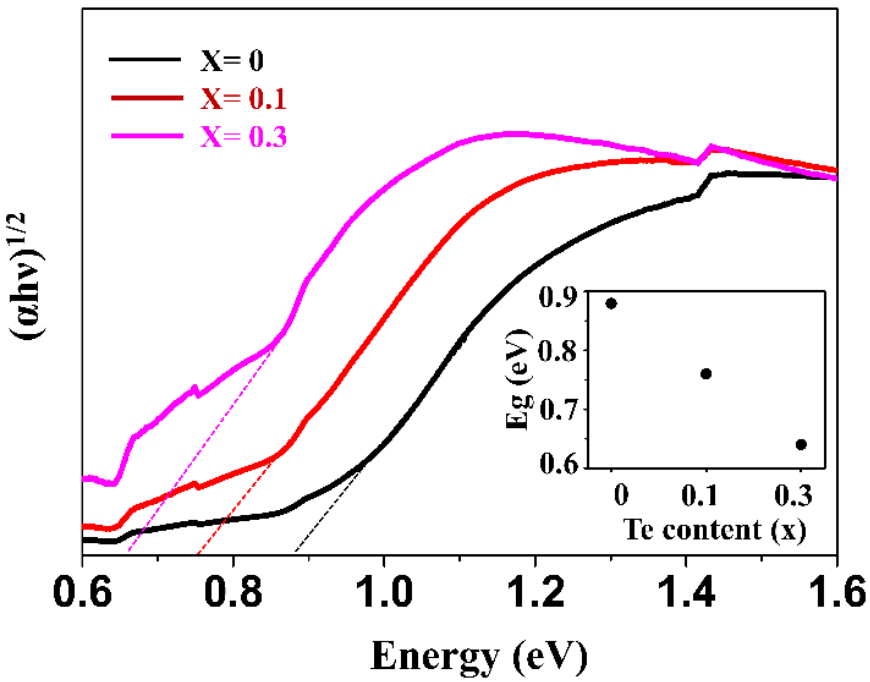

Figure 6-9. ($\alpha h\nu$)$^{1/2}$ versus ($h\nu$) plots of the polycrystalline $SnSe_{1-x}Te_x$ (x= 0, 0.1 and 0.3) obtained by UV-Vis-NIR spectrum. The inset shows the optical band gap versus Te content. The band gap value for each sample was obtained by extrapolating these plots to the x-axis.

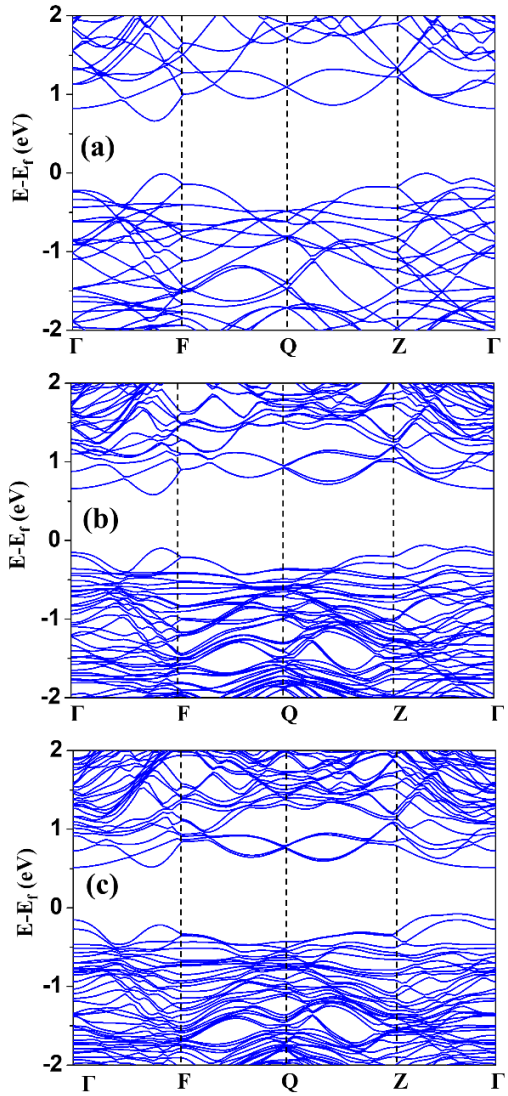

Figure 6-10. Electronic band structures of the polycrystalline (a) SnSe, (b) $SnSe_{0.725}Te_{0.125}$ and (c) $SnSe_{0.75}Te_{0.25}$, respectively.

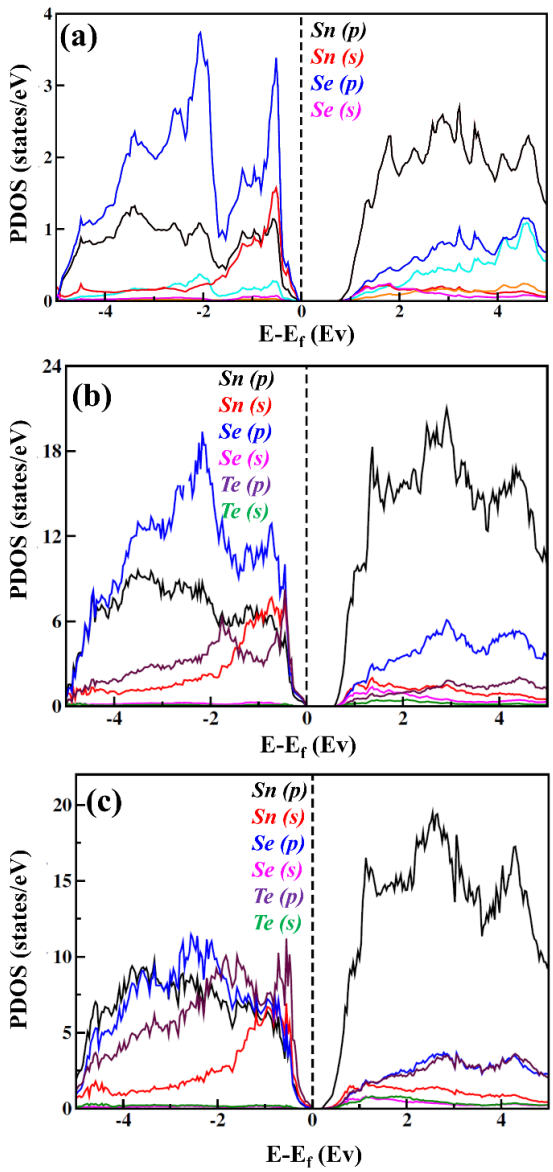

Figure 6-11. The projected density of states per atom of (a) SnSe, (b) $SnSe_{0.725}Te_{0.125}$

6.3.5 Thermal Conductivity and ZT of SnSe–SnTe Solid Solutions

Figure 6–12 (a) shows the temperature–dependency of total thermal conductivities (k_{tot}) of the polycrystalline $SnSe_{1-x}Te_x$. All samples show the same behavior with temperature: k_{tot} is generally decreased up to 790K, and then slightly increased. The increase in k_{tot} is known as the result of the phase transition of the SnSe from Pnma to Cmcm [42]. k_{tot} of $SnSe_{0.7}Te_{0.3}$ is lower than that of SnSe at all measurement temperatures. k_{tot} is expressed as the sum of electronic thermal conductivity (k_e) and lattice thermal conductivity (k_{latt}). In order to better understand the low k_{tot} of $SnSe_{0.3}Te_{0.7}$, the k_{tot} of all samples were separated into k_e and k_{latt}, and the results are shown in Figure 6–12 (b). The k_{tot} and k_{latt} of SnSe at 300K are 0.75 and 0.74 W m^{-1} K^{-1}, respectively, which indicates that the k_{tot} comes mainly from the k_{latt}. The k_{latt} of the samples were decreased with the increase of Te content. The atomic mass of Se and Te are 78.96 g mol^{-1} and 127.6 g mol^{-1}, and the atomic radius of them are 0.19 nm and 0.21 nm, respectively. The atomic mass and size difference between Se and Te can cause the fluctuation of mass and strain field, which can lead to the increase in the phonon scattering at point defects [21]. And so, the decrease in k_{latt} with the increase of Te

content can come from the increased amount of phonon scattering. The k_{latt} can be explained in terms of Umklapp scattering which is used for defect-free crystalline materials [43]. The polycrystalline SnSe, however, can have a lot of defects due to Te substitution, and so the phonon scattering by point defects is used to explain the decrease in k_{latt} with the increase of Te content in this study.

Figure 6-13 shows the figure of merits (ZT) of the polycrystalline $SnSe_{1-x}Te_x$, which were obtained from the electrical conductivity, Seebeck coefficient and thermal conductivity measured at different temperatures. The ZT value of $SnSe_{0.7}Te_{0.3}$ is higher than that of SnSe at all measurement temperatures. The highest ZT obtained in this study was ~0.78 at 823K of $SnSe_{0.7}Te_{0.3}$, which can be attributed to the improvement of electrical conductivity and the reduction of lattice thermal conductivity.

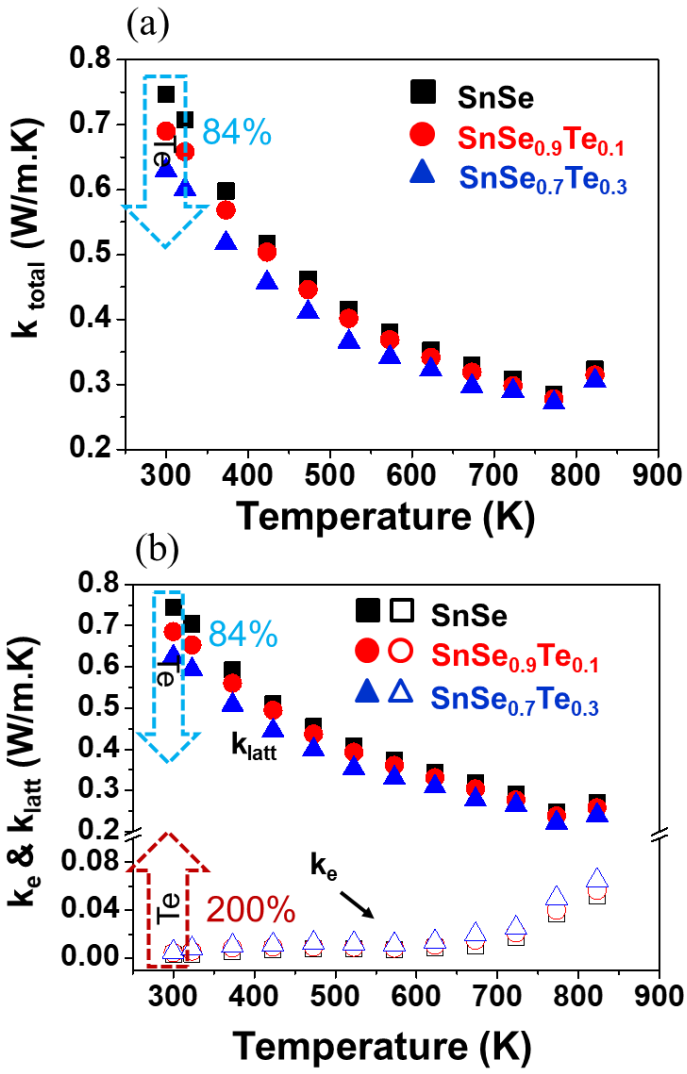

Figure 6-12. The temperature-dependency of (a) total thermal conductivity (k_{tot}), (b) electronic thermal conductivity (k_e) and the lattice thermal conductivity (k_{latt}) of the polycrystalline $SnSe_{1-x}Te_x$. (hollow shapes – k_e, filled shapes – k_{latt}).

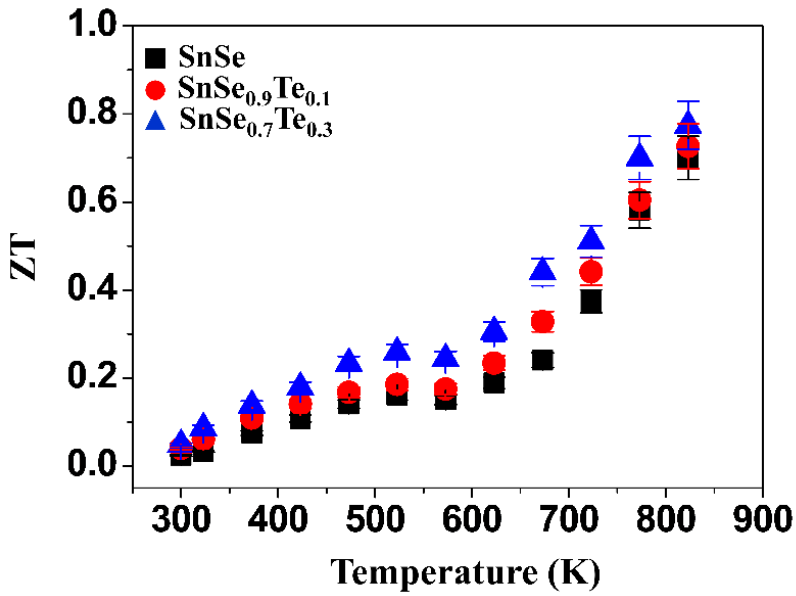

Figure 6-13. The figure of merits (ZT) of the polycrystalline SnSe1−xTex measured at different temperatures.

6.4 Summary

In this study, the thermoelectric (TE) properties of polycrystalline $SnSe_{1-x}Te_x$ solid solutions were investigated. SnSe–SnTe solid solutions were prepared by mechanical alloying and spark plasma sintering. XRD and EPMA analyses showed that the solubility limit of Te in $SnSe_{1-x}Te_x$ is somewhere between x = 0.3 and 0.5. Hall measurement showed that carrier concetration was increased with the increase of Te contents. The measurements of band gap using UV–VIS–NIR spectrum and calculation of band gap from DFT showed that the band gap was decreased as the amount of Te was increased, which can lead to the increase of carrier concentration. The increase in electrical conductivity and the reduction of Seebeck coefficeint of $SnSe_{1-x}Te_x$ were observed, which can result from the increase of carrier concentration. The thermal conductivity was decreased with increasing Te contents. Te has a larger atomic mass and size than Se, and the presence of Te at Se site can act as an effective point defect, which can increase phonon scattering and reduce lattice thermal conductivity. A ZT of ~0.78 was obtained at 823K from the $SnSe_{0.7}Te_{0.3}$, which was ~11% higher than that of SnSe. This study shows that polycrystalline $SnSe_{1-x}Te_x$ can have improved TE properties compared to SnSe which can be attributed to the increase in electrical conductivity and the decrease in the lattice thermal conductivity.

6.5 References

[1] G.J. Snyder, E.S. Toberer, Complex thermoelectric materials, Nature Materials, 7 (2008) 105.

[2] A. Demirbas, Global renewable energy projections, Energy Sources, Part B, 4 (2009) 212.

[3] D.M. Rowe, Thermoelectrics handbook: macro to nano, CRC press (2005).

[4] G.S. Nolas, D.T. Morelli, T.M. Tritt, Skutterudites: A phonon-glass-electron crystal approach to advanced thermoelectric energy conversion applications, Annual Review of Materials Science, 29 (1999) 89.

[5] J. Yang, H.M. Li, T. Wu, W.Q. Zhang, L.D. Chen, J.H. Yang, Evaluation of Half-Heusler Compounds as Thermoelectric Materials Based on the Calculated Electrical Transport Properties, Advanced Functional Materials, 18 (2008) 2880.

[6] J.P. Heremans, V. Jovovic, E.S. Toberer, A. Saramat, K. Kurosaki, A. Charoenphakdee, S. Yamanaka, G.J. Snyder, Enhancement of thermoelectric efficiency in PbTe by distortion of the electronic density of states, Science, 321 (2008) 554.

[7] P. Rauwel, O.M. Løvvik, E. Rauwel, E.S. Toberer, G.J. Snyder, J. Taftø, Nanostructuring in β-Zn_4Sb_3 with variable starting Zn compositions, physica status solidi (a), 208 (2011) 1652.

[8] L.D. Zhao, S.H. Lo, Y. Zhang, H. Sun, G. Tan, C. Uher, C. Wolverton, V.P. Dravid, M.G. Kanatzidis, Ultralow thermal conductivity and high thermoelectric figure of merit in SnSe crystals, Nature, 508 (2014) 373.

[9] Y.J. Fu, J.T. Xu, G.Q. Liu, J.K. Yang, X.J. Tan, Z. Liu, H.M. Qin, H.Z. Shao, H.C. Jiang, B. Liang, J. Jiang, Enhanced thermoelectric performance in p-type polycrystalline SnSe benefiting from texture modulation, J. Mater. Chem. C, 4 (2016) 1201.

[10] N.K. Singh, S. Bathula, B. Gahtori, K. Tyagi, D. Haranath, A.J.J.o.A. Dhar, Compounds, The effect of doping on thermoelectric performance of p-type SnSe: Promising thermoelectric material, 668 (2016) 152.

[11] H. Guo, H. Xin, X. Qin, J. Zhang, D. Li, Y. Li, C. Song, C. Li, Enhanced thermoelectric performance of highly oriented polycrystalline SnSe based composites incorporated with SnTe nanoinclusions, Journal of Alloys and Compounds, 689 (2016) 87.

[12] W.R. Shi, M.X. Gao, J.P. Wei, J.F. Gao, C.W. Fan, E. Ashalley, H.D. Li, Z.M. Wang, Tin Selenide (SnSe): Growth, Properties, and Applications, Advanced Science, 5 (2018).

[13] Y.K. Lee, Z. Luo, S.P. Cho, M.G. Kanatzidis, I. Chung, Surface oxide removal for polycrystalline SnSe reveals near-single-crystal thermoelectric performance, Joule, 3 (2019) 719.

[14] M. Tripathi, C. Bhandari, High-temperature thermoelectric performance of Si-Ge alloys, Journal of Physics: Condensed Matter, 15 (2003) 5359.

[15] V. Zaitsev, M. Fedorov, E. Gurieva, I. Eremin, P. Konstantinov, A.Y. Samunin, M. Vedernikov, Highly effective $Mg_2Si_{1-x}Sn_x$ hermoelectrics, Physical Review B, 74 (2006) 045207.

[16] Y. Pei, X. Shi, A. LaLonde, H. Wang, L. Chen, G.J. Snyder, Convergence of electronic bands for high performance bulk thermoelectrics, Nature, 473 (2011) 66.

[17] X. Yan, B. Poudel, Y. Ma, W. Liu, G. Joshi, H. Wang, Y. Lan, D. Wang, G. Chen, Z. Ren, Experimental studies on anisotropic thermoelectric properties and structures of n-type $Bi_2Te_{2.7}Se_{0.3}$, Nano letters, 10 (2010) 3373.

[18] H. Wang, A.D. LaLonde, Y. Pei, G.J. Snyder, The criteria for beneficial disorder in thermoelectric solid solutions, Advanced Functional Materials, 23 (2013) 1586.

[19] U. Mizutani, The Hume-Rothery rules for structurally complex alloy phases, Surface Properties And Engineering Of Complex Intermetallics, World Scientific2010, pp. 323.

[20] W. Liu, J. He, H. Huang, H. Wang, Z. Lu, C. Liu, Effects of Nb additions on the microstructure and mechanical property of CoCrFeNi high-entropy alloys, Intermetallics, 60 (2015) 1.

[21] Y.-M. Han, J. Zhao, M. Zhou, X.-X. Jiang, H.-Q. Leng, L.-F. Li, Thermoelectric performance of SnS and SnS-SnSe solid solution, Journal of Materials Chemistry A, 3 (2015) 4555.

[22] T.-R. Wei, C.-F. Wu, X. Zhang, Q. Tan, L. Sun, Y. Pan, J.-F. Li, Thermoelectric transport properties of pristine and Na-doped $SnSe_{1-x}Te_x$ polycrystals, Physical Chemistry Chemical Physics, 17 (2015) 30102.

[23] T.R. Wei, G.J. Tan, C.F. Wu, C. Chang, L.D. Zhao, J.F. Li, G.J. Snyder, M.G. Kanatzidis, Thermoelectric transport properties of polycrystalline SnSe alloyed with PbSe, Applied Physics Letters, 110 (2017).

[24] R. Saini, M. Singh, R. Kumar, G. Jain, Electrical properties of $SnTe_xSe_{1-x}$ sintered films, Optoelectronics and Advanced Materials-Rapid Communications, 3 (2009) 49.

[25] M. Hong, Z.-G. Chen, L. Yang, T.C. Chasapis, S.D. Kang, Y. Zou, G.J. Auchterlonie, M.G. Kanatzidis, G.J. Snyder, J. Zou, Enhancing the thermoelectric performance of $SnSe_{1-x}Te_x$ nanoplates through band engineering, Journal of Materials Chemistry A, 5 (2017) 10713.

[26] S. Chen, K. Cai, W. Zhao, The effect of Te doping on the electronic structure and thermoelectric properties of SnSe, Physica B: Condensed Matter, 407 (2012) 4154.

[27] W. Sheng, M. Myint, J.G. Chen, Y. Yan, Correlating the hydrogen

evolution reaction activity in alkaline electrolytes with the hydrogen binding energy on monometallic surfaces, Energy & Environmental Science, 6 (2013) 1509.

[28] J. He, J.T. Xu, X.J. Tan, G.Q. Liu, H.Z. Shao, Z. Liu, H.C. Jiang, J. Jiang, Synthesis of SnTe/$AgSbSe_2$ nanocomposite as a promising lead− free thermoelectric material, J. Materiomics, 2 (2016) 165.

[29] J.H. Kim, Y.J. Song, J.S. Rhyee, B.S. Kim, S.D. Park, H.J. Lee, J.W. Shin, Small−polaron transport and thermoelectric properties of the misfit−layer composite $(BiSe)_{(1.09)}TaSe_2/TaSe_2$, Physical Review B, 87 (2013) 6.

[30] L.−D. Zhao, C. Chang, G. Tan, M.G. Kanatzidis, SnSe: a remarkable new thermoelectric material, Energy & Environmental Science, 9 (2016) 3044−.

[31] M. Zhang, D. Wang, C. Chang, T. Lin, K. Wang, L.−D. Zhao, Oxygen adsorption and its influence on the thermoelectric performance of polycrystalline SnSe, J. Mater. Chem. C, 7 (2019) 10507.

[32] A. Volykhov, V. Shtanov, L. Yashina, Phase relations between germanium, tin, and lead chalcogenides in pseudobinary systems containing orthorhombic phases, Inorganic Materials, 44 (2008) 345.

[33] S. Sassi, C. Candolfi, J.−B. Vaney, V. Ohorodniichuk, P. Masschelein, A. Dauscher, B. Lenoir, Assessment of the

thermoelectric performance of polycrystalline p-type SnSe, Applied Physics Letters, 104 (2014) 212105.

[34] Q. Zhang, E.K. Chere, J. Sun, F. Cao, K. Dahal, S. Chen, G. Chen, Z. Ren, Studies on thermoelectric properties of n-type polycrystalline $SnSe_{1-x}S_x$ by iodine doping, Advanced Energy Materials, 5 (2015) 1500360.

[35] D. Feng, Z.-H. Ge, D. Wu, Y.-X. Chen, T. Wu, J. Li, J. He, Enhanced thermoelectric properties of SnSe polycrystals via texture control, Physical Chemistry Chemical Physics, 18 (2016) 31821.

[36] Y. Li, F. Li, J. Dong, Z. Ge, F. Kang, J. He, H. Du, B. Li, J.-F. Li, Enhanced mid-temperature thermoelectric performance of textured SnSe polycrystals made of solvothermally synthesized powders, J. Mater. Chem. C, 4 (2016) 2047.

[37] P. Maycock, Thermal conductivity of silicon, germanium, III-V compounds and III-V alloys, Solid-state electronics, 10 (1967) 161-.

[38] J. Jimenez, J.W. Tomm, Spectroscopic analysis of optoelectronic semiconductors, Springer2016.

[39] P.U. Bhaskar, G.S. Babu, Y.K. Kumar, V.S. Raja, Investigations on co-evaporated Cu_2SnSe_3 and Cu_2SnSe_3-ZnSe thin films, Applied Surface Science, 257 (2011) 8529.

[40] G. Shi, E. Kioupakis, Anisotropic spin transport and strong visible-light absorbance in few-layer SnSe and GeSe, Nano letters,

15 (2015) 6926.

[41] X. Su, P. Si, Q. Hou, X. Kong, W. Cheng, First-principles study on the bandgap modulation of Be and Mg co-doped ZnO systems, Physica B: Condensed Matter, 404 (2009) 1794.

[42] S.R. Popuri, M. Pollet, R. Decourt, F.D. Morrison, N.S. Bennett, J.W.G. Bos, Large thermoelectric power factors and impact of texturing on the thermal conductivity in polycrystalline SnSe, J. Mater. Chem. C, 4 (2016) 1685.

[43] A. Maznev, O.J.A.j.o.p. Wright, Demystifying umklapp vs normal scattering in lattice thermal conductivity, 82 (2014) 1062.

Notice; This chapter published in *Materials on Dec* 2019. The title is "Electrical Transport and Thermoelectric Properties of SnSe–SnTe Solid Solution" and the authors are Jun-Young Cho, Muhammad Siyar, Woo Chan Jin, Euyheon Hwang, Seung-Hwan Bae, Seong-Hyeon Hong, Miyoung Kim and Chan Park.

(Materials 2019, 12(23), 3854; https://doi.org/10.3390/ma12233854)

Chapter 7 Effect of CNT Addition on the Thermoelectric Properties of $SnSe_{0.7}Te_{0.3}Se$/CNT Composites.

7.1 Introduction

Thermoelectric (TE) devices which can convert temperature differences to electrical voltage and vice versa, have attracted a lot of attention for their application in many fields which include active cooling of electronic components and waste heat recovery. The cooling and the generation of electricity using TE materials have multiple significant advantages over the technology which they are expected to replace, such as the absence of moving parts, no emission of green house and hazardous gases, and low maintenance. [1−3] The performance of a TE material is represented by the figure of merit (ZT), $ZT = (S^2\sigma/k)T$, where S, σ, k, and T are Seebeck coefficient, electrical conductivity, thermal conductivity, and absolute temperature, respectively. [4]. SnSe compounds consisting of earth−abundant, less expensive and low−toxic elements are considered as one of the most promising thermoelectric materials in the medium temperature range because its single crystal possesses the highest ZT of 2.62 along the crystallographic b−axis at 923 K [5]. However,

the application of single crystal is limited due to the high production cost and poor mechanical properties. So, many studies have been conducted to obtain polycrystalline SnSe having a high ZT value. We already reported that when Te is doped into the SnSe, the electrical conductivity by was increased due to the increase of carrier concentration, while the lattice thermal conductivity was suppressed by the increased amount of phonon scattering, which result in a ZT of ~ 0.78 at 823K from $SnSe_{0.7}Te_{0.3}$, which is ~11% improvement compared to that of the SnSe. It, however, is still much lower than that of single crystal.

One possible way to improve the TE performance is to make polycrystalline SnSe-based nanocomposite. Various secondary phases such as SnTe [6] SnS [7] $MoSe_2$ [8] PbSe [9] Carbon nanotube [10] Carbon black (CB) [11] were used to enhance thermoelectric performance of polycrystalline SnSe. Recently, CNT has been considered as a better candidate because of its low dimensions and high electrical conductivity which may also enhance the mechanical strength of the TE material [12]. The improvement of TE property in TE material such as Bi_2Te_3 [13], oxide-based [14] and organic TE materials [15] by adding CNT as a secondary phase. Kim et al [13] and Ren et al. [12] showed reported CNT addition can lead to both reductions of electrical conductivity and thermal

conductivity of in the BiTe−based TE material. On the other hands, Dreßler et al. [16] and Khasimsaheb et al. [17] showed that dispersed CNT can lead the increase in electrical conductivity and decrease in thermal conductivity of Al−doped ZnO and PbTe, respectively. Chu et al. [10] and showed that the dispersion of CNTs reduces the thermal conductivity without significant deterioration on the electrical conductivity, and a ZT of 0.96 was obtained at 773 K along the direction perpendicular to the sintering pressing. Thus, the precise role of CNT addition on the TE properties is still not fully understood, and a detailed study of the TE transport properties of SnSe/CNT composite is needed. In this study, the effect of CNT addition on the TE property $SnSe_{0.7}Te_{0.3}$/CNT were investigated. Our expectation is that when CNTs are well dispersed at the grain boundaries between $SnSe_{0.7}Te_{0.3}$, the electrical conductivity can be enhanced by formation of the electrical network of CNTs while the thermal conductivity can be suppressed by enhanced phonon scattering at CNT/matrix interfaces.

7.2 Experimental Procedure

7.2.1 Fabrication of Bulk $SnSe_{0.7}Te_{0.3}$/CNT Composites

Figure 7-1 shows the experimental procedure. Sn (99.99%, Sigma Aldrich), Se (99.99%, Sigma Aldrich) and Te (99.99%, Kunjundo Chemicals) powders were used to synthesize the polycrystalline SnSe-SnTe solid solutions. High purity single elements of Sn, Se and Te were weighed according to the stoichiometry of $SnSe_{0.7}Te_{0.3}$, loaded into a steel crucible (100 mL) at a ratio of 5:1 with steel balls of different diameters (3mm and 1mm) in an Ar filled glove box and then subjected to mechanical alloying (MA). ~35% of the crucible was filled with the powder mixture and balls. The polycrystalline $SnSe_{0.7}Te_{0.3}$ powders were synthesized by MA at 250 rpm for 4 h, which was confirmed by XRD. 0, 0.3, 0.6 and 1 wt% of Multi-wall carbon nanotubes (MWCNTs, 95%, CNT Co., Ltd.) were mixed with $SnSe_{0.7}Te_{0.3}$ powders in ethanol. The solution was ultra-sonicated and stirred for 24h. The solution was dried in oven and then the powders were obtained. The dried powders were ground in an alumina mortar and sieved through a 140-mesh stainless steel mesh, loaded into a 12.5 mm-diameter graphite mold and was spark plasma sintered in vacuum (~ 2×10^{-3} Torr) at 850K for 10min under uni-axial pressure of 60 MPa.

7.2.2 Characterization

The qualitative phase analyses of the disk-shaped sintered samples were carried out using X-ray diffraction (XRD, D-8 Advanced, Bruker) with Cu K_α radiation. The microstructures of fracture surface of the sintered samples were observed using a field emission scanning electron microscope (FE-SEM, SU-70, JEOL), and the elemental distribution analyses were conducted on the polished surface of bulk samples using an energy-dispersive X-ray spectroscopy (EDS). Raman spectrum analyses of $SnSe_{0.7}Te_{0.3}$, CNT, $SnSe_{0.7}Te_{0.3}$/CNT composite samples were conducted in order to confirm whether CNTs are present without any other reactions. The dish-shaped sintered samples were cut into bars with dimensions of 1.5 x 1.5 x 7 mm^3. The bar-shaped samples were used for simultaneous measurement of Seebeck coefficient and electrical conductivity using a commercial measurement equipment (Seepel Corp) under an Ar atmosphere from room temperature to 850 K. Carrier concentrations of the SnSe samples were obtained using a Hall measurement system (HMS 3000, Ecopia) at room temperature. The total thermal conductivity (k_{tot}) can be expressed as the sum of electronic thermal conductivity (k_e) and lattice thermal conductivity

(k_{latt}). The k_{tot} was calculated by multiplying the specific heat (C_p), thermal diffusivity (D) and density (ρ). The C_p, D and ρ values were measured using the differential scanning calorimetry (DSC, Netzsch), the laser flash method (LFA457, Netzsch), and the Archimedes method, respectively. The k_e was obtained using the Wiedemann–Franz law, $k_e = L \sigma T$, where L, σ and T are Lorenz number, electrical conductivity and absolute temperature, respectively. The Lorenz number L which was obtained from fitting the Seebeck coefficient to the reduced chemical potential was used to obtain k_e [18]. The k_{latt} was obtained by subtracting the k_e from the k_{tot}. The TE properties of all samples were measured perpendicular to the direction of the pressure applied during the SPS.

Figure 7-1. An experimental procedure.

7.3 Results and Discussion

7.3.1 Phase Analysis of Bulk $SnSe_{0.7}Te_{0.3}$/CNT Composites

Figure 7-2 shows the XRD patterns of the sintered $SnSe_{0.7}Te_{0.3}$/CNT composites (0, 0.3, 0.6 and 1 wt % CNT) prepared using MA and spark plasma sintering. The XRD pattern shows that all the peaks shifted towards low 2θ values based on the XRD pattern position of orthorhombic SnSe orthorhombic SnSe (PDF #00-048-1224), which indicates that the incorporation of Te induces lattice expansion due the fact that Te has a larger atomic radius (0.21 nm) than Se (0.19 nm), which is consistent with the results in Chapter 6. However, presence of CNT-related peaks peaks intensity associated with CNTs were not observed in all samples. It is because that the small amount of CNT below the detection limit of XRD can lead to the absence of corresponding peak(s) in the XRD patterns.

Figure 7-3 shows the Raman spectrum of $SnSe_{0.7}Te_{0.3}$, CNT and of $SnSe_{0.7}Te_{0.3}$ with 1 wt % CNT. The Raman spectrum of $SnSe_{0.7}Te_{0.3}$ were recorded in the range of 50~150 cm^{-1} and that of pure CNTs shows a typical disorder-induced D-band at 1343 cm^{-1}, and a G-band at 1576 cm_{-1} indicating the presence of multi-walled CNTs.

When 1 wt % CNT is added to $SnSe_{0.7}Te_{0.3}$, the Raman shift related to CNT were not changed which means that CNTs are present without any other reaction.

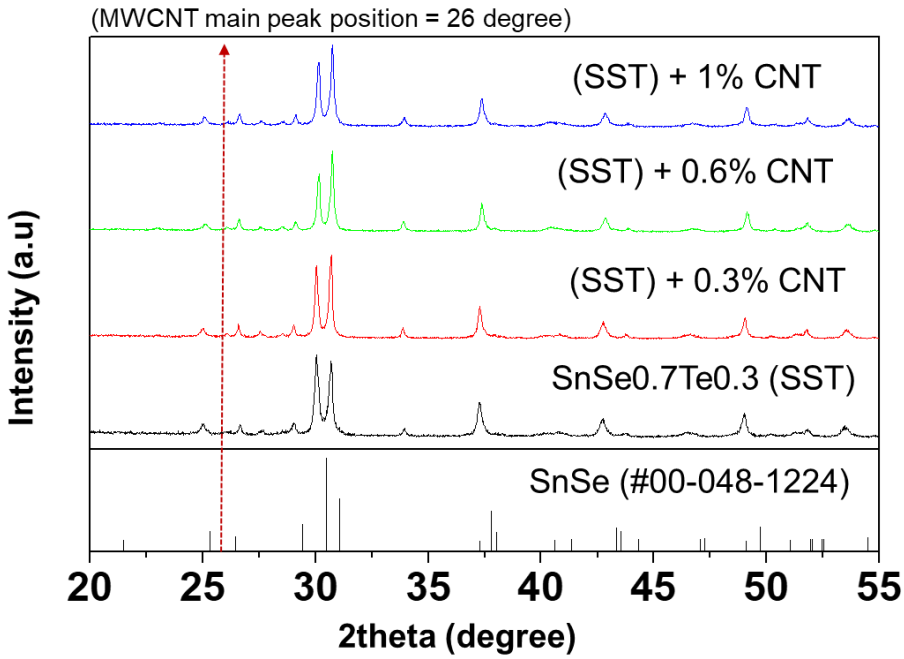

Figure 7-2. Theta-2theta XRD patterns of the polycrystalline $SnSe_{0.7}Te_{0.3}$/CNT (0, 0.3, 0.6 and 1 wt % CNT).

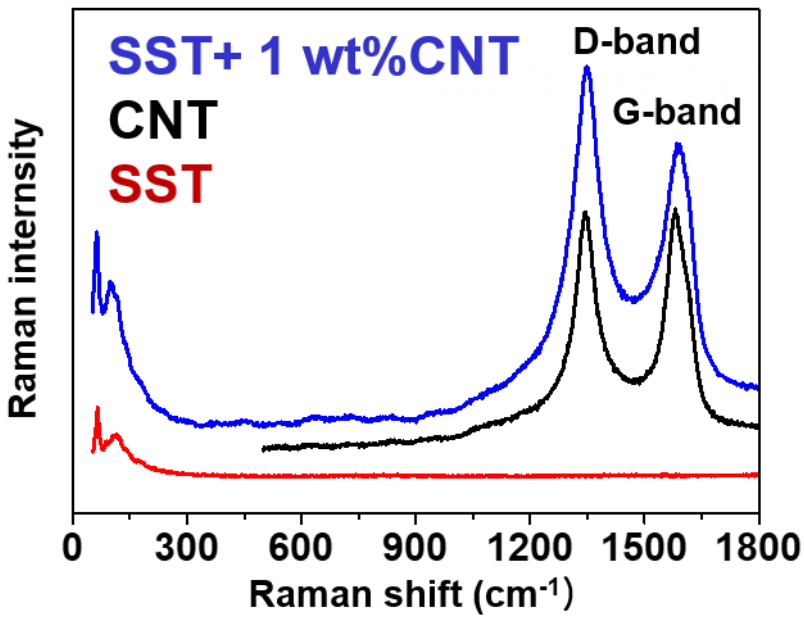

Figure 7-3. Raman spectrums of $SnSe_{0.7}Te_{0.3}$, CNT and $SnSe_{0.7}Te_{0.3}$/CNT (1 wt % CNT).

.

7.3.2 Microstructure of $SnSe_{0.7}Te_{0.3}$/CNT Composites

Figure 7-4 (a) show the schematic of microstructure and (b), (c) and (d) show FE-SEM micrographs taken from the fracture surface of polycrystalline $SnSe_{0.7}Te_{0.3}$/CNT composites (0.3, 0.6 and 1 wt % CNT). samples, respectively.

It was observed that the CNTs were well dispersed in all samples, and most of the samples added with 0.3 wt % CNT were present at the $SnSe_{0.7}Te_{0.3}$ interface. It was confirmed that the most CNTs were homogeneously distributed along the grain boundaries of $SnSe_{0.7}$Te0.3. When more than 0.6 wt% CNT was added, the CNTs were connected to each other to form a network, resulting in the creation of a number of new interfaces, which is consistent with the results of previous reports [10, 12, 13, 19]. The CNTs present in the $SnSe_{0.7}Te_{0.3}$ interface were identified by EDS mapping, and the results are shown in Figure 7-5.

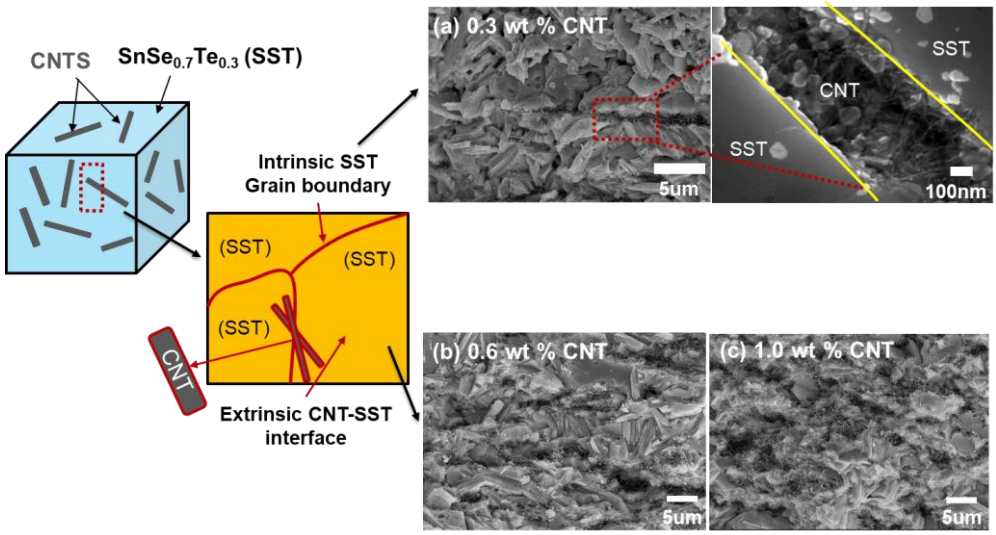

Figure 7-4. FE-SEM micrographs taken from the fracture surface of the polycrystalline $SnSe_{0.7}Te_{0.3}$ with addition of (a) 0.3 wt %, (b) 0.6 wt % and (c) 1.0 wt % CNTs.

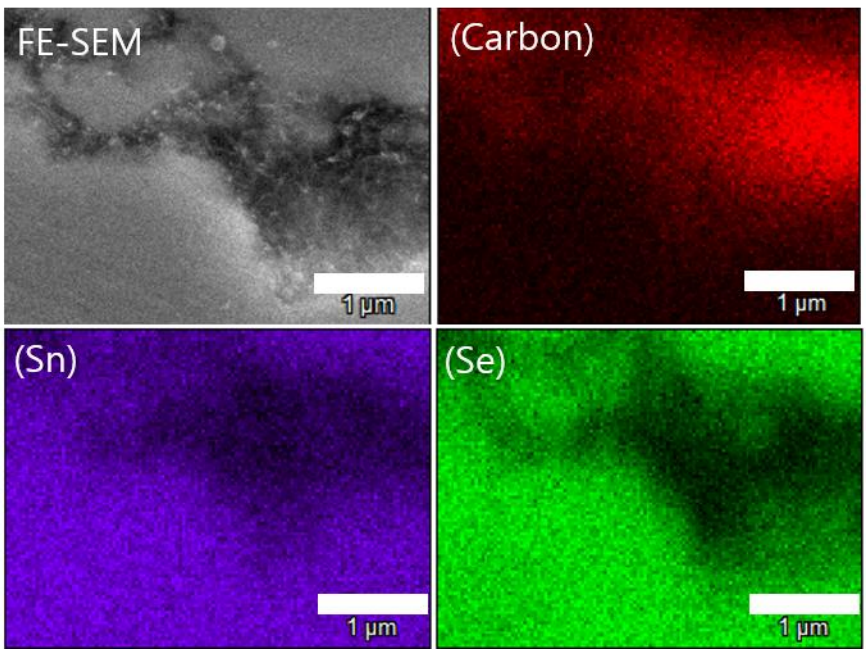

Figure 7-5. EDS mapping was performed on the polished surface of the polycrystalline $SnSe_{0.7}Te_{0.3}$/CNT composites (1wt % CNT).

7.3.3 Electrical Conductivity and Seebeck Coefficient of

$SnSe_{0.7}Te_{0.3}$/CNT Composites

As shown in figure 7-4 and 7-5, Presences of CNTs dispersed along the interface of the matrix and Interfaces created by the connection of CNTs, and it can affect the TE properties. To understand the variations in charge transport properties with increasing CNT contents, the carrier concentration (n) and carrier mobility (μ) of all samples were measured at room temperature, and the results are shown in figure 7-6. The n values of all the samples are positive, which indicates that hole is the major carrier and all sample are the p-type semiconductor. As the CNT contents are increased, n is increased from 1.2 x 10^{18} to 6.5 x 10^{19}, while μ is decreased from 5.6 to 2.4 $cm^{-2}\ V^{-1}\ s^{-1}$.

Figure 7-7 (a) shows the temperature-dependency of electrical conductivity (σ) of the polycrystalline $SnSe_{0.7}Te_{0.3}$/CNT composites (0, 0.3, 0.6 and 1 wt % CNT). With increasing CNT contents, the electrical conductivity was increased, which can be explained with the microstructure and change of carrier concentration (n) and mobility (μ). The movement of hole carriers is disturbed at newly generated grain boundaries, which result in the reduction of μ. The increase in n can be explained by the difference between the intrinsic hole concentration of CNT and $SnSe_{0.7}Te_{0.3}$. The carrier

concentration of $SnSe_{0.7}Te_{0.3}$ and CNT are ~10^{-20} cm^{-3} and ~$10^{17\sim18}cm^{-3}$, respectively. Therefore, high carrier concentration of CNT may the increase in the electrical conductivity with addition of CNT can be caused by high carrier concentration of CNT.

Figure 7-7 (b) shows the temperature-dependency of Seebeck coefficient (S) of the polycrystalline $SnSe_{0.7}Te_{0.3}$/CNT composites (0, 0.3, 0.6 and 1 wt % CNT). Unlike the electrical conductivity, the S values of the samples are decreased with the increase of amount of CNT. Generally, S values are determined by Pisarenko relationship [37], which indicates that S value is inversely proportional to the carrier concentration. As shown in Figure 7-3, the carrier concentration was increased with the increase of CNT content, which can lead to the decrease of Seebeck coefficient. Therefore, the change in the electrical conductivity and the Seebeck coefficient can be influenced by the increase in carrier concentration

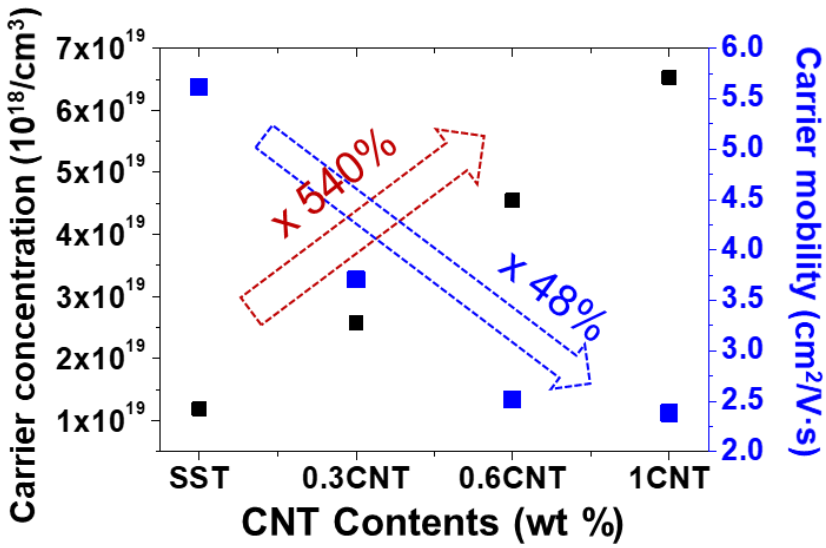

Figure 7-6. Charge transport properties of polycrystalline $SnSe_{0.7}Te_{0.3}$/CNT (0, 0.3, 0.6 and 1 wt % CNT). The carrier concentration (n), carrier mobility (u) were measured at room temperature.

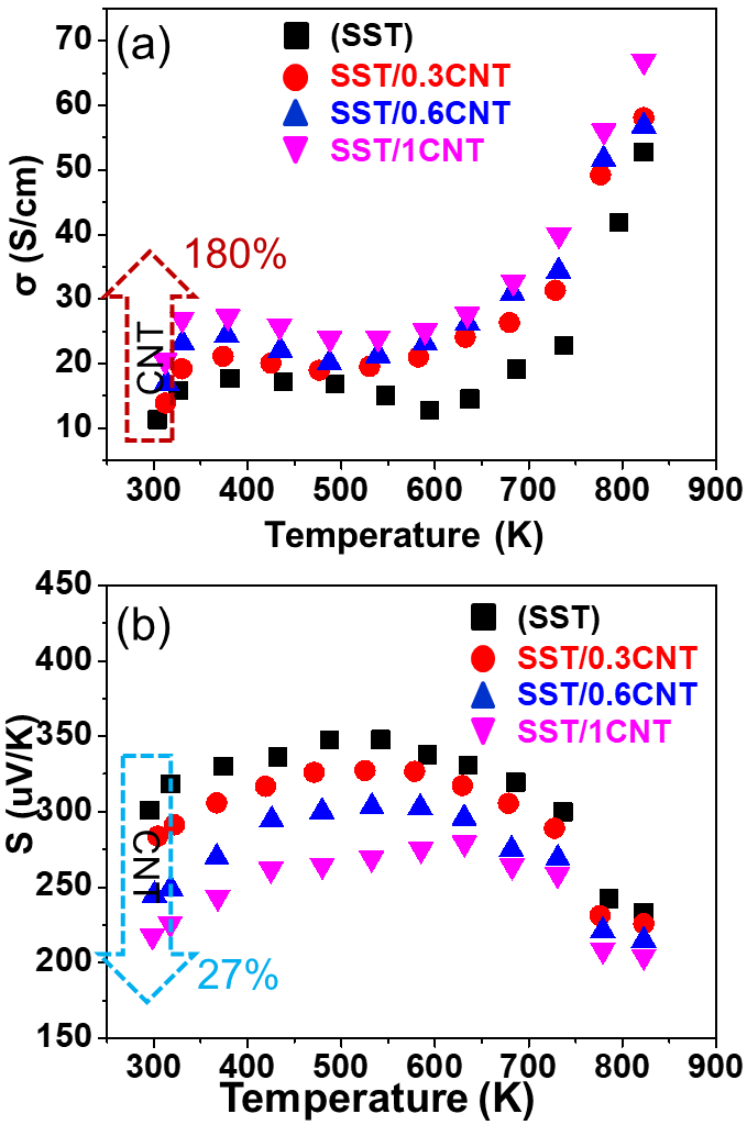

Figure 7-7. The temperature-dependency of (a) electrical conductivity (σ) and (b) Seebeck coefficient (S) of the polycrystalline $SnSe_{0.7}Te_{0.3}$/CNT (0, 0.3, 0.6 and 1 wt % CNT).

7.3.4 Thermal Conductivity and ZT of $SnSe_{0.7}Te_{0.3}$/CNT Composites

Figure 7-8 (a) shows the temperature-dependency of total thermal conductivities (k_{tot}) and of the polycrystalline $SnSe_{0.7}Te_{0.3}$/CNT composites and figure 7-8 (b) total conductivity at room temperature of polycrystalline $SnSe_{0.7}Te_{0.3}$/CNT composites. As the amount of CNT added increases, the change in the k_{tot} is as follows; k_{tot} decreased up to 0.3 wt %, and then increased again. k_{tot} is expressed as the sum of electronic thermal conductivity (k_e) and lattice thermal conductivity (k_{latt}). In order to better understand the change of k_{tot} with CNT addition, the k_{tot} of all samples were separated into k_e and k_{latt}, and the results are shown in figure 7-9 (a) and (b). It was observed that the k_{tot} comes mainly from the k_{latt}. The k_e of the samples were increased with the increase of CNT content, which is attributed to the increase in electrical conductivity. With increasing CNT contents, the k_{latt} is initially decreased and then increased. The decrease in k_{latt} with the increase of Te content can come from the increased amount of phonon scattering. When 0.3 wt % CNT was added, the k_{latt} was decreased by phonon scattering at interface, which results in the decrease of k_{tot}. which is consistent with the results reported by Kim et al. [13] and Ren et al [12]. The increase

in k_{latt} with when 0.6 and 1 wt % CNT was added may be due to the high k_{latt} of the CNT. Heng et al. [20] and Zhang et al. [21] reported the k_{latt} of SnSe and MWCNT at room temperature, which were ~0.63W/m·K and ~3000 W/m·K, respectively. Therefore, as the amount of CNT increases, the TE property of $SnSe_{0.7}Te_{0.3}$/CNT composites will depend on the those of CNT.

Figure 7-10 shows the figure of merits (ZT) of the polycrystalline the polycrystalline $SnSe_{0.7}Te_{0.3}$/CNT composites, which were obtained from the electrical conductivity, Seebeck coefficient and thermal conductivity measured at different temperatures. The ZT value of $SnSe_{0.7}Te_{0.3}$ with 0.3 wt % CNT is higher than that of $SnSe_{0.7}Te_{0.3}$ and other $SnSe_{0.7}Te_{0.3}$/CNT composites at all measurement temperatures. The highest ZT obtained in this study was ~0.89 at 823K of $SnSe_{0.7}Te_{0.3}$ with 0.3 wt % CNT, which can be attributed to the improvement of electrical conductivity and the reduction of lattice thermal conductivity.

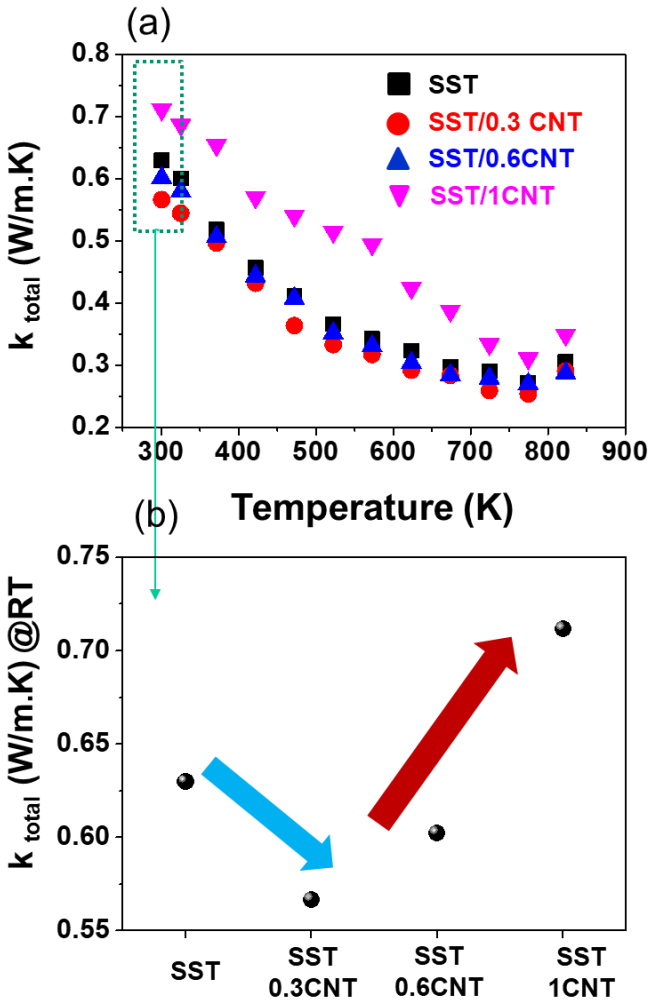

Figure 7-8. (a) The temperature-dependency of (a) total conductivity (k_{tot}) of polycrystalline $SnSe_{0.7}Te_{0.3}$/CNT composites (0, 0.3, 0.6 and 1 wt % CNT). (b) total conductivity at room temperature of polycrystalline $SnSe_{0.7}Te_{0.3}$/CNT composites.

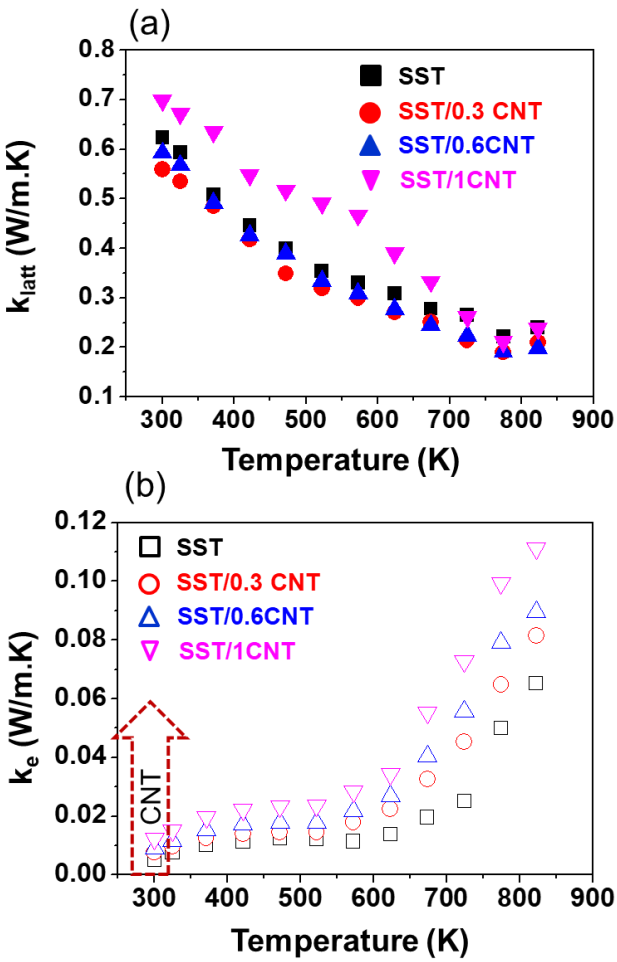

Figure 7-9. The temperature-dependency of (a) lattice conductivity (k_{latt}) and (b) electronic thermal conductivity of polycrystalline $SnSe_{0.7}Te_{0.3}$/CNT composites (0, 0.3, 0.6 and 1 wt % CNT).

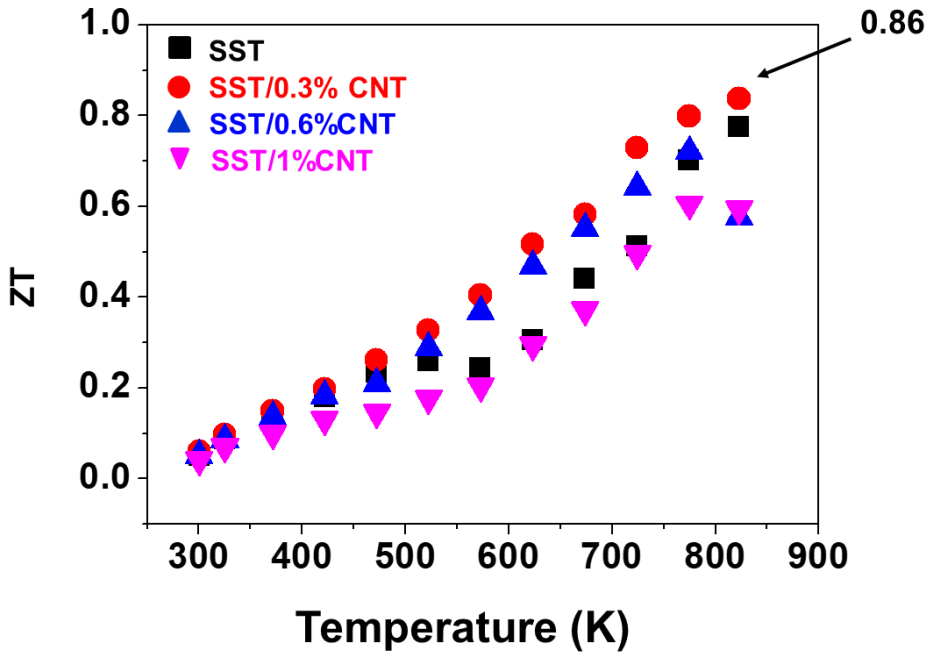

Figure 7-10. The figure of merits (ZT) of the polycrystalline $SnSe_{0.7}Te_{0.3}$/CNT composites (0, 0.3, 0.6 and 1 wt % CNT) measured at different temperatures.

7.4 Summary

In order to improve electrical conductivity and decrease the thermal conductivity of polycrystalline SnSe, the thermoelectric (TE) properties of $SnSe_{0.7}Te_{0.3}$/CNT composites (0, 0.3, 0.6 and 1 wt % CNT) were investigated. Our expectation is that when CNTs are well dispersed at the grain boundaries between $SnSe_{0.7}Te_{0.3}$, the electrical conductivity can be enhanced by formation of the electrical network of CNTs while the thermal conductivity can be suppressed by enhanced phonon scattering at $SnSe_{0.7}Te_{0.3}$/CNT interfaces. Most CNTs are dispersed along the grain boundaries of $SnSe_{0.7}Te_{0.3}$ and are connected to each other when the amount of CNT reaches 0.6 wt %, thereby forming new interfaces, which can result in the decrease in hole carrier mobility. In spite of the reduced mobility, the electrical conductivity was increased due to the high intrinsic hole concentration of CNT. When 0.3 wt% CNT was added, the decrease in lattice thermal conductivity due to phonon scattering at the interface was observed, and when more CNT were added, the total thermal conductivity was improved due to the high thermal conductivity of CNT. A ZT of ~ 0.86 at 823K was obtained from $SnSe_{0.7}Te_{0.3}$ with 0.3 wt % CNT, which is the highest ZT value obtained in this study.

7.5 References

[1] D.M. Rowe, Modules, systems, and applications in thermoelectrics, CRC press (2012).

[2] D.M. Rowe, Thermoelectrics handbook: macro to nano, CRC press (2018).

[3] G.J. Snyder, E.S. Toberer, Complex thermoelectric materials, materials for sustainable energy: a collection of peer-reviewed research and review articles from Nature Publishing Group, World Scientific (2011) 101.

[4] F.J. DiSalvo, Thermoelectric cooling and power generation, Science, 285 (1999) 703.

[5] L.-D. Zhao, S.-H. Lo, Y. Zhang, H. Sun, G. Tan, C. Uher, C. Wolverton, V.P. Dravid, M.G. Kanatzidis, Ultralow thermal conductivity and high thermoelectric figure of merit in SnSe crystals, Nature, 508 (2014) 373.

[6] H. Guo, H. Xin, X. Qin, J. Zhang, D. Li, Y. Li, C. Song, C. Li, Enhanced thermoelectric performance of highly oriented polycrystalline SnSe based composites incorporated with SnTe nanoinclusions, Journal of Alloys and Compounds, 689 (2016) 87.

[7] Y.-M. Han, J. Zhao, M. Zhou, X.-X. Jiang, H.-Q. Leng, L.-F. Li, Thermoelectric performance of SnS and SnS-SnSe solid solution, Journal of Materials Chemistry A, 3 (2015) 4555-4559.

[8] X.-Q. Huang, Y.-X. Chen, M. Yin, D. Feng, J. He, Origin of the enhancement in transport properties on polycrystalline SnSe with compositing two-dimensional material $MoSe_2$, Nanotechnology, 28 (2017) 105708.

[9] G. Tang, W. Wei, J. Zhang, Y. Li, X. Wang, G. Xu, C. Chang, Z. Wang, Y. Du, L.-D. Zhao, Realizing High Figure of Merit in Phase-Separated Polycrystalline $Sn_{1-x}Pb_xSe$, Journal of the American Chemical Society, 138 (2016) 13647.

[10] F. Chu, Q. Zhang, Z. Zhou, D. Hou, L. Wang, W. Jiang, Enhanced thermoelectric and mechanical properties of Na-doped polycrystalline SnSe thermoelectric materials via CNTs dispersion, Journal of Alloys and Compounds, 741 (2018) 756.

[11] J. Li, D. Li, W. Xu, X. Qin, Y. Li, J. Zhang, Enhanced thermoelectric performance of SnSe based composites with carbon black nanoinclusions, Applied Physics Letters, 109 (2016) 173902.

[12] F. Ren, H. Wang, P.A. Menchhofer, J.O. Kiggans, Thermoelectric and mechanical properties of multi-walled carbon nanotube doped $Bi_{0.4}Sb_{1.6}Te_3$ thermoelectric material, Applied Physics Letters, 103 (2013) 221907.

[13] K.T. Kim, S.Y. Choi, E.H. Shin, K.S. Moon, H.Y. Koo, G.-G. Lee, G.H. Ha, The influence of CNTs on the thermoelectric properties of a CNT/Bi_2Te_3 composite, Carbon, 52 (2013) 541.

[14] G. Tang, W. Yang, J. Wen, Z. Wu, C. Fan, Z. Wang, Ultralow thermal conductivity and thermoelectric properties of carbon nanotubes doped $Ca_3Co_4O_{9+\delta}$, Ceramics International, 41 (2015) 961.
[15] Q. Zhang, W. Wang, J. Li, J. Zhu, L. Wang, M. Zhu, W. Jiang, Preparation and thermoelectric properties of multi-walled carbon nanotube/polyaniline hybrid nanocomposites, Journal of Materials Chemistry A, 1 (2013) 12109.
[16] C. Dreßler, R. Löhnert, J. Gonzalez-Julian, O. Guillon, J. Töpfer, S. Teichert, Effect of Carbon Nanotubes on Thermoelectric Properties in $Zn_{0.98}Al_{0.02}O$, Journal of electronic materials, 45 (2016) 1459.
[17] B. Khasimsaheb, N.K. Singh, S. Bathula, B. Gahtori, D. Haranath, S. Neeleshwar, The effect of carbon nanotubes (CNT) on thermoelectric properties of lead telluride (PbTe) nanocubes, Current Applied Physics, 17 (2017) 306.
[18] J. He, J. Xu, X. Tan, G.-Q. Liu, H. Shao, Z. Liu, H. Jiang, J. Jiang, Synthesis of SnTe/$AgSbSe_2$ nanocomposite as a promising lead-free thermoelectric material, J. Materiomics, 2 (2016) 165.
[19] H. Bark, J.-S. Kim, H. Kim, J.-H. Yim, H. Lee, Effect of multiwalled carbon nanotubes on the thermoelectric properties of a bismuth telluride matrix, Current Applied Physics, 13 (2013) S111.
[20] K.L. Heng, S.J. Chua, P. Wu, Prediction of semiconductor

material properties by the properties of their constituent chemical elements, Chemistry of materials, 12 (2000) 1648.
[21] Q. Zhang, G. Chen, S. Yoon, J. Ahn, S. Wang, Q. Zhou, Q. Wang, J. Li, Thermal conductivity of multiwalled carbon nanotubes, Physical Review B, 66 (2002) 165440.

Chapter 8 Summary and Suggestions for Future work

SnSe-based thermoelectric (TE) materials have captured much attention since single-crystal SnSe exhibited record high ZT. Despite the excellent TE properties, SnSe single crystal has problems of poor mechanical properties and costly/not-simple fabrication process. And so, many studies have been conducted to obtain polycrystalline SnSe having TE performance as high as that of a single crystal. The ZT values of polycrystalline SnSe, however, are still lower than that of single crystal SnSe mainly due to their relatively low electrical conductivity (σ) and high thermal conductivity (k).

In this dissertation, the effect of microstructure and electronic structure on the thermoelectric properties of polycrystalline SnSe were investigated to obtain the high TE performances of polycrystalline SnSe. A summary of each main research topic and its results is as follow;

1. The effects of sintering pressure on the electrical transport and thermoelectric properties of the polycrystalline SnSe.

- Degree of texture was enhanced with increasing sintering pressure.
- Electrical conductivity was enhanced with increasing sintering pressure

– Thermal conductivity were significantly increased with a pressure of 60MPa

– A ZT of ~0.7 was obtained at 823K from the polycrystalline SnSe, which was sintered with a pressure of 60MPa, which can be attributed to large increase in electrical conductivity with very small increase of the thermal conductivity.

2. Electrical Transport and Thermoelectric Properties of SnSe–SnTe Solid Solution.

– The solubility limit of Te in $SnSe_{1-x}Te_x$ is somewhere between x = 0.3 and 0.5.

– Band gap is decreased with increasing Te contents, which reasults in the increase of hole carrier concentartion

– Electrical conductivity were increased and Seebeck coefficient were decreased due to the increase of carrier concentration.

– Presence of Te at Se site can act as an effective point defect, which can increase phonon scattering and reduce lattice thermal conductivity.

– A ZT of ~0.78 was obtained at 823K from the $SnSe_{0.7}Te_{0.3}$, which was ~11% higher than that of SnSe.

3. Effect of CNT addition on the thermoelectric properties of $SnSe_{0.7}Te_{0.3}$Se/CNT composites.

– Most CNTs are dispersed along the grain boundaries of

$SnSe_{0.7}Te_{0.3}$ and are connected to each other when the amount of CNT reaches 0.6 wt %, thereby forming new interfaces.

– With increasing CNT contents, the electrical/thermal conductivities were increased, which can be attributed to the higher intrinsic hole concentration of CNTs compared to $SnSe_{0.7}Te_{0.3}$.

– When 0.3 wt % CNT was added, the lattice thermal conductivity was decreased by phonon scattering at interface, which results in the decrease of total thermal conductivity.

– A ZT of ~ 0.86 at 823K was obtained from $SnSe_{0.7}Te_{0.3}$ with 0.3 wt % CNT, which is the highest ZT value obtained in this study.

The results of ZT obtained in this study are compared with t hose reported in the literature those, and the result are shown in figure 8-1. The TE performance efficiency of polycrystalline SnSe compounds remains still low for TE applications; therefore, the enhancement in the thermoelectric performance is still challenging.

From the literature review and the study presented here, some suggestions for the further study are as follows:

1. Using both effects simultaneously to improve TE performance

– Doping with texturing

– Oriented nano-sized grains

– Defect-induced Crystals

2. Oxide Removal Process and Its effect on TE Properties on

Polycrystalline SnSe

– SnO and SnO_2 on the surface of SnSe particle

– K_{tot} of SnO ~ 2 W $m^{-1} K^{-1}$ at RT, K_{tot} of SnO_2 ~ 98 W and ~55 $m^{-1} K^{-1}$ at along the c– and a–axes at RT

– The presence of thin oxides is detrimental to electrical and thermal transport properties of intrinsic p–type SnSe

– Removing SnO and SnO_2 oxides on the surface of SnSe will effectively improve the TE properties of polycrystalline SnSe.

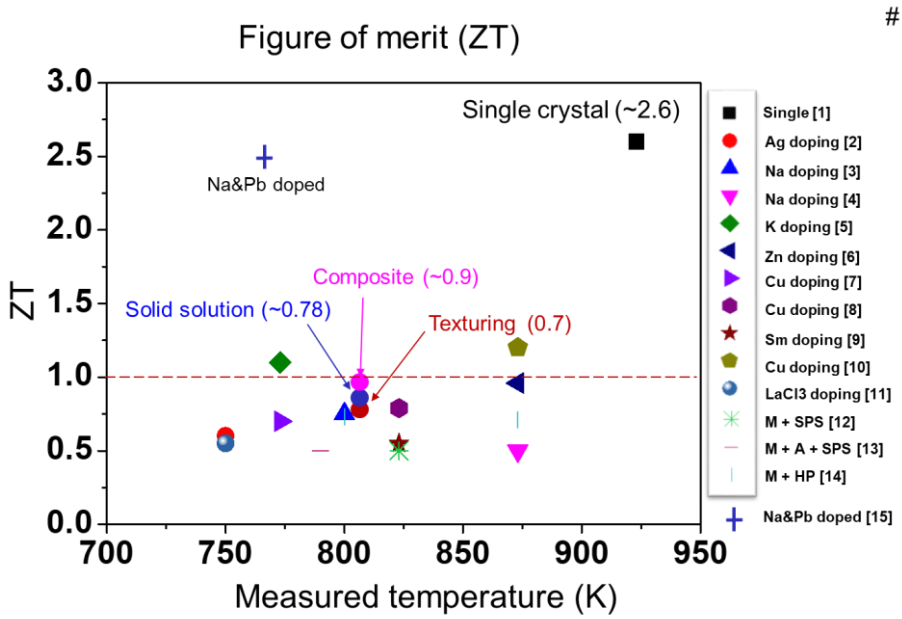

Figure 8-1. Comparison of the ZT values [1-15]

8.1 References

[1] L.-D. Zhao, S.-H. Lo, Y. Zhang, H. Sun, G. Tan, C. Uher, C. Wolverton, V.P. Dravid, M.G. Kanatzidis, Ultralow thermal conductivity and high thermoelectric figure of merit in SnSe crystals, Nature, 508 (2014) 373.

[2] C.-L. Chen, H. Wang, Y.-Y. Chen, T. Day, G.J. Snyder, Thermoelectric properties of p-type polycrystalline SnSe doped with Ag, Journal of Materials Chemistry A, 2 (2014) 11171.

[3] Y.X. Chen, Z.H. Ge, M. Yin, D. Feng, X.Q. Huang, W. Zhao, J. He, Understanding of the extremely low thermal conductivity in high-performance polycrystalline SnSe through potassium doping, Advanced Functional Materials, 26 (2016) 6836.

[4] J. Gao, G. Xu, Thermoelectric performance of polycrystalline $Sn_{1-x}Cu_xSe$ (x= 0-0.03) prepared by high pressure method, Intermetallics, 89 (2017) 40.

[5] J. Gao, H. Zhu, T. Mao, L. Zhang, J. Di, G. Xu, The effect of Sm doping on the transport and thermoelectric properties of SnSe, Materials Research Bulletin, 93 (2017) 366.

[6] Y. Gong, C. Chang, W. Wei, J. Liu, W. Xiong, S. Chai, D. Li, J. Zhang, G. Tang, Extremely low thermal conductivity and enhanced thermoelectric performance of polycrystalline SnSe by Cu doping, Scripta Materialia, 147 (2018) 74/

[7] H.-Q. Leng, M. Zhou, J. Zhao, Y.-M. Han, L.-F. Li, The thermoelectric performance of anisotropic SnSe doped with Na, Rsc Advances, 6 (2016) 9112.

[8] F. Li, W. Wang, Z.-H. Ge, Z. Zheng, J. Luo, P. Fan, B. Li, Enhanced thermoelectric properties of polycrystalline SnSe via LaCl3 doping, Materials, 11 (2018) 203.

[9] J. Li, D. Li, X. Qin, J. Zhang, Enhanced thermoelectric performance of p-type SnSe doped with Zn, Scripta Materialia, 126 (2017) 6.

[10] N.K. Singh, S. Bathula, B. Gahtori, K. Tyagi, D. Haranath, A. Dhar, The effect of doping on thermoelectric performance of p-type SnSe: Promising thermoelectric material, Journal of Alloys and Compounds, 668 (2016) 152.

[11] T.-R. Wei, G. Tan, X. Zhang, C.-F. Wu, J.-F. Li, V.P. Dravid, G.J. Snyder, M.G. Kanatzidis, Distinct impact of alkali-ion doping on electrical transport properties of thermoelectric p-type polycrystalline SnSe, Journal of the American Chemical Society, 138 (2016) 8875.

[12] W. Shi, M. Gao, J. Wei, J. Gao, C. Fan, E. Ashalley, H. Li, Z. Wang, Tin Selenide (SnSe): Growth, Properties, and Applications, Adv Sci (Weinh), 5 (2018) 1700602.

[13] Y. Li, X. Shi, D. Ren, J. Chen, L. Chen, Investigation of the

anisotropic thermoelectric properties of oriented polycrystalline SnSe, Energies, 8 (2015) 6275.

[14] D. Li, J. Li, X. Qin, J. Zhang, C. Song, L. Wang, H. Xin, Thermoelectric performance for SnSe hot-pressed at different temperature, Journal of Electronic Materials, 46 (2017) 79.

[15] Y.K. Lee, Z. Luo, S.P. Cho, M.G. Kanatzidis, I. Chung, Surface oxide removal for polycrystalline SnSe reveals near-single-crystal thermoelectric performance, Joule, 3 (2019) 719.

Publications [1st; 8 Co; 8]

[1] Jun-Young Cho, Muhammad Siyar, Woo Chan Jin, Euyheon Hwang, Seung-Hwan Bae, Seong-Hyeon Hong, Miyoung Kim, and Chan Park, "Electrical transport and thermoelectric properties of SnSe-SnTe solid solution, Materials 12, 3854 (2019)

[2] Jun-Young Cho, Muhammad Siyar, Sung-Hwan Bae, Junsik Mun, Miyoung Kim and Chan Park, "Effect of sintering pressure on electrical transport and thermoelectric properties of polycrystalline SnSe," Bulletin of Materials Science (2019). (accepted)

[3] Muhammad Siyar, Jun-Young Cho, Woo-Chan Jin, Euy Heon Hwang, Miyoung Kim and Chan Park, Thermoelectric Properties of Cu2SnSe3-SnS Composite, Materials 12, 13, (2019)

[4] Muhammad Siyar, Jun-Young Cho, Woo-Chan Jin, Jamil-Ur-Rehman and Chan Park, The Effect of Substrate Temperature on the Microstructure and Thermoelectric Properties of Pulsed Laser Deposited Cu_2SnSe_3 Thin Film," Journal of Nanoelectronics and Optoelectronics, 14 1 (2019).

[5] Jun-Young Cho, Woo-Chan Jin, Seung-Hwan Bae and Chan Park, "Evaluation of microstructure, phases, and mechanical properties of aged porcelain insulator," Korean Journal of Materials Research 29,

137 (2019)

[6] Jun-Young Cho, Tae-Ho An, Soo Young Shin, Hwang Sun Kim, Young Seok Kim, Hyunick Shin, Sung-Hwan Bae, Miyoung Kim, Seong-Hyeon Hong and Chan Park, "The effects of sintering conditions on the microstructure and mechanical properties of SiC prepared using powders recovered from kerf loss sludge," Bulletin of Materials Science, 41, 157 (2018)

[7] Muhammad Siyar, Jun-Young Cho, Yong Youn, Seungwu Han, Miyoung Kim, Sung-Hwan Bae and Chan Park, "Effect of annealing temperature on the phase transition, band gap and thermoelectric properties of Cu_2SnSe_3," Journal of Materials Chemistry C, 6, 1780 (2018)

[8] Jun-Young Cho, Tae-ho An, Sang-gu Ji, Youngseok Kim, Hyunick Shin, Sarah Wonjung Kim, Sung-Hwan Bae, Miyoung Kim and ChanPark, "The effects of B_4C addition on the microstructure and mechanical properties of SiC prepared using powders recovered from kerf loss sludge," Ceramics International, 43, 15332 (2017)

[9] Jun-Young Cho, Woo-Seok Kim, Ho-Sung An, Hee-Sung An, Tae-wan Kim, Yun-Seog Lim, Sung-Hwan Bae and Chan Park, "Effect of Porcelain/Polymer Interface on the Microstructure, Insulation Characteristics and Electrical Field Distribution of Hybrid

Insulators," Journal of the Korean Institute of Electrical and Electronic Material Engineers, 30, 558 (2017)

[10] Yong-Kwon Chung, Jae-Hong Koo, Shin-A Kim, Eun-Ok Chi, Jun-Young Cho, Woon-Bae Sohn, Mi-Young Kim and Chan Park, "Growth mechanism of Si_3N_4 nanowires from amorphous Si_3N_4 powders synthesized by low-temperature vapor-phase reaction, CrysEngComm, 18, 3247 (2016)

[11] Tae-Ho An, Young Soo Lim, Mi Jin Park, Jang-Yeul Tak, Soonil Lee, Hyung Koun Cho, Jun-Young Cho, Chan Park and Won-Seon Seo, "Composition-dependent charge transport and temperature-dependent density of state effective mass interpreted by temperature-normalized Pisarenko plot in $Bi_{2-x}Sb_xTe_3$ compounds, APL Materials 4, 104812 (2016)

[12] Jun-Young Cho, Seunghyun Ahn, Sung-Hwan Bae, Gwi-Rang Kim, Jae-Hun Han, Deuk-Hee Lee, Jin-Sang Kim, Kyu Jeong Song and Chan Park, "The Effect of Bi/Sn Ratio of Bi-Sn-Ag Solder on the Mechanical and Electrical Properties of Interfaces Between Solder/Thermoelectric Material and Solder/Electrode," Journal of Nanoelectronics and Optoelectronics, 10, 504 (2015)

[13] Jun-Young Cho, O-Jong Kwon, Yong Kwon Chung, Jin-Sang Kim, Woo-Seok Kim, Kyu Jeong Song and Chan Park, "Effect of

Trivalent Bi Doping on the Seebeck Coefficient and Electrical Resistivity of $Ca_3Co_4O_9$," Journal of Electronic Materials, 44, 3621 (2015)

[14] Girish S. Gund, Deepak P. Dubal, Nilesh R. Chodankar, Jun-Young Cho, Pedro Gomez-Romero, Chan Park and Chandrakant D. Lokhande, "Low-cost flexible supercapacitors with high-energy density based on nanostructured MnO_2 and Fe_2O_3 thin films directly fabricated onto stainless steel" Scientific Reports 5, 12454, (2015)

[15] Sejin Yoon, Jun-Young Cho, Hyun Koo, Sung-Hwan Bae, Seunghyun Ahn, Gwi Rang Kim, Jin-Sang Kim and Chan Park, " Thermoelectric Properties of n-Type Bi_2Te_3/$PbSe_{0.5}Te_{0.5}$ Segmented Thermoelectric Material, " Journal of Electronic Materials, 43, 414 (2014)

[16] Sejin Yoon, O-Jong Kwon, Seunghyun Ahn, Jae-Yeol Kim, Hyun Koo, Sung-Hwan Bae, Jun-Young Cho and Chan Park, "The Effect of Grain Size and Density on the Thermoelectric Properties of Bi_2Te_3-PbTe Compounds", Journal of Electronic Materials, 45, 3390-3396 (2013)

Patents [6]

[1] Jun-Young Cho, Chan Park, Mi-Young Kim, Sang-Gu Ji, Young-Seok Kim and Hyun-Ick Shin, "Recycling method of silicon carbide using Kerf loss sludge", KR1020190034074 (2019)

[2] Jun-Young Cho, Chan Park, Mi-Young Kim, Sung-Hwan Bae, Sang-Gu Ji and Jong-Hun Ryu, "Seebeck coefficient and electrical conductivity measurement device made of quartz tube and method", KR1020246790000 (2019)

[3] Chan Park, SeungHyun Ahn, Young-Sung Yoo, Sunghwan Bae, Jun-Young Cho and Miyoung Kim, "Methods of fabricating mesoporous composite powder and solid oxide fuel cell using the same", KR1020254400000 (2019)

[4] Jong-Hun Ryu, Chan Park, Miyoung Kim, Heung Nam Han, Jun-Young Cho, Woo Chan Jin, "Sintering apparatus for selectively applying electric", KR10180167288 (2018)

[5] Jong-Hun Ryu, Jun-Young Cho, Chan Park, Mi-Young Kim and Sang-Gu Ji, "Activated sintering apparatus having pressure control part" KR1020170127297 (2017)

[6] Chan Park, Sejin Yoon, Seunghyun Ahn, Sung-Hwan Bae, Hyun Koo, Jangwon Han, Jun-Young Cho, Kyeong-dal Choi and O-Jong Kwon, "Segmented thermoelectric material including diffusion barrier and fabrication method", KR1014703930000 (2014)

국문초록

미세구조 및 전자구조가 다결정 SnSe 열전 특성에 미치는 영향

조준영

공과대학 재료공학부

서울대학교

화석 연료 및 기존 에너지 자원들의 소비가 증가함에 따라 에너지 자원의 고갈 및 환경 오염이 전 세계적인 문제로 대두되고 있으며, 이를 해결하기 위해 새롭고, 친환경적이면서 재생 가능한 에너지 자원에 대한 수요가 높아지고 있다. 열에너지를 전기에너지로 상호 변환할 수 있는 열전 기술은 에너지 위기와 환경 문제를 해결 할 수 있는 대안 중 하나로 주목받고 있다. 열전재료의 효율은 $ZT = S^2\sigma T/k$로 나타내어지며 제백 계수 (S), 전기전도도 (σ), 열전도도 (k), 절대온도 (T), 로 구성된다. 높은 열전변환효율을 얻기 위해서, 열전재료는 높은 전기전도도와 제벡 계수, 그리고 낮은 열전도도를

동시에 가져야 한다. 하지만, 변수들의 복잡한 상호관계로 인하여 ZT 값을 최적화하는데 어려움이 있다. 예를 들어 캐리어 농도가 높을수록 전기전도도 (σ)는 증가하는 반면, 제벡 계수 (S)는 감소한다. 또한, 전기전도도의 저하 없이 열전도도만을 억제하는 것은 어렵다. 따라서 높은 열전효율을 갖기 위해서는 전하 농도의 최적화가 필요하며, 일반적으로 10^{19}~10^{20} cm^{-3} 의 캐리어 농도를 가질 때 열전 특성이 우수하다고 알려져 있다.

최근 독성이 없고 지구상에 풍부한 원소를 포함하는 SnSe는 2014년에 단결정의 b 축 방향으로 ~ 2.6 (923K)의 높은 ZT값이 보고되면서 실용화 가능성이 큰 열전재료로 주목을 받고 있다. 그러나, 기계적 특성이 열악하고 생산 비용이 많이 들기 때문에 단결정 SnSe를 소자에 사용하는 것은 어렵다. 이러한 이유로 SnSe에 대한 연구는 고효율의 다결정 SnSe를 개발하는 데 집중하고 있다. 하지만, 다결정 SnSe는 단결정 SnSe에 비해 상대적으로 낮은 전기전도도와 높은 열전도도 때문에 ZT 값이 낮다. 따라서, 높은 열전 효율을 가지는 다결정 SnSe를 얻기 위해서는 전기전도도를 증가시키고, 열전도도를 감소시켜야 한다.

본 연구에서는 미세구조 및 전자구조가 다결정 SnSe의 열전 특성에 미치는 영향을 조사하였으며, 미세구조, 밴드구조, 계면구조를 제어하여 다결정 SnSe의 전기전도도와 열전도도를 동시에 제어하여 열전 효율을 향상시켰다.

먼저 다결정 SnSe의 전기전도도를 향상시키기 위해, 소결 압력이 다결정 SnSe의 미세구조와 열전 특성에 미치는 영향에 관해 연구를 진행하였다. 기계적 합금화 공정으로 다결정 SnSe 분말을 합성한 후, 다양한 압력 조건 (30, 60, 90, 120MPa)에서 통전 활성 소결 (spark plasma sintering, SPS)하여 텍스처링 정도가 다양한 다결정 SnSe 소결체를 제조하였다. 소결 압력이 30에서 120MPa로 증가함에 따라 텍스쳐링 향상에 의해 홀 농도가 증가하였으며, 이로 인해 전기전도도가 향상하는 거동을 보였다. 반면, 소결 압력이 증가함에 따라 격자 열전도도의 증가로 인해 열전도도가 크게 증가하였으며, 이는 입계에서의 포논 산란의 감소에 따른 영향으로 해석하였다. 60 MPa의 압력으로 소결한 다결정 SnSe의 823K에서 ZT ~ 0.7 값을 얻었으며, 이는 전기전도도의 큰 증가와 매우 적은 열전도도의 증가에 따른 결과이다. 이 연구를 통해 SPS 동안 가해진 압력 조건을 변화시켜 텍스처의 정도를 제어함으로써 다결정 SnSe의 열전 특성이 향상될 수 있음을 보여주었다.

다음으로 SnSe-SnTe 고용체의 전하 수송과 열전 특성 관련 연구를 진행하였다. 기계적 합금화와 통전 활성 소결을 이용하여 $SnSe_{1-x}Te_x$ (x=0, 0.1, 0.3, 0.5, 0.8, 1) 소결체를 제조하였다. XRD 및 EPMA 분석을 통해 $SnSe_{1-x}Te_x$에서 Te의 고용 한도가 약 0.3~0.5 임을 확인하였다. Te 함량이 증가함에 따라, 홀 농도 증가로 인해 전기전도도가 향상되는 경향을 보였다. UV-VIS-NIR을 이용한 밴드갭 에너지 측정 및 DFT 밴드 구조 계산 결과를 통해 밴드갭 감소

때문에 홀 농도가 증가할 수 있음을 확인하였다. 전체 열전도도는 Te 함량이 증가함에 따라 감소하였고, 이는 격자 열전도도 감소에 따른 것이다. Te은 Se보다 원자 질량 및 크기가 더 크고, Se site에서 Te의 존재는 효과적인 점 결함으로 작용하여 포논 산란을 증가시켜 격자 열전도도를 감소시킬 수 있다. $SnSe_{0.7}Te_{0.3}$으로부터 823K에서 ~ 0.78의 ZT 값이 얻어졌으며, 이는 다결정 SnSe에 비해 ~ 11% 증가한 결과이다.

마지막으로, $SnSe_{0.7}Te_{0.3}$/CNT 복합체의 전하 전송과 열전 특성에 미치는 영향에 대한 연구를 진행하였다. $SnSe_{0.7}Te_{0.3}$에 다양한 함량의 CNT (0, 0.3, 0.6, 1 wt %)를 첨가하여 혼합한 후, 통전 활성 소결을 이용하여 $SnSe_{0.7}Te_{0.3}$/CNT 복합체를 제조하였다. CNT는 대부분 $SnSe_{0.7}Te_{0.3}$ 입계를 따라 분산되어 있으며, CNT 함량이 증가함에 따라 서로 연결되어 새로운 계면을 형성하며 홀 이동도가 감소하는 것을 확인하였다. 전기전도도는 CNT 함량이 증가함에 따라 증가하는 경향을 보였는데, 이는 $SnSe_{0.7}Te_{0.3}$에 비해 높은 CNT의 홀 농 때문에 전기전도도가 증가한 것으로 해석하였다. 0.3 wt % CNT가 첨가된 경우 계면에서의 포논 산란으로 격자 열전도도가 감소하며, 이는 전체 열전도도를 감소시켰다. 하지만 0.6 및 1wt %의 CNT가 첨가된 경우 CNT 고유의 높은 격자 열전도도로 인하여 전체 열전도도가 증가하는 경향을 보였다. 따라서 0.3 wt % CNT가 첨가된 $SnSe_{0.7}Te_{0.3}$ 로부터 823K에서 ~ 0.86의 ZT 값이 얻어졌으며, 이는 본 연구에서 얻을 수 있었던 가장 높은 ZT 값이다.

이러한 연구 결과를 통해 미세구조와 전자구조가 다결정 SnSe의 열전 특성에 미치는 영향에 대해서 좀 더 깊은 이해를 할 수 있었으며, 이 연구 결과는 앞으로 다결정 SnSe의 열전 특성을 향상시키고 특성을 이해하는 데 크게 활용될 것으로 기대한다.

핵심어: SnSe, 통전 활성 소결, 열전 특성, 미세 구조, 밴드 구조, 텍스처링, 고용체, 복합체